

Weak-lensing magnification as a probe for the dark Universe

Manuel García Fernández



GOBIERNO
DE ESPAÑA

MINISTERIO
DE ECONOMÍA, INDUSTRIA
Y COMPETITIVIDAD

Ciemat

Centro de Investigaciones
Energéticas, Medioambientales
y Tecnológicas



EXCELENCIA
MARÍA
DE MAEZTU

cfp
CIEMAT
física de partículas



Departamento de Investigación Básica – División de Astrofísica de Partículas
Centro de Investigaciones Energéticas Medioambientales y Tecnológicas

y

Departamento de Física Teórica – Facultad de Ciencias
Universidad Autónoma de Madrid

Weak-lensing magnification as a probe for the dark Universe

Presentado por:
Manuel García Fernández
Para la obtención del grado de Doctor en Física Teórica.

Dirigido por:
Dr. Eusebio Sánchez Álvaro
y
Dr. Ignacio Sevilla Noarbe

Madrid, Marzo-XXX del 2017

According to RD-99/2011, in partial fulfillment to obtain the ‘Mención Internacional’ qualification, this Thesis is written in English.

According to UAM’s Normative (12/15/2011), Summary and Conclusions are also written in Spanish and included before the core of the Thesis, right after the table of contents.

Conforme al RD-99/2011, en requerimiento parcial para la obtención de la calificación de ‘Mención Internacional’, esta Tesis está redactada en Inglés.

Conforme al acuerdo del Consejo de Gobierno de la UAM (15/12/2011), el Resumen y las Conclusiones también se encuentran redactadas en Castellano y se incluyen antes del cuerpo de la Tesis justo después del índice.

This Thesis is part of the following publication archives:

The DES Collaboration archive:

Fermilab preprint/thesis server:

Part of the results obtained during the development of this Thesis has been published under peer-review journals and proceedings. Their references are listed below.

Parte de los resultados obtenidos durante el desarrollo de esta Tesis han sido publicados en revistas y conferencias con un proceso de revisión por pares. Sus referencias bibliográficas se encuentran abajo.

M. Garcia-Fernandez, E. Sanchez and N. Sevilla-Noarbe. *Magnification with wide-field photometric surveys*. Highlights on Spanish Astrophysics XII. March 2017.

M. Garcia-Fernandez et al. *Weak lensing magnification in the Dark Energy Survey Science Verification data*, arXiv:1611.10326. November 2016.

Cover image credit: M. Garcia-Fernandez & The DES Collaboration

Chapter header credit: NASA

Yesterday's sensation is today's calibration.
RICHARD FEYNMAN

And tomorrow's background!
VALENTINE TELEGDI



Contents

Resumen y Conclusiones	ix
Resumen	ix
Conclusiones	ix
Summary	xi
1 Introduction	1
1.1 The expanding Universe	3
1.2 Dark Energy Models	4
1.2.1 The Cosmological Constant	4
1.2.2 Exotic matter fields	7
1.2.3 Modified Gravity	9
1.3 Current status of Dark Energy constrains	12
1.4 Alternative probes for Dark Energy: Voids & Troughs	15
2 Gravitational Lensing Theory	17
2.1 Lens Equation on Gravitational Fields	17
2.2 Weak Gravitational Lensing	19
2.2.1 Magnification	21
2.2.2 Shear	25
2.3 The Kaiser-Squires inversion.	27

3	The Dark Energy Survey	29
3.1	The DECam	30
3.2	Survey strategy	30
3.2.1	The transient survey	32
3.2.2	The wide-field survey	32
3.2.3	The night operations at CTIO	32
3.3	The data reduction pipeline	33
4	Magnification in DES	35
4.1	Magnification in the MICE-GC simulation	35
4.2	Magnification in DES Science Verification data	35
4.2.1	Data sample	36
4.2.2	Detection of the weak-lensing magnification signal	39
4.2.3	Systematic error analysis	48
4.3	Magnification in DES Year 1 data	61
4.3.1	Data sample	61
4.3.2	Determination of matter profile: voids & troughs	61
5	Conclusions	63
A	Appendix My test appendix	65
	References	67



Resumen y Conclusiones

Resumen

Conclusiones



Summary



1. Introduction

Nature's change and evolution is produced by the dynamics of the bodies and systems contained within the Universe. All the interactions of Universe can be described in terms of the four Fundamental Forces: gravitation, weak, electromagnetic and strong in ascending order of relative strength. High Energy Physics was able to unify the weak, electromagnetic and strong forces in terms of a $SU(3) \times SU(2) \times U(1)$ symmetry group in what is known as the *Standard Model* [1–5]. Nevertheless, attempts to unify Gravitation with the other forces has still not provided satisfactory results.

The current consensus theory of gravitation is Einstein's General Relativity, that describes gravity as a universal deformation ($h_{\mu\nu}$) of the Minkowski metric tensor ($\eta_{\mu\nu}$)

$$g_{\mu\nu}(x^\lambda) = \eta_{\mu\nu} + h_{\mu\nu}(x^\lambda), \quad (1.1)$$

where $g_{\mu\nu}$ is the metric tensor of the Universe. Gravity is postulated as a massless spin-two field with self-interaction Lagrangian

$$\mathcal{L}[g_{\mu\nu}] = \frac{c^4}{16\pi G_N} \sqrt{-g} g^{\mu\nu} R_{\mu\nu}(g), \quad (1.2)$$

that couples minimally and universally to all the fields of the Standard Model; where $R_{\mu\nu}$ is the Ricci tensor, c the speed of light and G_N Newton's constant [6–12].

From the total action, Einstein's equation of the gravitational field can be obtained [13, 14]:

$$R_{\mu\nu} - \frac{1}{2} R g_{\mu\nu} = \frac{8\pi G_N}{c^4} T_{\mu\nu}, \quad (1.3)$$

where $T_{\mu\nu}$ is total energy-momentum tensor, that is the source of gravity.

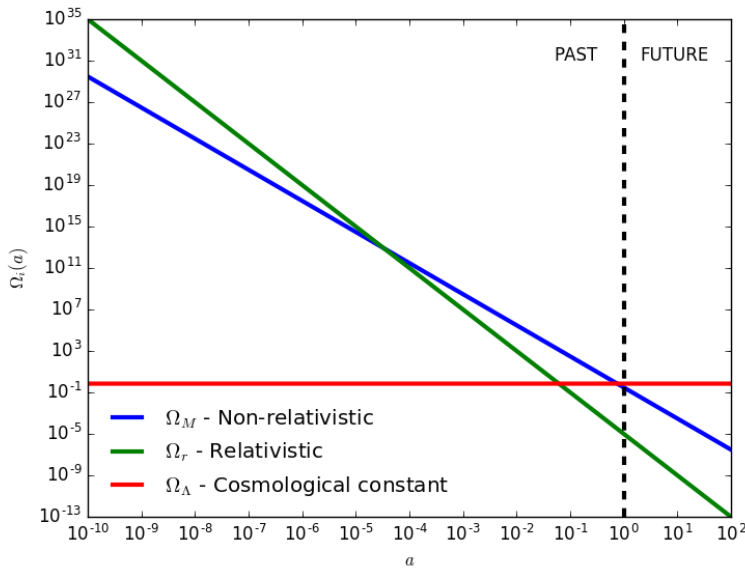


Figure 1.1: Critical energy density for different types of matter species as function of the scale parameter of the Universe: relativistic (cold matter), non-relativistic (radiation), and cosmological constant. It can be seen that at present (black-dashed line), cosmological constant has just started to be dominant over the other species, starting the accelerated expansion era.

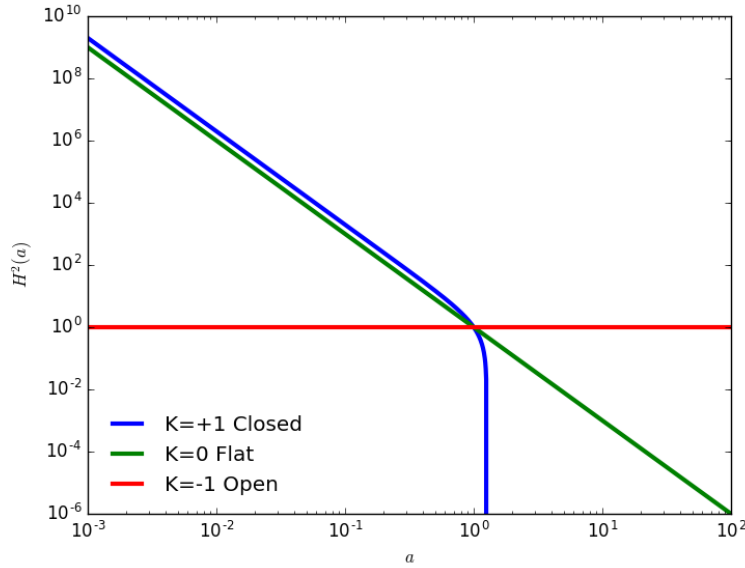


Figure 1.2: Expansion rate as function of the scale parameter of the Universe for different geometries (assume $\Omega_M = 1$). The flat geometry expansion rate decreases until at infinity reaches zero. Open geometries show a constant expansion rate leading to an exponential growth of the scale factor. Closed geometries drops to zero very fast and eventually becomes negative leading to a re-collapse of the Universe.

1.1 The expanding Universe

One of the consequences of Einstein's equation is that the metric tensor is not static, implying that the geometry of the Universe changes. Thus, the Universe is a dynamical entity itself and its past and future evolution can be computed within the framework of General Relativity.

Assuming that the Universe is homogeneous and isotropic [15, 16], the only possible metric tensor is the Friedman-Lemaître-Robertson-Walker metric (FLRW) given by the line element [17]

$$ds^2 = -dt^2 + a^2(t) \left[\frac{dr^2}{1 - Kr^2} + r^2(d\theta^2 + \sin^2 \theta d\phi^2) \right], \quad (1.4)$$

where $a(t)$ is a function of time known as scale factor, $K = -1, 0, 1$ is the curvature of the universe and r, θ, ϕ are spatial 3D spherical coordinates.

Solving Einstein's equation for this metric, an expression for the evolution of the scale factor with time can be obtained

$$H^2(t) \equiv \left[\frac{\dot{a}(t)}{a(t)} \right]^2 = \frac{8\pi G_N}{3c^4} \rho(t) - \frac{K}{a^2(t)}, \quad (1.5)$$

where the dot denotes time derivatives, and ρ is the total density of energy. The parameter H has been defined as the expansion rate and its value at present H_0 is known as Hubble's constant.

Expansion rate can be expressed in terms of the critical energy density

$$H^2(t) = H_0^2 \left[\sum_i \Omega_i(t) - \Omega_K \right] \quad (1.6)$$

with

$$\Omega_K \equiv \frac{K}{[a(t)H_0]^2} \quad \text{and} \quad \Omega_i(t) \equiv \frac{8\pi\rho_i(t)}{3H_0^2}. \quad (1.7)$$

The parameter Ω_i is the critical density of the i -th matter/energy species whose evolution with time can be computed using Thermodynamics. For non-relativistic matter –that is, matter with velocity $v \ll c$,

$$\Omega_M(t) = \Omega_M^0 a^{-3}(t), \quad (1.8)$$

whereas for relativistic matter species –that is, $v \sim c$ – also known as radiation,

$$\Omega_r(t) = \Omega_r^0 a^{-4}(t). \quad (1.9)$$

Here Ω_i^0 denotes the value on the present day of the i -th matter species and by construction

$$\sum_i \Omega_i^0 = 1 + \Omega_K \quad (1.10)$$

Taking into account that the matter species and the curvature evolve on a different manner with time (Figure 1.1), its relative abundance at present fixes the expansion rate for the whole history of the Universe from birth to death. Discarding the hypothesis of empty Universe¹ and taking into account that for $a \rightarrow \infty$ all the matter species are diluted, three scenarios of expansion history can be considered depending on the curvature density of the Universe (Figure 1.2):

- **Big Crunch:** Universe closed, with positive curvature ($K = 1$). The attractive gravitational self-interaction of the Universe causes the gravitational collapse of the whole Universe into a single point.
- **Big Rip:** The Universe has negative curvature ($K = -1$), the gravitational repulsive self-interaction of the Universe causes a perpetual accelerated expansion.
- **Big Freeze:** The Universe is flat ($K = 0$) and expands forever at a decelerated rate until it stops at $a \rightarrow \infty$.

Thus, the curvature of the Universe is the critical parameter to determine its thermal history. The latest combination of different cosmological probes determine it to be $\Omega_K = -0.0001^{+0.0054}_{-0.0052}$ [18], quantity close to the floor of experimental accuracy [19], allowing to assume safely that the Universe is flat. Thus, the Universe is expected to be expanding at a decelerated rate. Although, the expansion of the Universe has been known for a century since Hubble's measurement of the recession velocity of galaxies [20], measurements of type-Ia supernovae (SNIa) two decades ago and confirmed since then by several probes [21] show that the expansion of the Universe is accelerating (Figure 1.3 and Figure 1.4).

1.2 Dark Energy Models

Two independent experiments of different properties of the Universe show contradictory measurements: the Universe is flat and its expansion is accelerated. This implies two things, either Equation 1.3 is wrong or the Universe is filled with new matter specie, that does not dilute with cosmic expansion and has negative pressure. Whatever drives this accelerated expansion is known as Dark Energy. Dark Energy models can be divided in three categories: the cosmological constant, exotic matter fields and modified gravity.

Among all the possible explanations, the cosmological constant is considered the fiducial explanation for dark energy.

1.2.1 The Cosmological Constant

The Cosmological Constant was initially proposed by Einstein himself [24] to avoid the solutions of the General Relativity where the Universe was not static and later discarded, when the expansion of the Universe was discovered by Hubble. Nevertheless, on the light of the recent events of accelerated expansion, the Cosmological Constant was soon recovered. The approach followed by this model

¹At least, this Thesis is present at the Universe, therefore it is not empty.

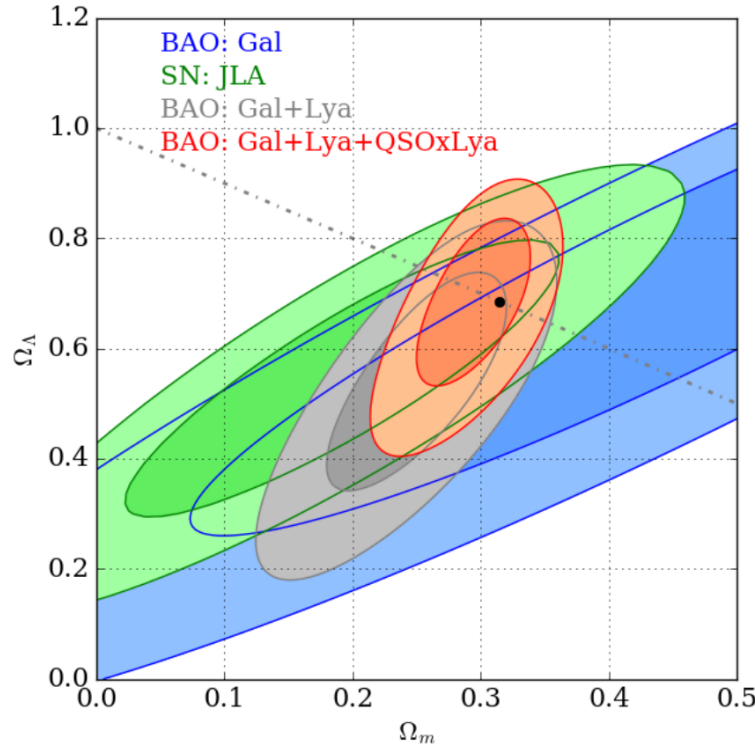


Figure 1.3: Latest constrains on the curvature of the Universe measured by the combination of barion acoustic oscillation (BAO) and supernovas (SN) [22]. Curvature can be obtained with Equation 1.10 assuming that the matter species are only dark energy and non-relativistic matter, Ω_Λ, Ω_M respectively. Black-solid dot is Planck 2015 best-fit result [18]. Flat Universe is the dash-dotted line.

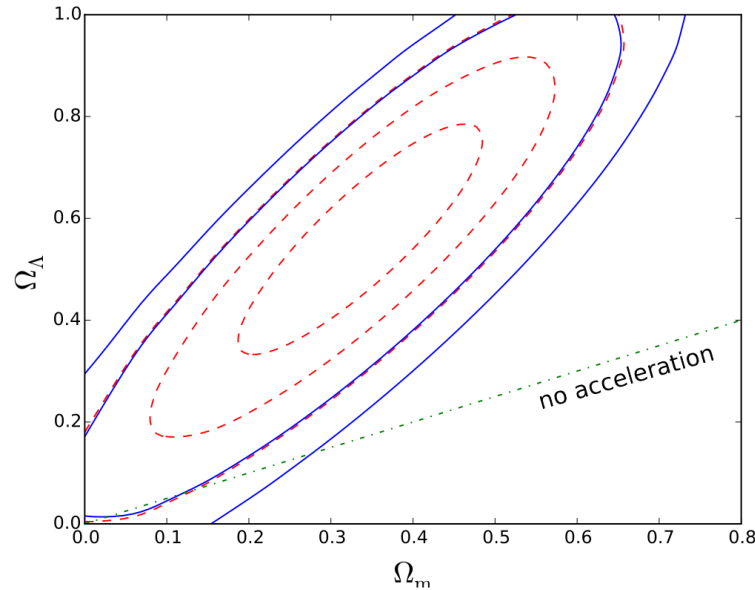


Figure 1.4: Reanalysis by J. T. Nielsen et al. of the Nobel Laureate SNIa data, demonstrating that accelerated expansion is solid [23].

consist on the addition of an additional covariant term to the Einstein field equations, a term proportional to the metric tensor ($\Lambda g_{\mu\nu}$), resulting [25]:

$$R_{\mu\nu} - \frac{1}{2}Rg_{\mu\nu} + \Lambda g_{\mu\nu} = \frac{8\pi G_N}{c^4}T_{\mu\nu}. \quad (1.11)$$

With this new term and assuming $\Omega_K = 0$ Equation 1.6 transforms into

$$H^2(t) = H_0^2 \left[\sum_i \Omega_i(t) + \Omega_\Lambda \right], \quad (1.12)$$

where Ω_Λ is the dark energy critical density. This new term is a time-independent constant that has the same value on every location of the Universe. Thus, as the other matter species has a critical density that decreases with time, the dark energy critical density has only impact at late cosmic times.

This new term may be regarded as a new matter specie such that

$$\rho_\Lambda = \frac{3H_0^2}{8\pi G_N} \Omega_\Lambda. \quad (1.13)$$

Taking into account Equation 1.10, an upper bound on the dark energy density can be established

$$\rho_v \leq \frac{3H_0^2}{8\pi G_N} \sim 10^{-47} \text{ GeV}^4. \quad (1.14)$$

Since this energy density is fills the whole Universe and is an inherent property of the geometry of the Universe and hence of the Universe itself, from a physical point of view it can be identified as the energy of the vacuum [26, 27]. Quantum Field Theory (QFT) states that the quantum vacuum is not empty and static but it actually is a dynamical entity where particle and antiparticles are constantly produced and annihilated as it has been demonstrated by the Casimir effect. Energy density of the vacuum can be estimated

$$\rho_{QFT} = \int_0^{1/L_P} dk \sqrt{k^2 + m^2} \frac{4\pi k^2}{(2\pi)^4} \sim 10^{71} \text{ GeV}^4, \quad (1.15)$$

where L_P is Planck's length. Thus, there's a miss-match between the amount of dark energy measured and that predicted by QFT of several orders of magnitude. It can be argued that although it is known that Planck's energy scale is the upper range of validity of Standard Model physics, nothing prevents that it starts to fail at lower scales. A lower bound on this point can be established as the Quantum Chromodynamics (QCD) cutoff scale (~ 200 MeV), leading to a vacuum energy density of

$$\rho_{QCD} = \int_0^{1/L_{QCD}} dk \sqrt{k^2 + m^2} \frac{4\pi k^2}{(2\pi)^4} \sim 10^{-3} \text{ GeV}^4, \quad (1.16)$$

reducing the tension between theory and experiment, but still being catastrophic. Some theories claim that a cancellation of modes may arise at super-symmetry models. Nevertheless, latest LHC results excluded most of the phase-space of supersymmetric models [28].

Several discrepancies indicate that either something is missing on the High Energy Physics side or on the Cosmology side. Nevertheless, it can be argued that no connection between the cosmological constant and quantum theory exists and define the cosmological constant as a free parameter of the theory. Despite this, a fine tune problem arises: the coincidence problem. As it has been observed by many experiments, the present day dark energy and matter density are very close, allowing the formation of structure. The redshift at which matter and dark energy densities are equal is given by

$$z_{eq} = \sqrt[3]{\frac{\Omega_\Lambda^0}{1 - \Omega_\Lambda^0}} - 1 \quad (1.17)$$

with $\Omega_\Lambda^0 \in (0, 1)$. Current measurements indicate that $\Omega_\Lambda^0 \sim 0.7$, demanding that $z_{eq} \sim 0.3$. Those redshifts such that $z < z_{eq}$ are dominated by dark energy, inhibiting structure formation. The variation of Equation 1.17 with dark energy density is not smooth and variations on this parameter lead to completely different results. An increase of the 20% on the dark energy density leads to a value of $z_{eq} = 2.7$, preventing structure formation, whereas a decrease of the 20% leads to $z_{eq} = -0.1$, indicating the universe is still matter dominated, preventing the detection of cosmic expansion. This fine tuning issue indicates that there must be some mechanism that couples dark energy and matter. Anthropic arguments can be made, stating that the value of the dark energy density has the value we measure since it is the only possible compatible with the detection of cosmic acceleration and structure formation.

1.2.2 Exotic matter fields

Since no satisfactory explanation has been found on the vacuum to explain dark energy, the presence on new quantum fields that, on the simplest case, interact only through gravity, but on more complicated scenarios may also couple arbitrarily with the other matter fields can be considered.

The simplest case is known as quintessence and is defined as a scalar field that is added to the Lagrangian defined at Equation 1.3 such that such that

$$\mathcal{L}[g_{\mu\nu}] = \sqrt{g} (g^{\mu\nu} R_{\mu\nu}(g) + \mathcal{L}_\phi) \quad \text{with} \quad \mathcal{L}_\phi = -\frac{1}{2} g^{\mu\nu} \partial_\mu \phi \partial_\nu \phi - V(\phi), \quad (1.18)$$

where $V(\phi)$ is the potential of the field. On an FLRW metric, this leads to a substance with density and pressure

$$P_\phi = \frac{1}{2} \dot{\phi}^2 - V(\phi) \quad \text{and} \quad \rho_\phi = \frac{1}{2} \dot{\phi}^2 + V(\phi). \quad (1.19)$$

This can be parametrized as an ideal fluid with equation of state

$$w_{DE} = \frac{P_\phi}{\rho_\phi} = \frac{\dot{\phi}^2 - 2V(\phi)}{\dot{\phi}^2 + 2V(\phi)}. \quad (1.20)$$

Thus, it can be deduced that dark energy critical density evolves with the scale factor of the universe as

$$\Omega_\Lambda(t) = \Omega_\Lambda^0 [a(t)]^{-3(1+w_\phi)}. \quad (1.21)$$

The only possible candidate for dark energy as quintessence within the Standard Model of Particle Physics is the Higgs field, a complex scalar-field that fills the Universe and couples to gauge bosons giving them its mass. The potential of the field is given by

$$V(\phi) = \mu_H^2 \phi^\dagger \phi + \frac{1}{4} \lambda_H (\phi^\dagger \phi)^2, \quad (1.22)$$

with μ_H the mass term, λ_H the self-interaction of the field and ϕ, ϕ^\dagger the Higgs field and its hermitian conjugate respectively. Since the potential of the field is time independent, this leads to an equation of state

$$w_{DE} = \frac{-2V(\phi)}{2V(\phi)} = -1, \quad (1.23)$$

recovering the cosmological constant solution. Thus, cosmological constant can be interpreted as the expected value of Higgs field at vacuum

$$\langle 0 | \phi_0 | 0 \rangle = \frac{|\mu_H|}{\sqrt{\lambda_H}} = \sqrt{\frac{1}{\sqrt{2} G_F}} = 246 \text{ GeV}, \quad (1.24)$$

where G_F is the Fermi constant, that can be computed from the decay of the muon. The connection between the decay of the muon and the Higgs field comes from the fact that the decay is mediated by vector bosons, whose mass is given by the Higgs field:

$$\mu^- \rightarrow W^- + \nu_\mu \text{ and } W^- \rightarrow e^- + \bar{\nu}_e. \quad (1.25)$$

Other High Energy Physics scalar potentials can be built from physics beyond the Standard Model, such us supergravity [29–31], where a scalar potential can be found such that

$$V(\phi) = M^{4+n} \phi^{-n} \exp(\alpha \phi^2 / m_P^3), \quad (1.26)$$

which has a minimum with $w_{DE} \simeq -0.8$, close to the cosmological constant value. Within a supersymmetry breaking framework, a field with potential

$$V(\phi) = M^{4+n} \phi^{-n} \quad (1.27)$$

can be introduced [32]. Nevertheless most of the phase space of supersymmetry and supergravity has been excluded by latest LHC results.

The existence of an ultra-light Pseudo-Nambu-Goldstone Boson may be postulated with an associated field with potential [33, 34]

$$V(\phi) = M^4 \cos^2(\phi/f). \quad (1.28)$$

Light-massive Pseudo-Nambu-Goldstone Bosons can be found as exotic forms of matter such as axions and schizons, whose existence is far from being probed.

More complicated field models can be considered increasing the number of fields and letting them interact and will not be considered here since they are beyond the scope of this Thesis. A detailed description of all the models can be found at [35]. Nevertheless, a general phenomenological description can be made in terms of the equation of state of dark energy,

$$P_{DE} = w_{DE}\rho_{DE} \quad (1.29)$$

expanding the parameter w_{DE} in a power series of the scale factor

$$w_{DE}(t) = w_0 + w_a[1 - a(t)], \quad (1.30)$$

where w_0 denotes the value of the equation of state parameter at present and w_a is evolution –at first order– with time. The cosmological constant may be considered as an specific solution of this equation of state where

$$w_0 = -1 \quad \text{and} \quad w_a = 0. \quad (1.31)$$

1.2.3 Modified Gravity

Attempts to explain the existence of a cosmological constant from High Energy Physics side, leads to a tension between General Relativity and the Standard Model. Possible new exotic fields that may explain late-time cosmic acceleration are walking a tightrope due to latest LHC results from physics beyond the Standard Model.

The remaining approach to explain the accelerated expansion of the Universe is to consider General Relativity as an approximate gravitational theory on the same way Newtonian gravity is the low-energy limit of Einstein’s gravity. Extensions to General Relativity are known as modified gravity models. This kind of models were born as alternate theories to dark matter as explanation of Vera Rubin’s measurements of the rotation curve of spiral galaxies [36–39].

The first theory is Milgrom’s Modified Ordinary Newtonian Dynamics (MOND) and its relativistic extensions [40–43], that suggest that Newton’s second law is not valid on galactic scales, not requiring the existence of dark matter. Although some tests on galactic scales support MOND [44, 45], this paradigm can not explain the Bullet Cluster [46–48] (see Figure 1.5). Recently Verlinde proposed a new theory that postulates gravity as a consequence of quantum entanglement at the microscopic level [49]. Although, this theory recovers MOND results for point masses, it has been rapidly put in tension with the measurement of the rotation

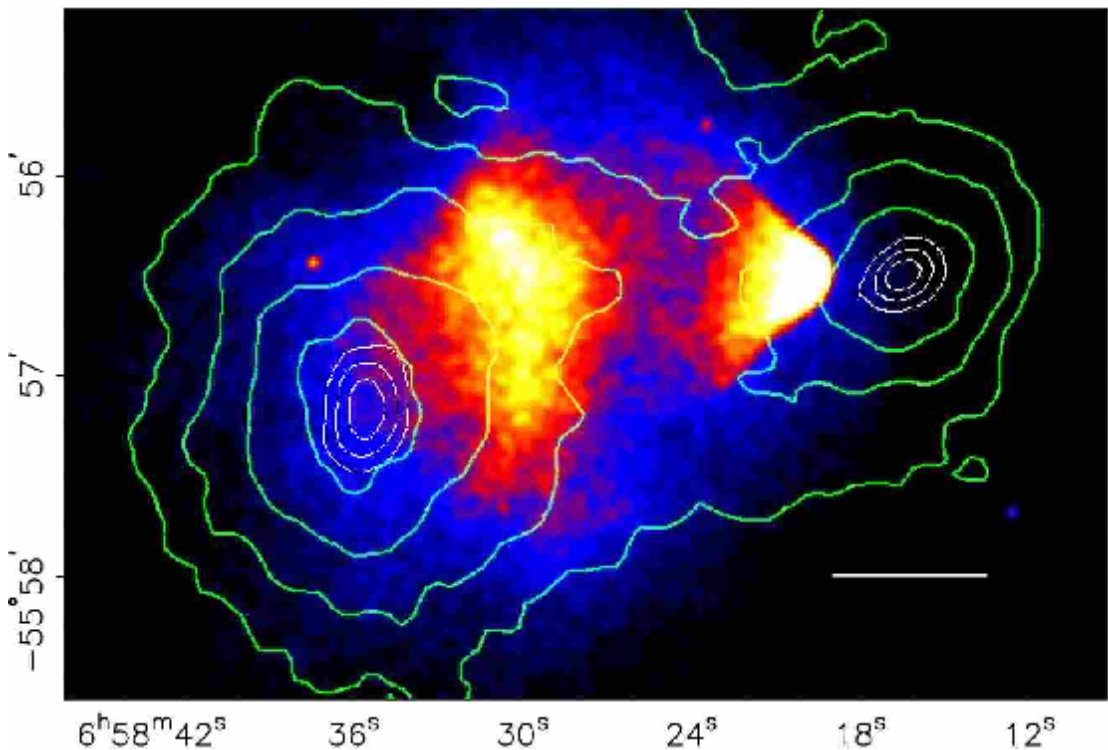


Figure 1.5: Bullet cluster. Colors indicate the barionic mass measured with gamma-rays, whereas the solid lines indicate the mass reconstructed with gravitational lensing. This result is considered the clearest probe of the existence of dark matter and that it is decoupled from barionic matter. Image taken from [51].

curve of galaxies [50].

More elaborated theories that do not break the equivalence principle can be made. One class of those theories is known as $f(R)$ gravity [52, 53], and its approach is to let the Lagrangian to be a general function (f) of the Ricci scalar, $R = g^{\mu\nu}R_{\mu\nu}$:

$$\mathcal{L}[g_{\mu\nu}] = \frac{c^4}{16\pi G_N} \sqrt{-g} f(R), \quad (1.32)$$

that leads to the field equation

$$R_{\mu\nu} - \frac{1}{2}Rg_{\mu\nu} = \frac{8\pi G_N}{c^4}(T_{\mu\nu} + T_{\mu\nu}^R). \quad (1.33)$$

This field equation is similar to Equation 1.3 but has an additional term $T_{\mu\nu}^R$ that takes into account the additional curvature terms that can be modeled as a fluid on the same way as the energy-momentum tensor. The simplest case is $f(R) = R + \alpha R^n$ with $\alpha, n \in \mathbb{R}$. It has interesting cosmological solutions [54], nevertheless the latest studies on the large-scale-structure of the Universe, favor Λ CDM over $f(R)$ models [55] although a range of n can not still be fully discarded. This theory has very distinctive phenomenology such as double Einstein rings on the strong lensing regime [56] that –if found– could be the smoking gun of these kind of theories.

More complicated models of modified gravity can be considered but are not going to be treated here since they are beyond of the scope of this Thesis. For a review it can be consulted [57]. The usual approach to explore the modifications to General Relativity [58] are to model the departures of the metric. On the Newtonian gauge, the FLRW line element of can be parametrized with the Newtonian and the lensing potential; Φ, Ψ respectively [58]:

$$ds^2 = a^2(\tau)[-(1 + 2\Phi)d\tau^2 + (1 - 2\Phi)dx_i dx^j], \quad (1.34)$$

with

$$2\nabla^2\Phi(a, k) = \frac{8\pi G_N}{c^2}a^2\mu(a, k)\bar{\rho}_M\delta_M(a, k) \quad \text{and} \quad \gamma(a, k) = \frac{\Phi(a, k)}{\Psi(a, k)}, \quad (1.35)$$

where $\bar{\rho}_M$ is the average matter density, δ_M its fluctuations and k is the wavenumber of the potentials. Here μ and γ parametrize the departures from General Relativity, that is the specific case with

$$\mu(a, k) = 1 \quad \text{and} \quad \gamma(a, k) = 1. \quad (1.36)$$

It is important to remark that the zoo all the departures from General Relativity plus cosmological constant –including the addition of new fields–, may be unified into a single parametrization known as Parametrized Post-Friedmann Framework [59].

1.3 Current status of Dark Energy constraints

The latest and more precise results constraining dark energy are provided by the Planck Collaboration 2015 results from the analysis of the Cosmic Microwave Background (CMB) [60].

Dark energy as an exotic form of matter, is determined by measuring the parameters of the equation of state (w_0, w_a) and their value can be seen at Figure 1.6. The results provided are compatible with General Relativity plus cosmological constant, the uncertainty on the parameters of the equation of state does not allow to exclude many models, specifically the type of models that predict a value of the equation of state close to that of the cosmological constant but whose equation of state evolves with cosmic time –or equivalently, redshift–, since current precision on the determination of this evolution is still very poor as it can be deduced from Figure 1.7. Constraints on Modified Gravity models are also given in terms of the modified gravity potentials μ, η and Σ . As it can be deduced from Figure 1.8 and Figure 1.9, General Relativity plus cosmological constant is not excluded but, as in the case of the fluid equation, the measurements are not precise enough to discard many modified gravity models.

Although the Planck Collaboration 2015 results seem to favor cosmological constant as dark energy, Riess et al. latest direct determination of the Hubble constant using the cosmological distance ladder (parallax-cepheids-SNIa) [61], show a discrepancy on the 3σ level with the Hubble constant measured by Planck Collaboration 2015. If more exotic cosmological scenarios are considered, such as non-flatness, additional species of neutrinos or other models of dark energy are allowed, this tension is relaxed.

CFHTLens & KiDS-450 Collaborations galaxy-shear weak-lensing analysis show tension on the $\Omega_M - \sigma_8$ plane with Planck Collaboration 2013 [62] and 2015 CMB measurements if a General Relativity plus cosmological constant scenario is considered [63, 64]. This tension may be alleviated if other models are considered, such as non-zero curvature and dark energy models [65]. Nevertheless, discrepancies could also be produced by systematic effects [66, 67].

A weak-lensing analysis by Leauthaud et al. [68] of CFHTLens & CMASS data using gg-lensing show a lower signal amplitude than the one predicted measuring the clustering of the lens sample. In addition gg-lensing measurements on the $\Omega_M^0 - \sigma_8$ plane have a discrepancy on the 3σ level with Planck Collaboration 2013 measurements on a cosmological constant scenario. Nevertheless, discrepancies are interpreted in terms of new physics on the astronomy side: halo occupation distribution (HOD) and barionic physics.

As it has been described, current individual constraints on dark energy are not precise enough to determine which model is the correct explanation of the accelerated expansion of the Universe. Current cosmological model –General Relativity with flat geometry plus cosmological constant (flat- Λ CDM)–, is in crisis

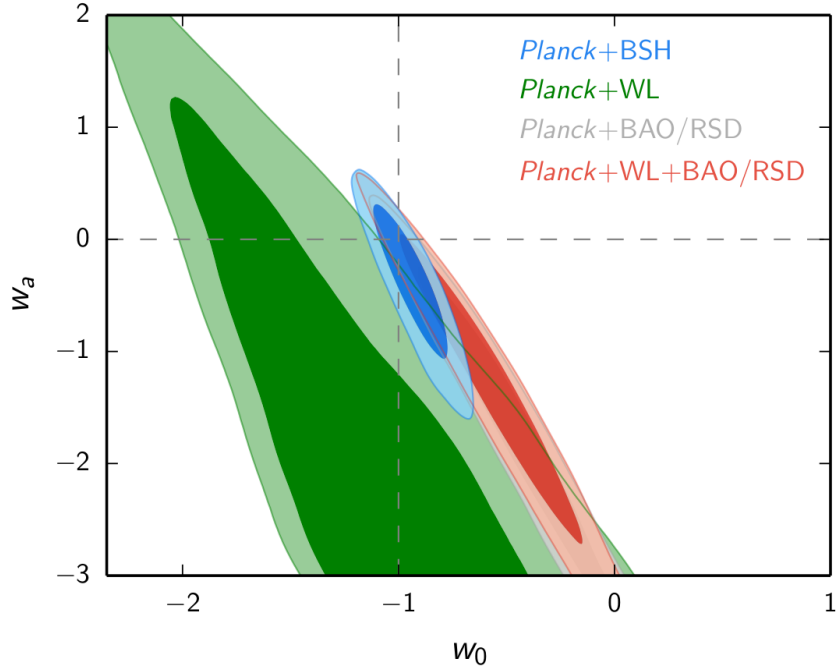


Figure 1.6: One- and two- sigma contours of the equation of state of dark energy w_0, w_a . The intersection of dashed lines is the cosmological constant. Results obtained from Planck Collaboration 2015 results [60].

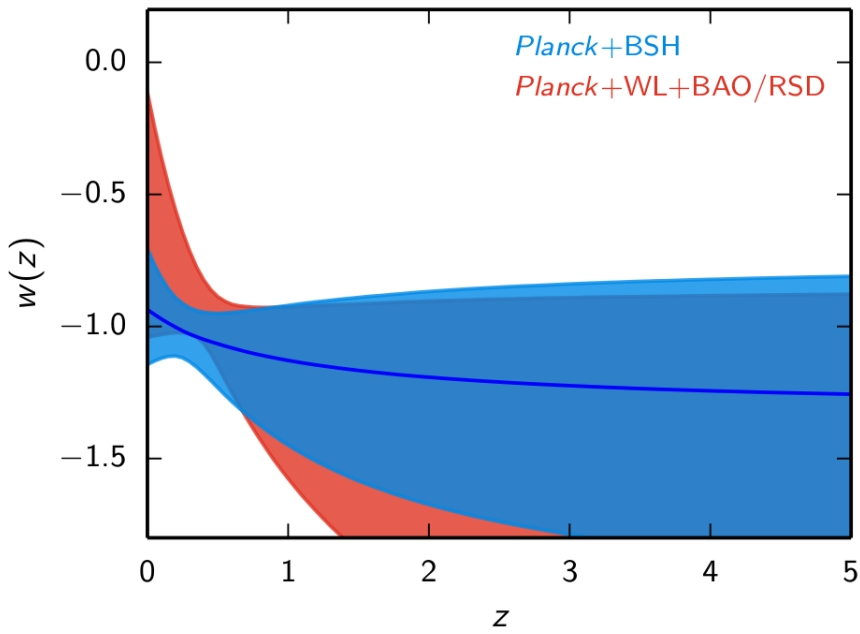


Figure 1.7: One-sigma confidence interval of the equation of state of dark energy as a function of redshift $w_{DE}(z)$ and one-sigma confidence interval. Results obtained from Planck Collaboration 2015 results [60].

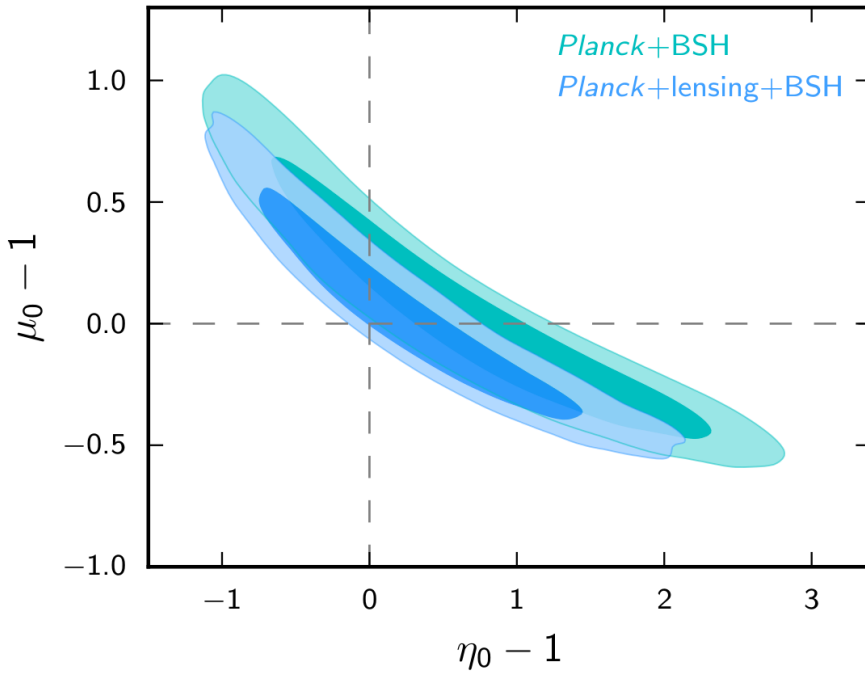


Figure 1.8: One- and two- sigma modified gravity potentials at present μ_0, η_0 . Dashed line is General Relativity plus cosmological constant. Results obtained from Planck Collaboration 2015 results [60].

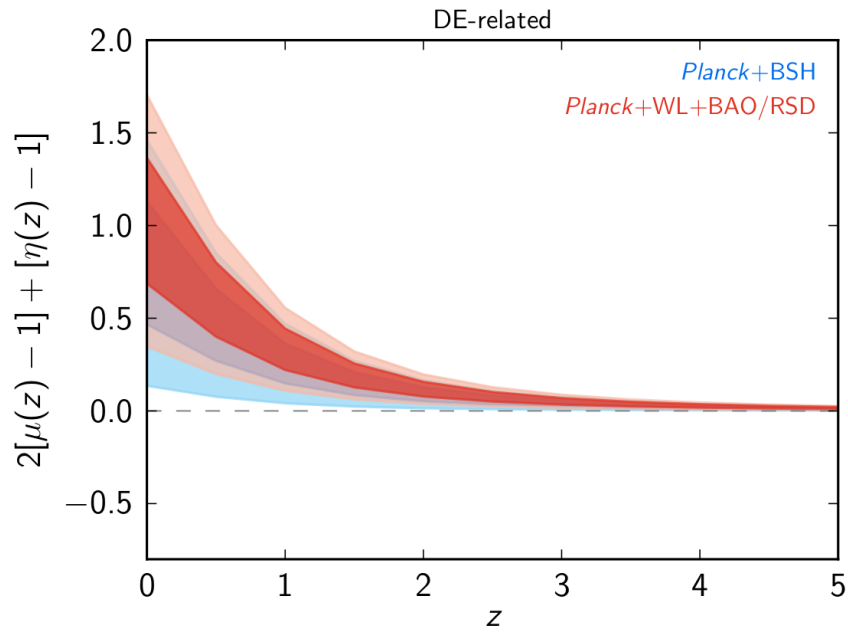


Figure 1.9: One- and two- sigma of the sum of the modified gravity potentials. Dashed line is General Relativity plus cosmological constant. Results obtained from Planck Collaboration 2015 results [60].

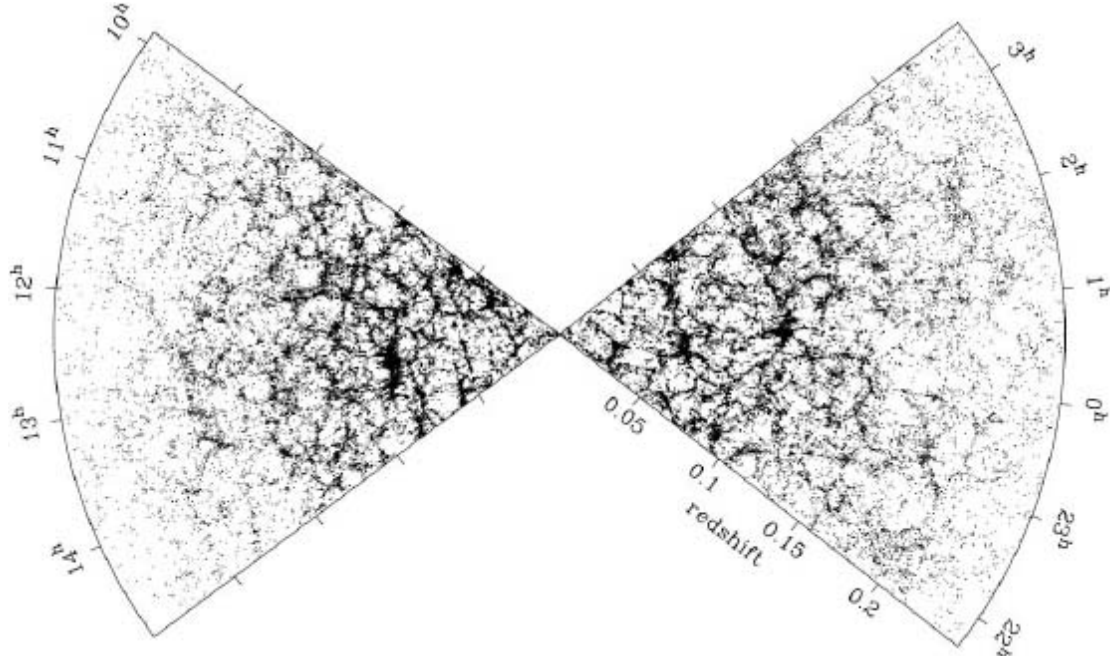


Figure 1.10: Large-scale-structure of the Universe. Each dot represents the position of a galaxy. Image credit: 2 Degree Field Survey.

since a tension exists between different probes [69]. Dark energy is one of the possible scenarios to solve this tension, although caution is needed and analysis need to put special attention to systematic analysis. This requires additional probes and redundant measurements of the same physical observable but with different sources of systematic errors.

1.4 Alternative probes for Dark Energy: Voids & Troughs

Previous cosmological probes were based on the same physical quantity: the anisotropies of the matter density-field although at different moments of the Cosmic History. Whereas CMB measures anisotropies at decoupling, lensing and clustering measure them at present. This anisotropies where originated on primordial density fluctuations² that, when matter and radiation decoupled, froze. Then, the over-dense regions of the mater field started to grow by gravitational collapse of the matter, leading the the accretion of the matter contained at the under-dense regions, forming the cosmic web (see Figure 1.10). This large under-dense regions of the Universe surrounded by over-dense regions are known as voids.

Since voids have a lower matter content than the average Universe, their gravitational evolution is dominated by dark energy. Thus, void properties are different depending on the dark energy theory that rules the Cosmos. If the abundance of large voids on the Universe is considered, it has been reported that its number increases in $f(R)$ gravity models [70] since the abundance of dark matter halos is altered [71]. Nevertheless, if the shape of the void is measured, its ellipticity

²The current hypothesis suggests that this fluctuations are due to inflation.

can be used as a probe for the parameters of the equation of state of dark energy [72–75], since the structure growth-factor on the line-of-sight has a variation due to the dark energy content, whereas on the transverse plane, growth-factor is constant. Finally, the radial distribution of matter around the center of a void –known as void profile– has demonstrated to be different on $f(R)$ theories and General Relativity [76–81]. Thus, by simply measuring the void matter profile, constraints on dark energy can be made.

Nevertheless, the total matter budget of the Universe is composed by both barionic and dark matter, being the presence of the latter only accessible indirectly through its gravitational effects. As galaxies –mainly composed by barionic matter– are biased tracers of the underlying dark matter field, its spatial distribution requires a model of assembly of galaxies within dark matter, introducing uncertainties and nuisance parameters on the model. Gravitational light deflection is only sensitive to the total matter field, not needing additional modeling on how barionic and dark matter relate. Thus, gravitational light deflection made by voids constitutes a promising new probe on dark energy.

2. Gravitational Lensing Theory

One of the most astonishing conclusions of General Relativity is that the presence of masses curl the space-time. This ripples on the 4-dimensional space, force the other bodies within it to move. Thus, a gravitational field is just the expression of a non-uniform local¹ curvature. The main consequence of this, is that massless particles are also affected by Gravity.

As part of the four Fundamental Forces, the specific property of Gravity among the others, is that the charge of the sources of the field is always positive². The consequence of this, is that the gravitational force is always attractive. Thus, if a stream of photons with parallel trajectories goes through a massive point-particle, all the trajectories will be deflected towards it. This bending of the photons trajectories is produced coherently such that the point-particle can be considered as a convergent optical lens.

2.1 Lens Equation on Gravitational Fields

As stated before, the axis observer-mass constitute an optical system. Thus a lens equation can be deduced following the same approach as Geometrical Optics with the deflection angle ($\hat{\alpha}$) of a light ray –photon trajectory– given by General Relativity [82–88]:

$$\hat{\alpha} = \frac{4G_N M}{rc^2}. \quad (2.1)$$

Here M is the mass of the point-particle (lens hereafter), G_N is Newton's constant, c the speed of light and r the closest encounter distance (a.k.a. impact parameter). Using Figure 2.1 as reference and defining θ as the observed and β the real lens-

¹Local in the cosmological sense. Here it can mean the scale of the size of a cluster.

²There are experiments probing this statement. Until now, no evidence of negative masses.

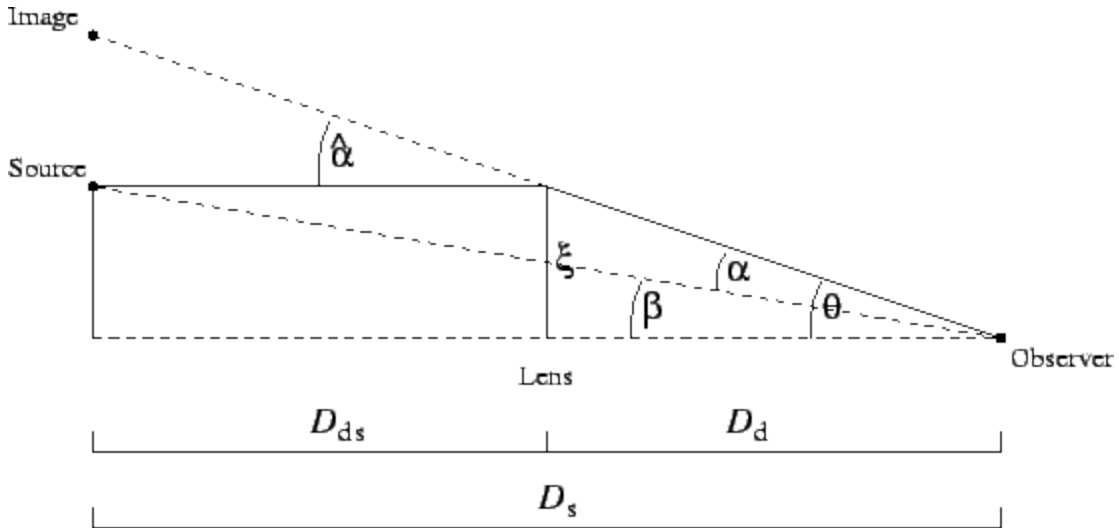


Figure 2.1: Optical system of the gravitational lensing caused by a point mass. Solid line is the actual photon trajectory. Dashed lines are the apparent trajectories with and without lensing. The distances D_s , D_d , D_{ds} are expressed in comoving coordinates.

source angle, it can be deduced that

$$\beta = \theta - \frac{D_{ds}}{D_s} \hat{\alpha}(D_d \theta) = \theta - \alpha(\theta), \quad (2.2)$$

where D_{ds} , D_s and D_d are the source-lens, observer-source and observer-lens comoving distances.

Considering now an extended matter distribution, with density $\rho(\vec{r})$, where the observer is located at the origin. The position vector can be splitted such that

$$\vec{r} = r_{\parallel} \hat{r}_{\parallel} + \vec{r}_{\perp}, \quad (2.3)$$

where $r_{\parallel} \hat{r}_{\parallel}$ denotes the position on the direction defined by the axis observer-lens (line-of-sight or LoS hereafter) and \vec{r}_{\perp} denotes a 2D vector on the plane transverse to the line-of-sight. Thus, the total matter distribution that the photon goes through from the source to the observer is given by

$$\Sigma(\vec{r}_{\perp}, r_{\parallel}^S) = \int_0^{r_{\parallel}^S} dr_{\parallel} \rho(r_{\parallel}, \vec{r}_{\perp}), \quad (2.4)$$

where \vec{r}^S is the position of the source and the quantity Σ is called the surface density. Taking into account the flat-sky approximation –that is, all the transverse planes to LoS are parallel– and summing to all the lens positions, Equation 2.1 becomes

$$\hat{\alpha}(\vec{r}_{\perp}, r_{\parallel}^S) = \frac{4G_N}{c^2} \int d^2 \vec{r}_{\perp} \Sigma(\vec{r}_{\perp}, r_{\parallel}^S) \frac{\vec{r}_{\perp}^S - \vec{r}_{\perp}}{|\vec{r}_{\perp}^S - \vec{r}_{\perp}|^2}. \quad (2.5)$$

This leads to a deflection angle

$$\vec{\alpha}(\vec{r}_\perp, r_\parallel^S) = \frac{1}{\pi} \int d^2 \vec{r}_\perp \kappa(\vec{r}_\perp, r_\parallel^S) \frac{\vec{r}_\perp^S - \vec{r}_\perp}{|\vec{r}_\perp^S - \vec{r}_\perp|^2}, \quad (2.6)$$

where the convergence (κ) and critical density (Σ_c) has been defined such that

$$\kappa(\vec{r}_\perp, r_\parallel^S) = \frac{\Sigma(\vec{r}_\perp, r_\parallel^S)}{\Sigma_c} \text{ with } \Sigma_c = \frac{c^2}{4\pi G_N} \frac{D_s}{D_d D_{ds}}. \quad (2.7)$$

Defining the lensing potential as

$$\psi(\vec{r}_\perp, r_\parallel^S) = \frac{1}{\pi} \int d^2 \vec{r}_\perp \kappa(\vec{r}_\perp, r_\parallel^S) \ln |\vec{r}_\perp^S - \vec{r}_\perp|, \quad (2.8)$$

the deflection angle can be written as the gradient of the lensing potential on the transverse plane

$$\vec{\alpha}(\vec{r}_\perp, r_\parallel^S) = \nabla_\perp \psi(\vec{r}_\perp, r_\parallel^S) \quad (2.9)$$

and the convergence as its laplacian,

$$\kappa(\vec{r}_\perp, r_\parallel^S) = \frac{1}{2} \nabla_\perp^2 \psi(\vec{r}_\perp, r_\parallel^S). \quad (2.10)$$

Thus, the lens equation from Equation 2.2 results

$$\vec{\beta} = \vec{\theta} - \nabla_\perp \psi(\vec{r}_\perp, r_\parallel^S). \quad (2.11)$$

Taking into account the definition of the lensing potential, it can also be written in terms of the Newtonian gravitational potential (Φ):

$$\psi(\vec{r}_\perp, r_\parallel^S) = \frac{D_{ds}}{D_s D_d c^2} \int dr_\parallel^S \Phi(D_d \vec{r}_\perp, r_\parallel^S). \quad (2.12)$$

Thus, gravitational lensing is a direct probe for the underlying gravitational field.

2.2 Weak Gravitational Lensing

In addition to the change in the observed position of the source, considering no absorption nor emission of photons between the source and the observer, Liouville's theorem implies that the surface brightness of the source (I_S) is conserved,

$$I_S(\vec{r}_\perp) = I_S[\vec{\beta}(\vec{r}_\perp)]. \quad (2.13)$$

Considering the weak-field regime, the lensing map can be linearized such that

$$I_S(\vec{r}_\perp) = I_S[\vec{\beta}_0 + \mathcal{J}(\vec{r}_{\perp 0})(\vec{r}_\perp - \vec{r}_{\perp 0})], \quad (2.14)$$

where $\mathcal{J}(\vec{r}_\perp)$ is the jacobian matrix. By the integration-by-substitution theorem of calculus, the integral of the surface brightness at the lensed and un-lensed coordinate systems are related by

$$\int I_S(\vec{\beta}) d\vec{\beta} = \det(\mathcal{J}) \int I_S[\vec{\beta}(\vec{r}_\perp)] d\vec{r}_\perp, \quad (2.15)$$

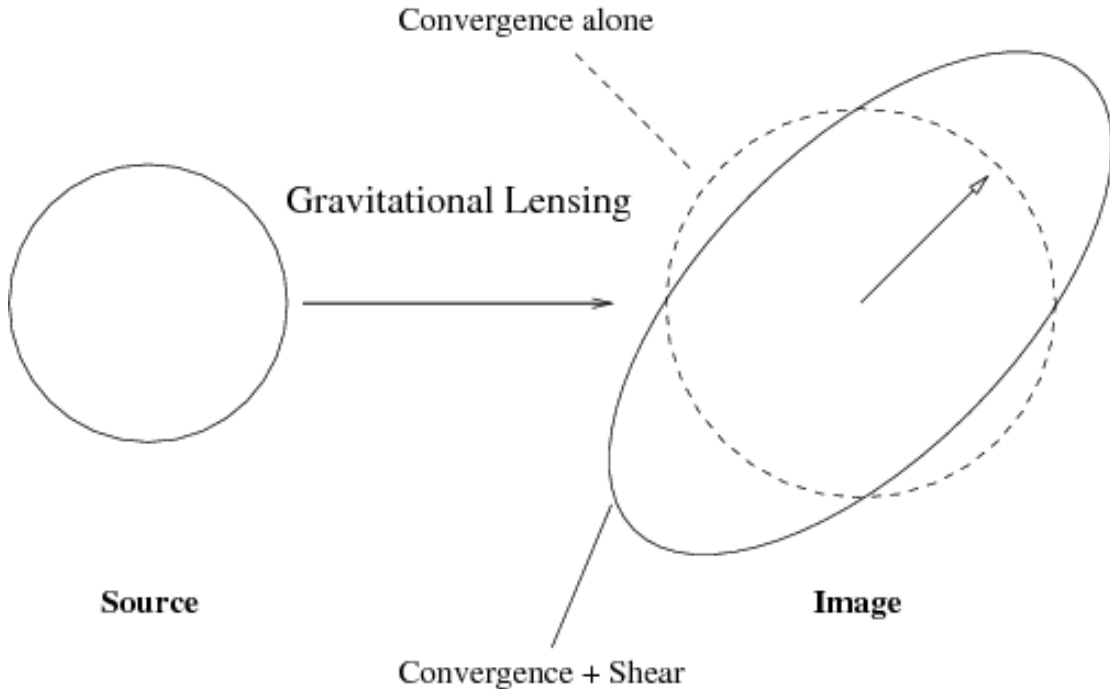


Figure 2.2: Weak-lensing distortion of an extended spherical object. Convergence leads to an isotropic enlargement, whereas shear produces an elongation/shrink along one axis.

where $\det(\mathcal{J})$ denotes the determinant of the jacobian matrix. Thus, defining the luminosity of an extended object as the integral of its surface brightness, the luminosity for the cases with and without gravitational lensing (L_μ, L_0 respectively) are related by

$$L_\mu = \frac{1}{\det(\mathcal{J})} L_0 = \mu L_0, \quad (2.16)$$

where μ is called the magnification factor and is defined as de inverse of the determinant of the jacobian matrix of the lensing map.

Taking into account that the jacobian matrix is given by $\mathcal{J} = (\hat{n}_\perp \cdot \nabla_\perp) \vec{\beta}$ with \hat{n}_\perp a unit vector on the plane transverse to LoS, by Equation 2.11 the jacobian can be expressed as

$$\mathcal{J} = (\hat{n}_\perp \cdot \nabla_\perp) \vec{r}_\perp - \mathcal{J} = (\hat{n}_\perp \cdot \nabla_\perp) \nabla \psi, \quad (2.17)$$

resulting finally

$$\mathcal{J}(\vec{r}_\perp) = \left(\delta_{ij} - \frac{\partial^2 \psi}{\partial r_i \partial r_j} \right) = \begin{pmatrix} 1 - \kappa - \gamma_1 & -\gamma_2 \\ -\gamma_2 & 1 - \kappa + \gamma_1 \end{pmatrix}. \quad (2.18)$$

Here κ is the convergence, an isotropic shape distortion and γ_1, γ_2 is the shear, an elongation/shrink on the shape along one of the axis (Figure 2.2).

Taking into account the Born approximation –that is, the light rays of a source galaxy are deflected by only one lens–, the derivatives of the previous equation can be evaluated on the unlensed coordinates.

2.2.1 Magnification

As it has been demonstrated at the previous section, gravitational lensing increases the observed luminosity on an extended object [89–93] such that $L_\mu = \mu L_0$ with

$$\mu = \frac{1}{(1 - \kappa)^2 + \gamma_1^2 + \gamma_2^2} \simeq 1 + 2\kappa, \quad (2.19)$$

where on the last step it has been used that $1 \gg \kappa \gg \gamma$. Taking into account the definition given at Equation 2.7, the convergence suffered by the photons emitted by a source located on the sky direction \hat{n} and redshift z is given by

$$\kappa(\hat{n}, z) = \frac{1}{2} \frac{\Sigma(\hat{n}, z)}{\Sigma_c}. \quad (2.20)$$

Using the definition given at Equation 2.4 and the poisson equation for the gravitational field this leads to

$$\kappa(\hat{n}, z) = \int_0^z dz' \frac{r(z')[r(z) - r(z')]}{r(z)} \nabla_\perp \Phi(\hat{n}, z'), \quad (2.21)$$

where $r(z)$ is the comoving distance at redshift z and Φ the gravitational potential. Expressing now the gravitational potential as an homogeneus therm plus a perturbation ($\Phi = \bar{\Phi} + \delta_\Phi$), the previous equation can be expressed as a funcion of the matter density contrast (δ_M)

$$\nabla^2 \Phi(\hat{n}, z) = \nabla^2 \delta_\Phi(\hat{n}, z) = 4\pi G a^2 \bar{\rho} \delta_M(\hat{n}, z), \quad (2.22)$$

where $a = 1/(1 + z)$ is the scale factor and $\bar{\rho}$ is the average density. This leads finally to

$$\kappa(\hat{n}, z) = \frac{3H_0 \Omega_M}{2} \int_0^z dz' \frac{r(z')[r(z) - r(z')]}{(1 + z')r(z)} \delta_M(\hat{n}, z). \quad (2.23)$$

The convergence, is the physical observable of Magnification and it traces the matter on the direction of line of sight whereas shear proves the matter on the transverse direction. This makes magnification and shear complementary measurements of the same phenomena. The dependence of magnification is usually splitted into two pieces: the lensing kernel,

$$\mathcal{K}(z) = \frac{r(z')[r(z) - r(z')]}{(1 + z')r(z)}. \quad (2.24)$$

and the matter density contrast (δ_M). The lensing kernel only contains only geometrical information and, for a given Cosmology, it is fixed. On the other side, the matter density contrast depends strongly on the population of galaxies selected as lens sample. This dependence on the selected lens sample, has been exploited in the past to measure magnification itself maximizing the signal-to-noise ratio and to trace the matter profiles on a HOD framework.

The convergence of the foreground sample can be probed tracing the three effects that it produces on the background sample:

- **Change of the observed density:** The increase of the observed luminosity of the galaxies, allows to see sources that if there were no lensing, would be below our observational threshold nearby the location of the lenses. At the same time, an stretching of the solid angle behind the lenses causes a drop in the number density. This two effect compete between them and who is over the other depends on the slope of the number counts of the sources. Thus, at the neighborhood of the lenses, a change of the number density respect to the average is produced. This is known as number-counts magnification.
- **Shift on the observed magnitude:** Since the increase of luminosity due to gravitational lensing, is a short range effect, a shift on the observed magnitudes may be detected nearby the positions of the lenses. This requires, in principle, the knowledge of the unlensed magnitude of the sources. Nevertheless, although galaxies have a large variety of magnitudes, it can be assumed that, they are randomly distributed. Thus shifts on the magnitudes respect to the average can be detected.
- **Size enlargement:** All the effects above are a consequence that the meanwhile surface brightness is conserved, a size enlargement is produced. This effect can be statistically measured despite the fact that the unlensed size is not known. Nevertheless, since galaxies have a large variety of shape and size that is strongly related to its evolution and age, no homogeneity assumption can be made and require the definition of the *fundamental plane*. That kind of work is beyond the scope of this Thesis and further information can be found at Huff& Graves.

Traditionally all this probes has been used independently, but the ideal would be a three-way combination since each method is sensitive to a different kind of systematic.

As it has been mentioned before, the knowledge of the unlensed properties of the sources is physically impossible. Thus all the observable quantities must be formulated in terms of changes of its variation respect the ensemble average with the distance to the lenses. The statistical way to do this is the two-point angular correlation-function (2pacf hereafter). This method, provides a measurement of the average convergence profile of the lenses ($\kappa(\theta)$) as a function of its angular distance θ of a point to the lens .

Estimation of $\kappa(\theta)$ with the number counts technique

The 2pacf between the lens (L) and the source (S) is defined as

$$\omega_{LS}(\theta) = \langle \delta_O(\hat{n}, z_L, f_\mu) \delta_O(\hat{n}', z_S, f_\mu) \rangle_\theta. \quad (2.25)$$

Where $\delta_O(\hat{n}, z_L, f_\mu)$ is the observed galaxy density-contrast on the sky direction \hat{n} and redshift z_L with flux limit f_μ . Since due to magnification galaxies beyond the observable threshold will appear nearby the lenses introducing a non-uniform distribution of galaxies. Thus the observed galaxy density contrast can be expressed as

$$\delta_O(\hat{n}, z, f_\mu) = \delta_g(\hat{n}, z) + \delta_\mu(\hat{n}, z, f_\mu), \quad (2.26)$$

where δ_g is the intrinsic galaxy-density contrast (that is, without magnification) and δ_μ is the density contrast due to magnification. Thus Equation 2.25 becomes

$$\omega_{LS}(\theta) = \langle \delta_g(z_L)\delta_g(z_S) \rangle + \langle \delta_g(z_L)\delta_\mu(z_S) \rangle + \langle \delta_\mu(z_L)\delta_g(z_S) \rangle + \langle \delta_\mu(z_L)\delta_\mu(z_S) \rangle. \quad (2.27)$$

Taking into account that $0 < z_L < z_S$, and that the lens and the source sample are well redshift separated, the only non vanishing term is

$$\omega_{LS}(\theta) = \langle \delta_g(\hat{n}, z_L)\delta_\mu(\hat{n}, z_L, f_\mu) \rangle_\theta. \quad (2.28)$$

Let define the magnification density contrast on the sky direction \hat{n} as

$$\delta_\mu(\hat{n}, z, f_\mu) = \frac{N_\mu(\hat{n}, z, f_\mu)}{N_0(\hat{n}, z, f_0)} - 1, \quad (2.29)$$

where $N_0(\hat{n}, z, f_0)$ is the un-lensed cumulative number counts of sources located at redshift z , that is, the number of sources with observed flux greater than the threshold f_0 . Conversely, $N_\mu(\hat{n}, z, f_\mu)$ is the lensed cumulative number counts affected by magnification.

Magnification by gravitational lenses increases the observed flux of background objects allowing to see fainter sources by an amount $f_\mu = f_0/\mu$. At the same time, it stretches the solid angle behind the lenses, reducing the surface density of sources an amount $N_\mu = N_0/\mu$, which translates into the density contrast as a power law:

$$\delta_\mu(\hat{n}, z, f_\mu) = \frac{N_\mu(\hat{n}, z, f_\mu)}{\mu N_\mu(\hat{n}, z, f_\mu)} - 1. \quad (2.30)$$

The cumulative number counts can be locally parametrized as

$$N_\mu(\hat{n}, z, f_\mu) = A \left(\frac{f_\mu}{f_*} \right)^{\alpha(f_\mu)}, \quad (2.31)$$

where A, f_* are constant parameters and $\alpha(f_\mu)$ a function of the flux limit. Substituting this into Equation 2.30

$$\delta_\mu(\hat{n}, z, f_\mu) = \mu^{\alpha(f_\mu)-1} - 1. \quad (2.32)$$

Taking into account $\mu \simeq 1 + 2\kappa$ along with Equation 2.19 and translating from fluxes to magnitudes

$$\delta_\mu(\hat{n}, z, m) = 2\kappa(\hat{n}, z)[\alpha(m) - 1] \quad (2.33)$$

with

$$\alpha(m) = 2.5 \frac{d}{dm} [\log N_\mu(m)]. \quad (2.34)$$

Thus Equation 2.25 becomes

$$\omega_{LS}(\theta) = 2[\alpha(m) - 1]\langle \delta_g(\hat{n}, z_L)\kappa(\hat{n}, z_S) \rangle_\theta. \quad (2.35)$$

Using the definition of convergence as a function of the galaxy density contrast given at Equation 2.23 and assuming a constant redshift-independent galaxy-bias, $\delta_g(\hat{n}, z_L) = b_L \delta_M(\hat{n}, z_L)$, this leads finally to

$$\omega_{LS}(\theta) = b_L [\alpha(m) - 1] \omega_0(\theta), \quad (2.36)$$

where b_L is the galaxy-bias of the lens sample and

$$\omega_0(\theta) = \frac{3H_0\Omega_M}{2} \int_0^\infty dz' \mathcal{K}(z') \langle \delta_g(\hat{n}, z_L) \delta_g(\hat{n}', z') \rangle_\theta. \quad (2.37)$$

Estimation of $\kappa(\theta)$ with magnitude-shift magnification technique

The magnitude-position-angular correlation function (mpac hereafter) between the lens sample (L) and the source sample (S) is defined as

$$\varphi_{LS}(\theta) = \langle \delta_g(z_L, \hat{n}) \delta_m(z_S, \hat{n}') \rangle_\theta. \quad (2.38)$$

Where, as on the last section $\delta_g(z, \hat{n})$ is the galaxy density contrast at redshift z on the sky direction \hat{n} and δ_m is the magnitude shift³, defined as

$$\delta_m(z, \hat{n}) = m_\mu(\hat{n}, z) - m_0(\hat{n}, z), \quad (2.39)$$

where m_μ is the lensed magnitude and m_0 the unlensed magnitude. Taking into account that, as it has been demonstrated previously

$$f_\mu(\hat{n}, z) = \mu(\hat{n}, z) f_0(\hat{n}, z) \Leftrightarrow m_\mu(\hat{n}, z) - m_0(\hat{n}, z) = -2.5 \log \mu(\hat{n}, z), \quad (2.40)$$

where on the last step it has been converted from fluxes to magnitudes. Thus, taking into account that

$$\log(\mu) \simeq \log(1 + 2\kappa) \simeq 2\kappa, \quad (2.41)$$

the Equation 2.38 results finally

$$\varphi_{LS}(\theta) = -5 \langle \delta_g(\hat{n}, z_L) \kappa(\hat{n}', z_S) \rangle = -2.5 b_L \omega_0(\theta), \quad (2.42)$$

where $\omega_0(\theta)$ is defined at Equation 2.37.

Nevertheless, reddening by the inter-galactic medium can also produce –unlike gravitational lensing– wavelength-dependent magnitude-shifts such that the lensed-plus-reddened fluxes are

$$f_\mu(\hat{n}, z, \lambda_\eta) = \mu(\hat{n}, z) f_0(\hat{n}, z) e^{-\tau(\lambda_\eta)}, \quad (2.43)$$

that converted to magnitudes results in

$$m_\mu(\hat{n}', z, \lambda_\eta) - m_0(\hat{n}', z, \lambda_\eta) = -2.5 \log \mu + \frac{2.5}{\ln 10} \tau(\lambda_\eta), \quad (2.44)$$

³Do not confuse with δ_M , the matter density contrast.

where $\tau(\lambda_\eta)$ is the optical depth at the wavelength λ_η . The dust and the lensing components can be disentangled by defining the color-excess angular correlation function ($E^{\eta\nu}$) between two-wavelengths $\lambda_\eta, \lambda_\nu$,

$$E_{LS}^{\eta\nu}(\theta) = \langle \delta_g(\hat{n}, z_L)[m_\mu(\hat{n}', z_S, \lambda_\eta) - m_\mu(\hat{n}', z_S, \lambda_\nu)] \rangle_\theta. \quad (2.45)$$

Since gravitational lensing is acromatic, the only dependence with the wavelength comes from the extinction law

$$E_{LS}^{\eta\nu}(\theta) = \frac{2.5}{\ln 10} \langle \delta_g(\hat{n}, z_L)[\tau(\hat{n}', z_S, \lambda_\eta) - \tau(\hat{n}', z_S, \lambda_\nu u)] \rangle. \quad (2.46)$$

Modeling the wavelength dependence of the optical depth as

$$\tau_\eta = \tau(\lambda_\eta) = \tau_V \left(\frac{\lambda_V}{\lambda_\eta} \right), \quad (2.47)$$

where τ_V is the optical depth at the V -band filter, λ_V is the wavelength of the V -band filter and $\gamma \sim 1$ is a constant parameter. Thus, the color-excess cross-correlation results finally

$$E_{LS}^{\eta\nu}(\theta) = \lambda_V (\lambda_\eta^{-1} - \lambda_\nu^{-1}) \frac{2.5}{\ln 10} \langle \delta_g(\hat{n}, z_L) \tau_V(\hat{n}', z_S) \rangle. \quad (2.48)$$

At a wide field survey with several broad-band band-pass filters the scale dependence of the optical depth, $\tau_V(\hat{n}, z_S)$ can be constrained.

2.2.2 Shear

From the Jacobian of the lensing map, it can be deduced that the transformation is not isotropic producing an elongation along one of the axis $(r_1, r_2) = \vec{r}_\perp$. Thus, an intrinsically round galaxy is seen as elliptical. On the case of elliptical galaxies, statistically they present a global ellipticity. From the definition of Equation 2.18, the shear components are given by:

$$\gamma_1(\vec{r}_\perp) = -\frac{1}{2} \left(\frac{\partial^2 \psi}{\partial r_1^2} - \frac{\partial^2 \psi}{\partial r_2^2} \right) \text{ and } \gamma_2(\vec{r}_\perp) = -\frac{\partial^2 \psi}{\partial r_1 \partial r_2}. \quad (2.49)$$

The shear fields γ_1, γ_2 can be expressed as Fourier series such that:

$$\tilde{\gamma}_{1,2}(\vec{k}_\perp) = \int \gamma_{1,2}(\vec{r}_\perp) e^{-i\vec{k}_\perp \cdot \vec{r}_\perp} d^2 \vec{r}_\perp \quad (2.50)$$

and

$$\gamma_{1,2}(\vec{r}_\perp) = \frac{1}{(2\pi)^2} \int \tilde{\gamma}_{1,2}(\vec{k}_\perp) e^{i\vec{k}_\perp \cdot \vec{r}_\perp} d^2 \vec{k}_\perp. \quad (2.51)$$

Expressing the differential equation at the Fourier space with the usual approach $\partial/\partial r_1 \rightarrow ir_1$ it leads to

$$\gamma_1(\vec{k}_\perp) = \frac{1}{2}(r_1^2 - r_2^2)\tilde{\psi}(\vec{k}_\perp) \text{ and } \gamma_2(\vec{k}_\perp) = \frac{1}{2}r_1 r_2 \vec{\psi}(\vec{k}_\perp) \quad (2.52)$$

Considering a plane-wave perturbation of the lensing potential, it is useful to align the axis of the perturbation with those of the shear field such that

$$\tilde{\gamma}_E(\vec{k}_\perp) = \cos(2\phi_{\vec{k}_\perp})\tilde{\gamma}_1(\vec{k}_\perp) + \sin(2\phi_{\vec{k}_\perp})\tilde{\gamma}_2(\vec{k}_\perp) \quad (2.53)$$

and

$$\tilde{\gamma}_B(\vec{k}_\perp) = \cos(2\phi_{\vec{k}_\perp})\tilde{\gamma}_1(\vec{k}_\perp) - \sin(2\phi_{\vec{k}_\perp})\tilde{\gamma}_2(\vec{k}_\perp). \quad (2.54)$$

Resulting finally that

$$\tilde{\gamma}_E(\vec{k}_\perp) = \vec{k}_\perp^2 \tilde{\psi}(\vec{k}_\perp) \text{ and } \tilde{\gamma}_B(\vec{k}_\perp) = 0 \quad (2.55)$$

The fact that γ_B is zero, constitutes a necessary (but not sufficient) proof for the lack of systematic effects on any shear measurement.

Reaching this point, two kinds of two-point statistics can be build: the point-shear⁴ and the shear-shear two-point angular-correlation functions. From this two, we will only focus to gg-lensing due to its direct connection to magnification.

The gg-lensing.

Defining $\tilde{\epsilon}$ as the observed ellipticity, taking into account shear distortions it can be expressed as:

$$\tilde{\epsilon} = \tilde{\epsilon}_i + \tilde{\gamma}, \quad (2.56)$$

where $\tilde{\epsilon}_i$ is the intrinsic ellipticity of the galaxy. As stated previously, without loss of generality, shear coordinates can be rotated. Thus, let define the tangential shear γ_t as

$$\gamma_t = -[\cos(2\phi_{\vec{k}_\perp})\tilde{\gamma}_1(\vec{k}_\perp) + \sin(2\phi_{\vec{k}_\perp})]\tilde{\gamma}_2(\vec{k}_\perp) = -\gamma_E. \quad (2.57)$$

On the new coordinates, this leads to

$$\epsilon = \epsilon_i + \gamma_E, \quad (2.58)$$

where $\tilde{\epsilon}, \tilde{\epsilon}_i$ are the ellipticities on the new coordinates. Let $p(\epsilon)$ the distribution of ellipticites of the sources. At the small distortion regime, assuming that ellipticities are isotropic, it follows that

$$p(\epsilon) = p(\epsilon_i) + \gamma_t \cos 2\phi \frac{\partial p(\epsilon)}{\partial \epsilon}. \quad (2.59)$$

Here $\phi_{\vec{k}_\perp}$ is the angle of orientation of the principal axis of the galaxy. Integrating over all the ellipticities, they can be translated to orientation angle,

$$p(\phi) = \frac{2}{\pi} \left[1 - \langle \gamma_t \rangle \cos 2\phi \left\langle \frac{1}{\epsilon} \right\rangle \right]. \quad (2.60)$$

Thus, measuring the ellipticities –or orientation angles–, sear E-modes can be measured, probing directly the underlying lensing potential.

⁴This is usually called galaxy-galaxy- (or gg-) lensing.

2.3 The Kaiser-Squires inversion.

As it has been explained during the last sections, magnification traces the convergence field whereas ellipticities of galaxies trace the shear field. Both convergence and shear are produced by the same lensing potential, which is function of the spatial distribution of the matter content and the geometry of the problem –that is, the cosmological distances between the lens, source and observer–.

As it has been mentioned previously convergence and shear can be expressed at the Fourier space

$$\kappa(\vec{r}_\perp) \rightarrow \tilde{\kappa}(\vec{k}_\perp) = (k_1^2 + k_2^2)\tilde{\psi}(\vec{k}_\perp), \quad (2.61)$$

$$\gamma_1(\vec{r}_\perp) \rightarrow \tilde{\gamma}_1(\vec{k}_\perp) = \frac{1}{2}(k_1^2 - k_2^2)\tilde{\psi}(\vec{k}_\perp), \quad (2.62)$$

$$\gamma_2(\vec{r}_\perp) \rightarrow \tilde{\gamma}_2(\vec{k}_\perp) = \frac{1}{2}k_1k_2\tilde{\psi}(\vec{k}_\perp). \quad (2.63)$$

Taking into account that $\tilde{\psi}$ is the same on the three cases and defining the complex-shear as $\gamma = \gamma_1 + i\gamma_2$, the following relationship can be established,

$$\tilde{\kappa}(\vec{k}_\perp) = \tilde{\gamma}(\vec{k}_\perp)\tilde{\mathcal{D}}^*(\vec{k}_\perp) \text{ where } \tilde{\mathcal{D}}(\vec{k}_\perp) = \frac{k_1^2 - k_2^2 + 2ik_1k_2}{\vec{k}_\perp^2}. \quad (2.64)$$

Conversely, it may also be obtained

$$\tilde{\gamma}(\vec{r}_\perp) = \tilde{\kappa}(\vec{k}_\perp)\tilde{\mathcal{D}}(\vec{k}_\perp). \quad (2.65)$$

Thus, transforming to the real space one gets finally the following pair of equations, known as the Kaiser-Squires inversion:

$$\gamma(\vec{r}_\perp) = \frac{1}{\pi} \int_{\mathbb{R}^2} d^2\vec{r}'_\perp \mathcal{D}(\vec{r}_\perp - \vec{r}'_\perp) \kappa(\vec{r}'_\perp) \quad (2.66)$$

$$\kappa(\vec{k}_\perp) - \kappa_0 = \frac{1}{\pi} \int_{\mathbb{R}^2} d^2\vec{r}'_\perp \Re[\mathcal{D}^*(\vec{r}_\perp - \vec{r}'_\perp) \gamma(\vec{r}'_\perp)] \quad (2.67)$$

with

$$\mathcal{D}(\vec{r}_\perp) = \frac{-1}{(r_1 - ir_2)^2}. \quad (2.68)$$

This set of equations allows to relate the convergence and the shear field demonstrating this way that they are two sides of the same coin.



3. The Dark Energy Survey

The Dark Energy Survey (DES) [94] is a *grizY* photometric galaxy-survey that has as main scientific goal to give light on the nature of the Dark Energy. It is labeled as a stage III experiment by the Dark Energy Task Force (DETF) [95].

The four probes used by DES to unravel the nature of Dark Energy are: the number of clusters as a function of redshift, the measurement of the peak-scale of the barion acoustic oscillations (BAO), the weak gravitational lensing of galaxies and the measurement of the Hubble diagram with type Ia Supernovae (SNIa). By the end of five years of observations, DES will cover 5000 deg^2 of the Southern Hemisphere up to magnitude $i < 24.0$ at the 10σ detection level. Taking this into account, this survey is expected to measure 10000 clusters up to redshift 1.0, 200 million galaxy-shapes for weak-lensing, 300 million galaxies for BAO and 3000 SNIa up to redshift 1.0. Thus, each individual probe is not competitive by itself individually compared with specific experiments. Nevertheless, the power of DES resides on the combination of all the probes braking degeneracies on the cosmological parameter phase-space leading to a precision better than the 5% and 30% on the parameters w_0 and w_a respectively of the equation of state of the Dark Energy.

DES is an international collaboration formed by about 500 scientist from more than 20 institutions from: USA, Spain, UK, Brazil, Germany and Switzerland. The Collaboration has built a very sensitivity camera, DECam (see Figure 3.1 and Figure 3.2), that has been mounted at the 4-m Victor M. Blanco Telescope¹ at the Cerro Tololo Inter-American Observatory (CTIO). located at La Serena (Chile).

¹This is the same telescope where Schmidt and Perlmutter performed the observations leading to the Nobel Prize in 2010 for the discovery of Dark Energy.

3.1 The DECam

The DECam (Dark Energy Camera), is the main instrument of the experiment. It is composed mainly by:

- the 570 megapixel CCDs,
- low-noise readout electronics,
- wide-field optical corrector –producing 2.2 deg^2 field of view–,
- filter and shutter system,
- hexapod for stability.

Since the DES is going to observe very high redshifted galaxies, CCDs used by DES have been specifically designed at Lawrence Berkeley National Laboratory to detect red light. In order to do so, this CCDs are ten times thicker – $250 \mu\text{m}$ – than conventional ones². This results in a quantum efficiency of the 90% at wavelengths grater than 900 nm and about 60% at the rest. The DECam focal plane consist of the following types of CCDs:

- Science array: formed by 62 CCDs with 2048×4096 pixels. Each pixel is $15\mu\text{m}$ of side that, at Blanco Telescope, results on 0.27 arc-seconds on the sky.
- Four 2048×2048 guider CCDs.
- Eight 2048×2048 focus and alignment CCDs.

To minimize the noise and dark currents due to the electronic system, DECam operates on an environment cooled by liquid nitrogen at 180 K and a vacuum of $\sim 10^{-9}$ atm.

The whole readout process takes 17 seconds (about the same slewing-time of the telescope). Readout electronic boards were produced and designed in Spain at CIEMAT and IFAE.

3.2 Survey strategy

The total amount of time awarded to DES at CTIO period to reach the total area to the nominal depth on the five photometric bands is of 525 nights over a 5-year period. The rest of the nights the DECam is available to the scientific community. The tank-shaped footprint, that can be seen at Figure 3.3) is not casual but is optimized for the several probes.

- The *canyon* located at the equator, is known as stripe-82 and overlaps with several spectroscopic surveys such as SDSS, to calibrate the photometric redshifts (photo-z hereafter).
- The rounded shape –*the body*– is intended to have the largest available scale for BAO measurement.
- The lower part –*the wheels*– is designed to overlap with the South Pole Telescope (SPT) to measure the Sunyaev-Zeldovich effect.

The DES observations can be splitted in two: the transient survey and the wide-field survey.

²Sensitivity to long wavelengths is increased when passing through more silicon.



Figure 3.1: Location of the 4-m Victor Blanco Telescope at Cerro Tololo. Chilean Andes.

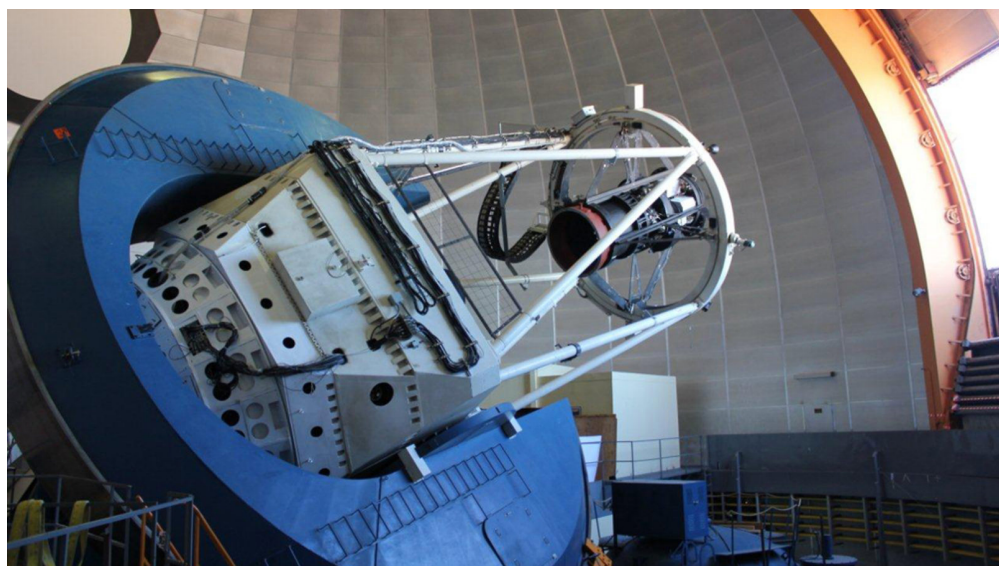


Figure 3.2: DECam mounted at the focus of the Victor Blanco Telescope.

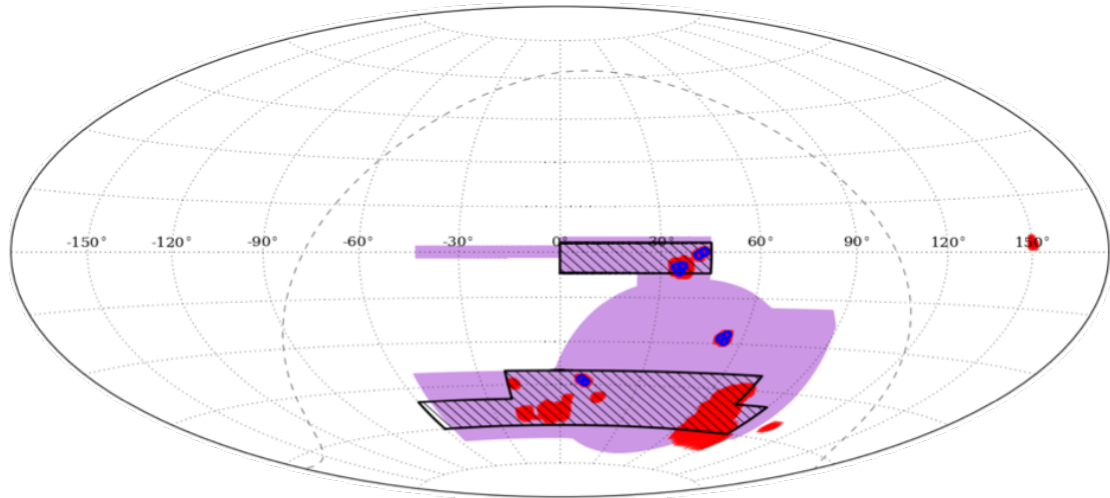


Figure 3.3: DES footprint on equatorial coordinates. Purple area is the total area that DES will cover at the end of the five years (Y5). Red areas -that overlap with the purple- are the Science Verification observations. Shaded areas are the first year campaign of observations (Y1). Dotted line represent the galactic plane.

3.2.1 The transient survey

The transient survey is designed to measure SNIa. Selected small portions of the sky –known as the supernovae fields– are surveyed from time to time to look for supernovae explosions by looking objects that are not always present and measure its luminosity curve as a function of time. Although it is designed to SNIa astronomy, some ancillary Solar-System astronomical results as been reported, such as Jupiter-trojan and trans-neptunian detection and searches for the known planet-9.

3.2.2 The wide-field survey

The wide field survey is intended for the rest of the probes for Dark Energy along with some Milky-Way astrophysics. To cover the whole footprint, the sky has been divided on a grid of half square-degree patches known as tiles. Each tile is visited XX times on each band along the 5-year-period to reach the full depth. The regions to survey are defined at the beginning of the campaign of observations and which band is observed at an specific night is decided based on the seeing and sky-brightness conditions of that night.

3.2.3 The night operations at CTIO

A typical night of observations, if sky is not overcast and no earthquake threatens the life of the observers, starts in the afternoon taking zeros of the camera and the dome-flats. Then, after the evening twilight, three standard stars are photographed to calibrate the photometry. After that, the wide-field survey starts. When the supernovae fields are visible, they are surveyed, returning to the wide-field survey when they are done. Some time before the morning twilight, other three standard stars are photographed, finishing the night. All the night operations are the same except if some gravity-wave has been detected by LIGO that, due to an agreement

with the LIGO Consortium, DES points to the place where the gravity-wave has been produced to look for an optical counterpart.

3.3 The data reduction pipeline

The data reduction that goes from images to science-ready catalogs of galaxies is carried at the NCSA. The first step involves is correct by the zeropoints and the dome flats the images taken and to calibrate them with the standard stars. This, are well known stars with very well defined and measured photometric properties. Then, the different exposures of the same tile for a given band –single-epoch images– are combined into a single image on a procedure called as co-addition –multi-epoch image–. This procedure allows the increase of the observed depth respect to each individual single-epoch image. This multi-epoch images will constitute the measurement images for each band. Nevertheless, to reach the DES nominal depth, images are detected on the image produced by the co-addition of the $r + i + z$ multi-epoch images. Co-additon of the objects is made by the software **Swerp** and the detection and photometric measurements is made with **SExtractor** in dual mode. Nevertheless, shape and photometry given by **SExtractor** does not reach the precision level required for the shear analysis, so the photometry for this analysis is made with **IM3SHAPE** and **NGMIX**.

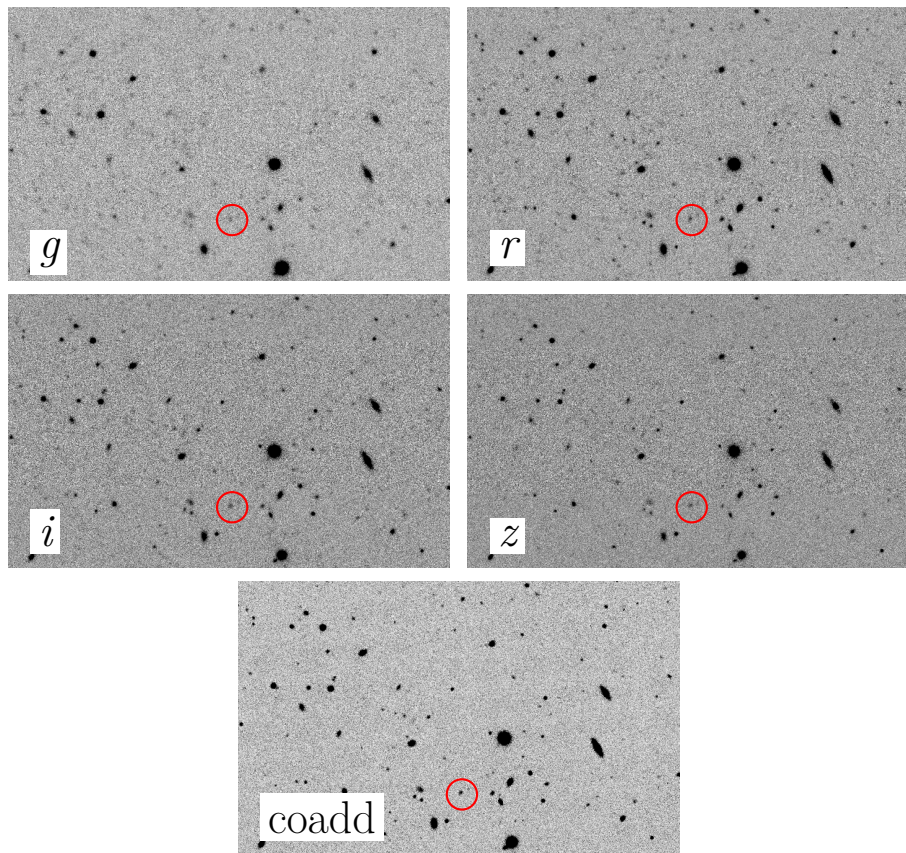


Figure 3.4: Comparison of the multi-epoch image for the $griz$ bands with the detection coadd. Images are taken from DES-database for a region of the tile DES0419-4914 after the Y1 epoch. Red circle denotes an object that is detected at the coadd image but at the individual image is not.



4. Magnification in DES

Extensive wide-field programs have allowed accurate measurements of weak lensing effects. Previous magnification measurements involve the use of very massive objects as lenses, such as luminous red galaxies (LRGs) and clusters [96–99], or high redshift objects as sources, such as Lyman break galaxies (LBGs) [100, 101], quasars ([102–107] and sub-mm sources [108] to improve signal-to-noise ratio. In addition to the number count technique used in this paper, other observational effects produced by magnification have been measured as well: the shift in magnitude [109], flux [110] and size [111].

On this chapter, first the methodology to measure magnification is tested with simulations. Then, the methodology is used to measure the magnification signal at the Dark Energy Survey Science Verification data (SV). Finally, the methodology used at the DES-SV data is employed to measure the convergence profile of voids and troughs

4.1 Magnification in the MICE-GC simulation

4.2 Magnification in DES Science Verification data

As it has been described at the gravitational lensing theory section, the amplitude of the magnification signal is dependent on two factors: the number-count slope parameter ($\alpha - 1$) and the lensing kernel, that for a given lens sample, depends on the redshift of the source sample. LBGs has been traditionally used on magnification studies since they have an steep magnitude distribution, leading to a high value of $\alpha - 1$. In addition, this population of galaxies is located at very high redshift ($2 \lesssim z \lesssim 4$), leading to a high lensing efficiency. Nevertheless, this population of galaxies has much less density than the general population of galaxies, feature that can prevent the measurement of a magnification signal for low-area surveys. In addition, the selection of a population of LBGs involve the known as *dropout* technique, that requiere the development of a custom data-reduction pipeline just

to select this specific population of galaxies. For large-area surveys such as DES, the amount of computing time to run the data-reduction pipeline is enormous (~ 1 year), reaching manpower and infrastructure difficulties. On the other side, although LRGs do not require a custom pipeline and a template-based approach to select them from the galaxy-catalogs provided by DES standard pipeline, its density is also very low.

As of January 2014 –when I started my PhD–, the only data available at DES was the Science Verification data. The first data-release from DES. This data where taking just for testing purposes and in order to explore the capabilities of the experiment. Thus, although the nominal depth of the survey was reached, only ~ 150 deg 2 where taken. Taking this into account, only 10^4 LBGs are expected at the full DES-SV data, preventing the measurement of magnification.

In order to be capable to reach a detection of the magnification signal with the DES-SV data, the general population of galaxies was selected both as lens and source sample. This leads to technical difficulties, since DES has a low precision on the redshift determination and the general population of galaxies is mainly located at low redshift, complicating the possibility to reach a clean redshift separation.

4.2.1 Data sample

The sample used in this analysis corresponds to the Science Verification (DES-SV) data, which contains several disconnected fields. From the DES SVA1-Gold¹ main galaxy catalog [112], the largest contiguous field is selected, the SPT-E. Regions with declination $< -61^\circ$ are removed in order to avoid the Large Magellanic Cloud. MODEST_CLASS is employed as star-galaxy classifier [113].

The following colour cuts are made in order to remove outliers in colour space:

- $-1 < g - r < 3$,
- $-1 < r - i < 2$,
- $-1 < i - z < 2$;

where g , r , i , z stand for the corresponding MAG_AUTO magnitude measured by SExtractor [114].

Regions of the sky that are tagged as bad, amounting to four per cent of the total area, are removed. An area of radius 2 arcminutes around each 2MASS star is masked to avoid stellar halos ([2005MNRAS.361.1287M]; [107]).

The DES Data Management ([115]; [116]; [117]) produces a MANGLE² [118] magnitude limit mask that is later translated to a $N_{\text{side}} = 4096$ HEALPIX³ [119] mask. Since the HEALPIX mask is a division of the celestial sphere with romboid-like shaped pixels with the same area, to avoid boundary effects due to the possible mismatch between the MANGLE and HEALPIX masks, each pixel is

¹des.ncsa.illinois.edu/releases/SVA1

²<http://space.mit.edu/~molly/mangle/>

³healpix.jpl.nasa.gov

required to be totally inside the observed footprint as determined by MANGLE, by demanding

- $r_{\text{fracdet}} = 1$,
- $i_{\text{fracdet}} = 1$,
- $z_{\text{fracdet}} = 1$;

where $r_{\text{fracdet}}, i_{\text{fracdet}}, z_{\text{fracdet}}$ is the fraction of the pixel lying inside the footprint for r, i, z bands respectively.

Depth cuts are also imposed on the riz -bands in order to have uniform depth when combined with the magnitude cuts. These depth cuts are reached by including only the regions that meet the following conditions:

- $r_{\text{lim}} > 23.0$,
- $i_{\text{lim}} > 22.5$,
- $z_{\text{lim}} > 22.0$;

where $r_{\text{lim}}, i_{\text{lim}}, z_{\text{lim}}$ stand for the magnitude limit in the corresponding band, that is, the faintest magnitude at which the flux of a galaxy is detected at 10σ significance level. The resulting footprint, as shown in Figure 4.1, after all the masking cuts amounts to 121 deg^2 .

Photometric redshifts (photo-z) have been estimated using different techniques. In particular, the fiducial code used in this work employs a machine-learning algorithm (random forests) as implemented by TPZ [120], which was shown to perform well on SV data [121]. The redshifts of the galaxies are defined according to the mean of the probability density functions given by TPZ (z_{ph}). Other methods are also employed to demonstrate that the measured two-point angular cross-correlation are not a feature induced by TPZ).

Lens sample

A unique lens sample is defined by the additional photo-z and magnitude cuts:

- $0.2 < z_{\text{ph}} < 0.4$;
- $18.0 < i < 22.5$.

These requirements are imposed in order to be compatible with the first redshift bin of the so called ‘benchmark sample’ [112]. Note that the MAG_AUTO cut along with the previous i -band depth cut guarantees uniformity [112].

Source sample

Three source samples are defined, one per band:

- R: $0.7 < z_{\text{ph}} < 1.0$ and $r < 23.0$;
- I: $0.7 < z_{\text{ph}} < 1.0$ and $i < 22.5$;
- Z: $0.7 < z_{\text{ph}} < 1.0$ and $z < 22.0$.

Following the same approach we used on the lens, defined over the ‘benchmark’ sample, the MAG_AUTO cut along with the previously defined depth cuts also guarantee uniformity on the corresponding band. Within each R, I, Z source sample five sub-samples that map the magnitude evolution are defined,

- $R_1: r < 21.0$; $R_2: r < 21.5$; $R_3: r < 22.0$; $R_4: r < 22.5$; $R_5: r < 23.0$.
- $I_1: i < 20.5$; $I_2: i < 21.0$; $I_3: i < 21.5$; $I_4: i < 22.0$; $I_5: i < 22.5$.
- $Z_1: z < 20.0$; $Z_2: z < 20.5$; $Z_3: z < 21.0$; $Z_4: z < 21.5$; $Z_5: z < 22.0$.

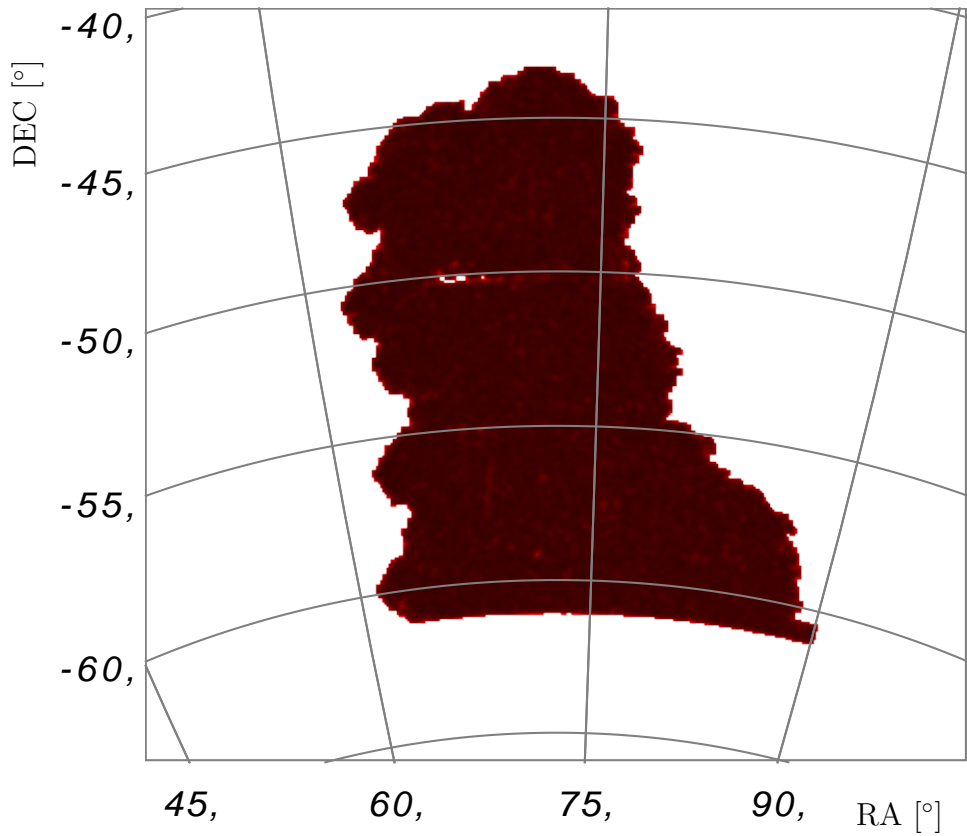


Figure 4.1: Final footprint of the DES SPT-E region after all masking is applied.

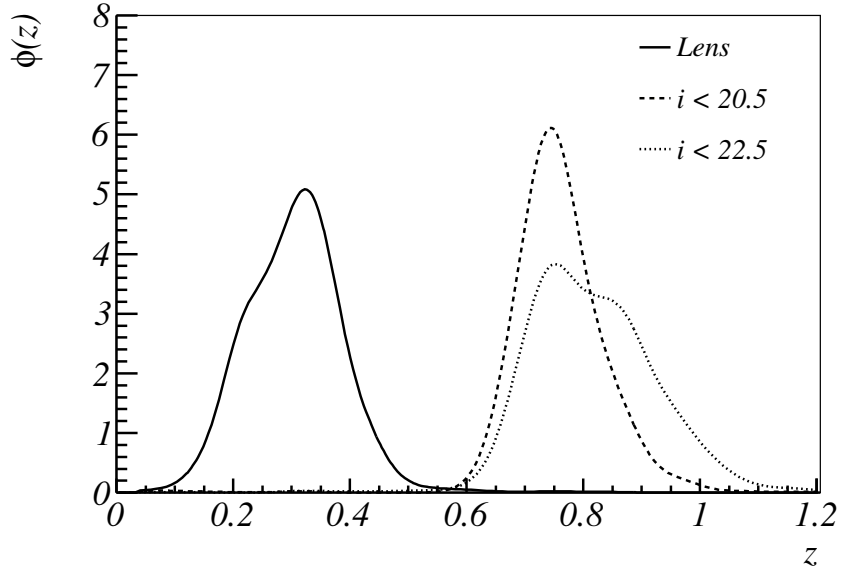


Figure 4.2: Redshift distributions from the stacking of the TPZ probability distribution functions for the lens and two i -band sub-samples of the source.

Here S_j with $j = 1, 2, 3, 4, 5$ are the sub-samples of sample $S \in \{R, I, Z\}$. In Figure 4.2, the redshift distributions of the lens and source sample are shown. Note that the sub-samples R_5, I_5, Z_5 are equal to R, I, Z respectively.

The g -band is not used on this analysis because when the same approach is followed and a uniform sample is defined in that band, the number of galaxies of the lens and source samples decrease dramatically. This increases the shot noise preventing the measurement of number count magnification

4.2.2 Detection of the weak-lensing magnification signal

To estimate the cross-correlation functions, the tree-code `TREECORR`⁴ [122] and the Landy-Szalay estimator [123] are used demanding six logarithmic angular bins:

$$\omega_{LS_j}(\theta) = \frac{D_L D_{S_j}(\theta) - D_L R_{S_j}(\theta) - D_{S_j} R_L(\theta)}{R_L R_{S_j}(\theta)} + 1, \quad (4.1)$$

where $D_L D_{S_j}(\theta)$ is the number of pairs from the lens data sample L and the source data sub-sample S_j separated by an angular distance θ and $D_L R_{S_j}(\theta)$, $D_{S_j} R_L(\theta)$, $R_L R_{S_j}(\theta)$ are the corresponding values for the lens-random, source-random and random-random combinations normalized by the total number of objects on each sample.

Catalogs produced with `BALROG`⁵ [124] are used as random samples. The `BALROG` catalogs are DES-like catalogs, where no intrinsic magnification signal has been included. The `BALROG` software generates images of fake objects, all with zero convergence κ , that are embedded into the DES-SV coadd images (convolving the objects with the measured point spread function, and applying the measured photometric calibration). Then `SEXTRACTOR` was run on them, using the same DES Data Management configuration parameters used for the image processing. The positions for the simulated objects were generated randomly over the celestial sphere, meaning that these positions are intrinsically unclustered. Hence, the detected `BALROG` objects amount to a set of random points, which sample the survey detection probability. For a full description and an application to the same measurement as in [112] see [124]. This is the first time that this extensive simulation is used to correct for systematics. The same cuts and masking of the data sample (??) are also applied to the the `BALROG` sample. A re-weighting following a nearest-neighbours approach was applied to `BALROG` objects in order to follow the same magnitude distribution of the DES-SV data on both lens and sources.

A covariance matrix is computed for each band by jack-knife re-sampling the data taking into account the correlations between the different magnitude cut

⁴github.com/rmjarvis/TreeCorr

⁵github.com/emhuff/Balrog

within each band

$$C_S(\omega_{LS_i}(\theta_\eta); \omega_{LS_j}(\theta_\nu)) = \frac{N_{JK}}{N_{JK} - 1} \times \sum_k^{N_{JK}} [\omega_{LS_i}^k(\theta_\eta) - \omega_{LS_i}(\theta_\eta)][\omega_{LS_j}^k(\theta_\nu) - \omega_{LS_j}(\theta_\nu)], \quad (4.2)$$

where $\omega_{LS_j}^k$ stands for the cross-correlation of the k -th jack-knife re-sample and ω_{LS_j} is the cross-correlation of the full sample. The $N_{JK} = 120$ jack-knife regions are defined by a k -means algorithm [125] using Python's machine learning library SCIKIT-LEARN⁶ [126]. In order to get N_{JK} regions with equal area, the algorithm is trained on a uniform random sample following the footprint of the data demanding N_{JK} centres. The regions used on the re-sampling are composed by the Voronoi tessellation defined by these centres. These matrices trace the angular covariance as well as the covariances between functions within each band. No covariance between bands is considered, since each band is treated independently on this work. The reduced covariance matrix of the i -band is displayed at Figure 4.3. The behavior is similar for the other bands.

Measured two-point angular cross-correlation functions and Λ CDM weak lensing theoretical predictions can be found in ???. Measured correlation functions are found to be non-zero, compatible with Λ CDM and its amplitude evolves with the magnitude cut. The magnitude cuts imposed to guarantee uniform depth make that, for this data, no negative amplitudes are expected.

To compare with the expected theory, ?? has been used assuming [**2016A&A...594A..13P**] cosmological parameters. The bias of the lens sample has already been measured independently with different techniques: clustering [112], gg-lensing [**2016arXiv160908167P**], shear [**2016MNRAS.459.3203C**] and CMB-lensing [127]. From these values the most precise, from [112], is selected ($b_L = 1.07 \pm 0.08$) and is assumed to be a constant scale-independent parameter. The number count slope parameter α_S is computed by fitting the cumulative number count of the sample S to a Schechter function [128] on the range of interest

$$N_\mu(m) = A [10^{0.4(m-m_*)}]^\beta \times \exp[-10^{0.4(m-m_*)}], \quad (4.3)$$

where A, m_*, β are the free parameters of the fit. Then $\alpha_S(m) - 1$ is computed by applying ??, where m_j is the magnitude limit of the S_j sub-sample on the considered band. In Figure 4.7 the fit and the number count slope parameter for the I sample are shown.

A goodness of fit test of the measured two-point angular cross-correlation function respect to the theoretical predictions for each band is performed:

$$\chi_{\text{Planck}}^2 = \sum_{\eta\nu ij} [\tilde{\omega}_{LS_i}(\theta_\eta) - \omega_{LS_i}(\theta_\eta)] \quad (4.4)$$

$$C^{-1}(\omega_{LS_i}(\theta_\eta); \omega_{LS_j}(\theta_\nu))[\tilde{\omega}_{LS_j}(\theta_\nu) - \omega_{LS_j}(\theta_\nu)], \quad (4.5)$$

⁶scikit-learn.org

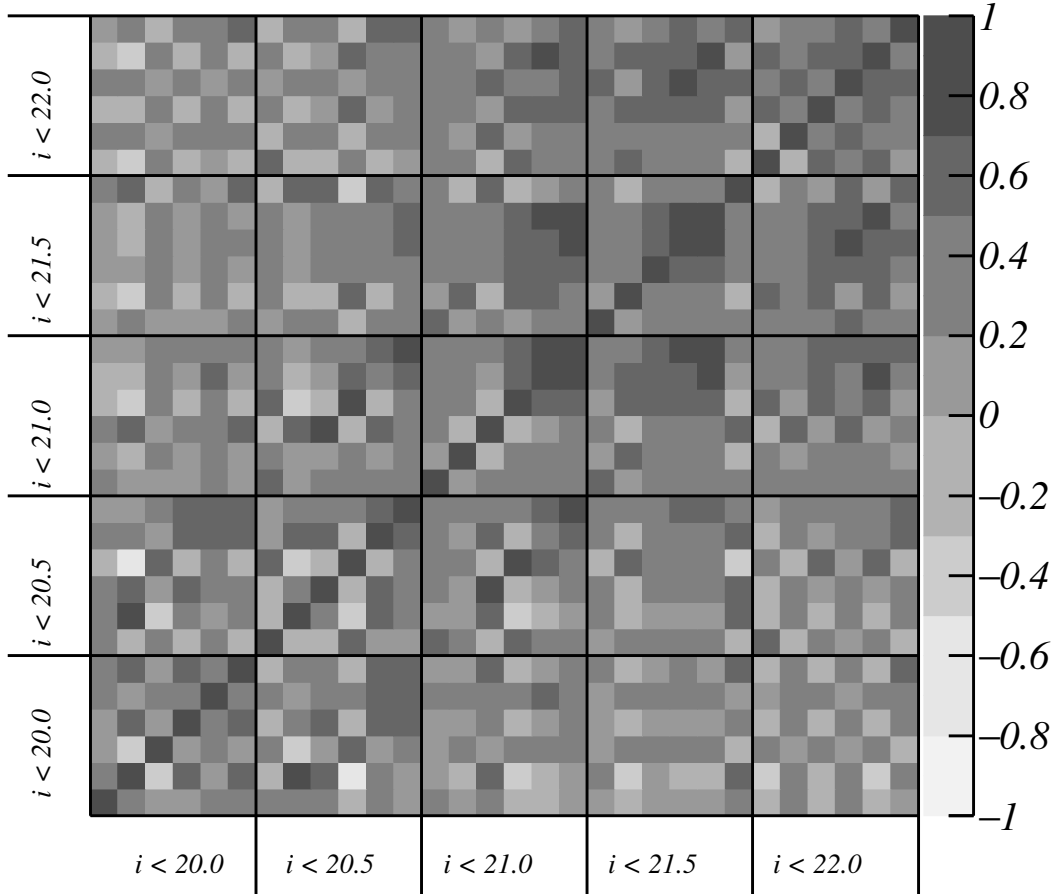


Figure 4.3: Covariance matrix of the i -band rescaled by the value of the diagonal ($C_{ij}/\sqrt{C_{ii}C_{jj}}$). Each box is the part of the matrix corresponding to the samples labeled at the axis whereas the bins within each box stand for the angular values of the correlation function.

Weight	Sample	$\log_{10} \mathcal{B}$	$\chi^2/ndof$
No	R	3.9	21.6/30
	I	3.4	23.9/30
	Z	3.4	36.8/30
Yes	$r < 23.0$	3.2	3.2/6
	$i < 22.5$	2.1	2.1/6
	$z < 22.0$	2.3	2.3/6

Table 4.1: Significance of the detection of a magnification signal. Results are shown for the combination of the five subsamples within each band as well as for the faintest sample with weighting.

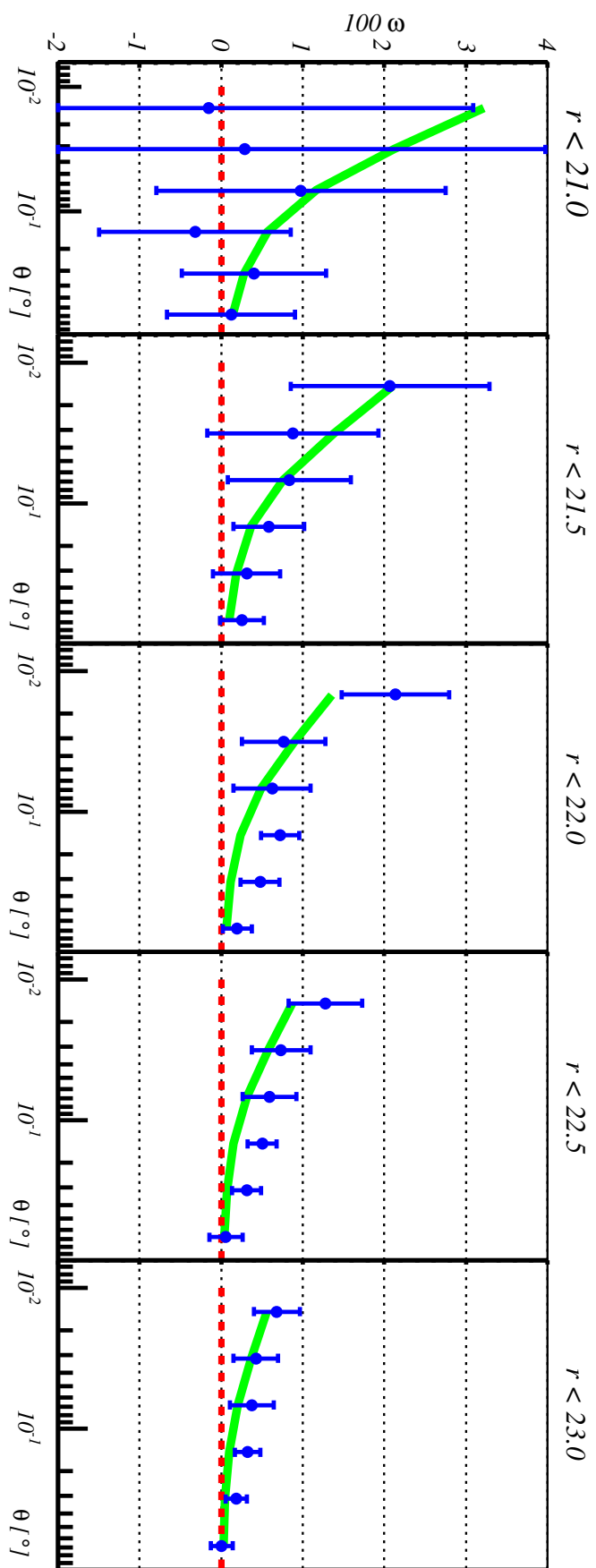


Figure 4.4: CONA

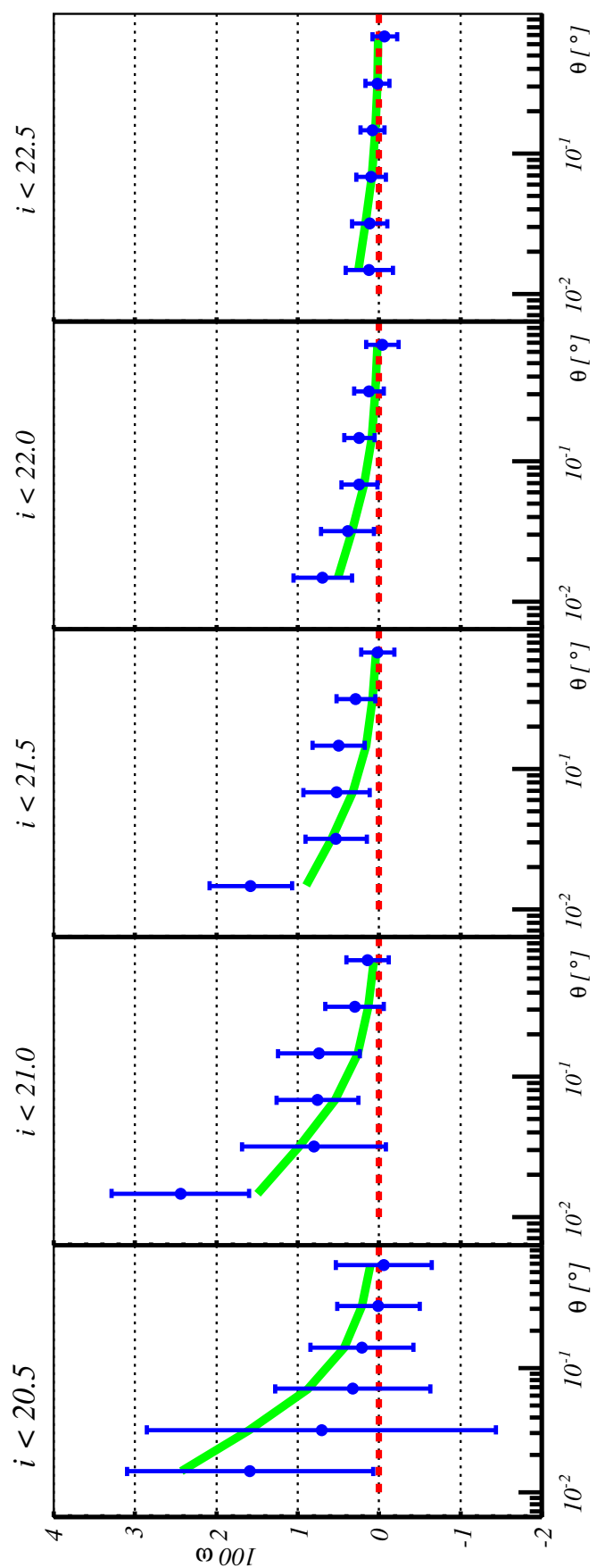


Figure 4.5: CONA

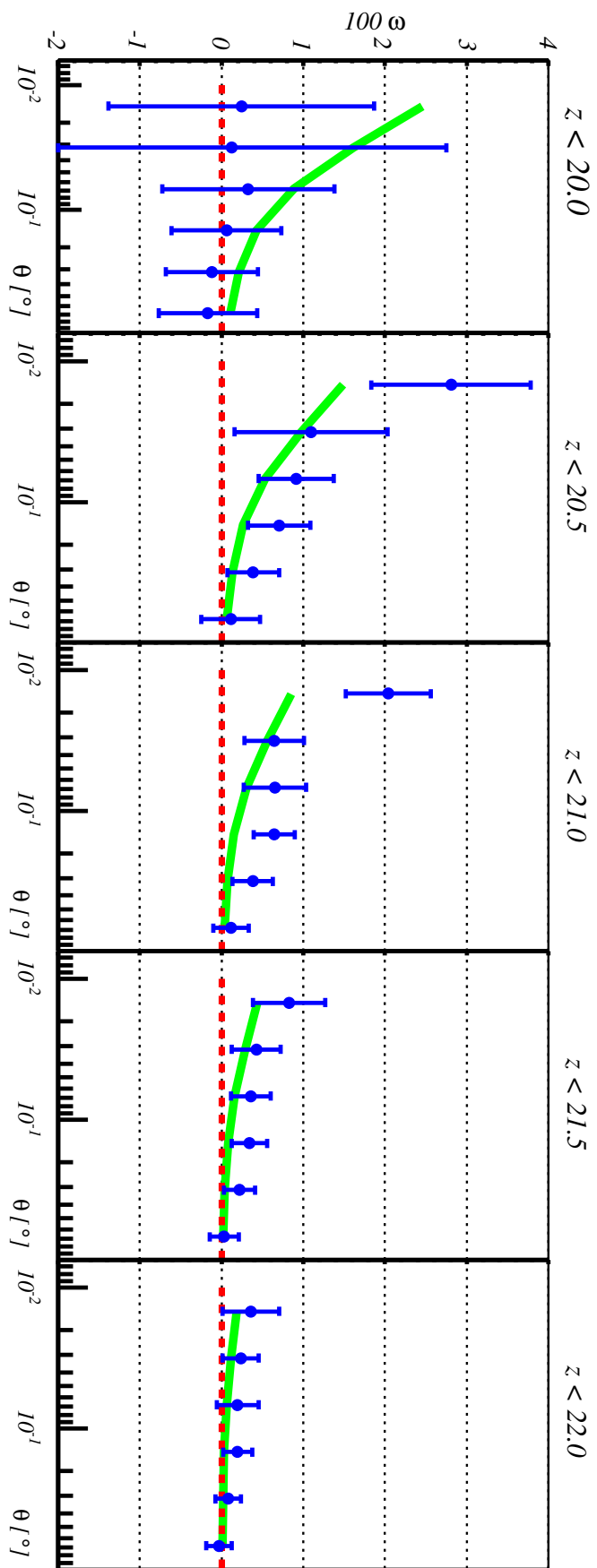


Figure 4.6: CONA

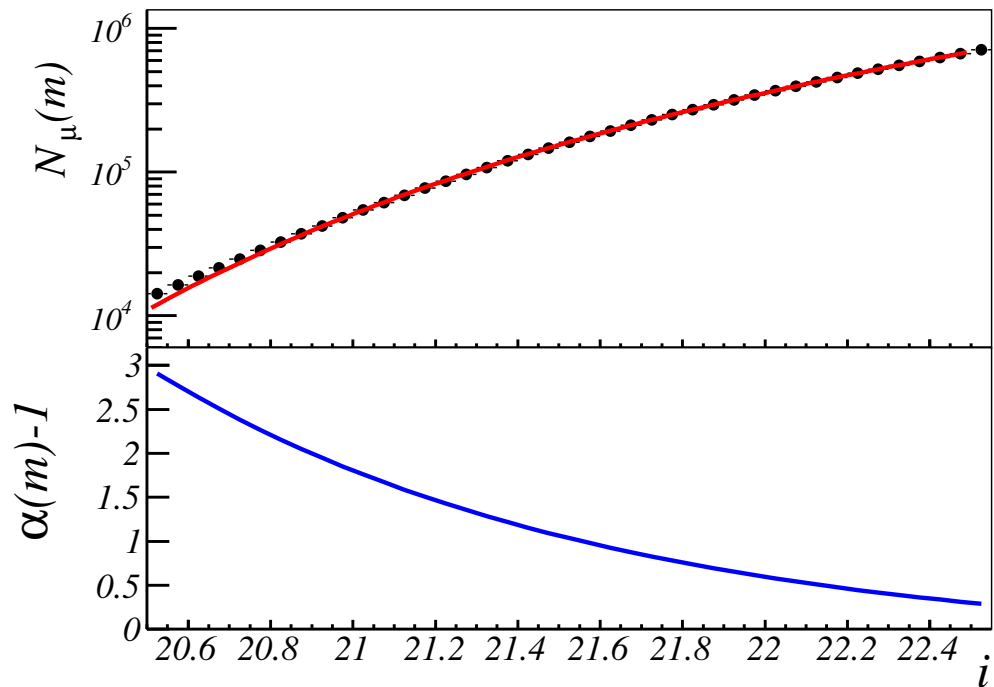


Figure 4.7: Top panel: Dots are the measured i -band cumulative number count as a function of the i -band magnitude. Red solid line is the fit using a Schechter function (see text). Bottom panel: number count slope $\alpha - 1$ measured from the fitted Schechter function of the top panel.

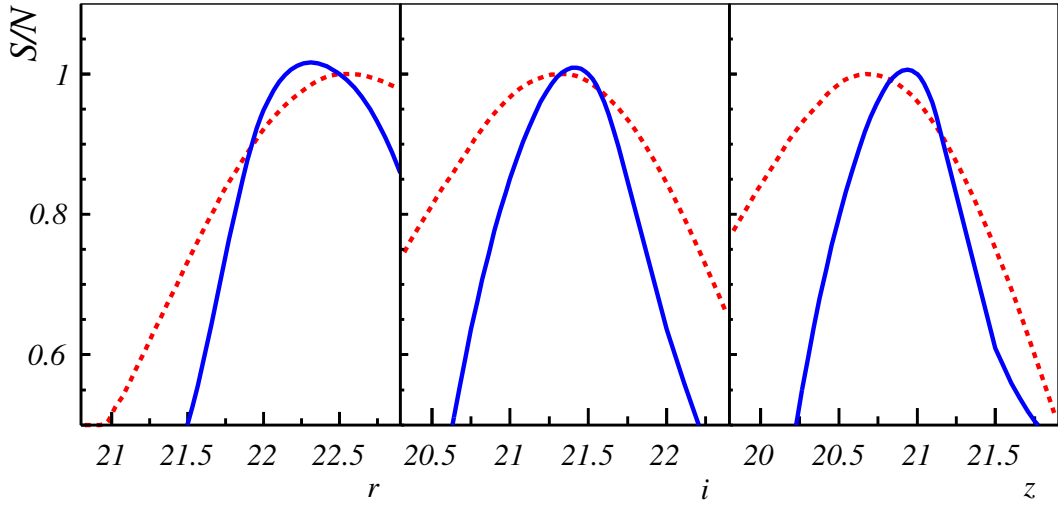


Figure 4.8: Red dashed line: expected signal-to-noise ratio computed with ???. Blue solid line is the measured significance of the data. Both curves are normalized to their respective maximum.

where $\tilde{\omega}, \omega$ are the measured and theoretical cross-correlation functions respectively. Goodness of fit tests are also made testing the hypothesis of absence of magnification:

$$\chi_{\text{zero}}^2 = \sum_{\eta\nu ij} \tilde{\omega}_{\text{LS}_i}(\theta_\eta) C^{-1}(\omega_{\text{LS}_i}(\theta_\eta); \omega_{\text{LS}_j}(\theta_\nu)) \tilde{\omega}_{\text{LS}_j}(\theta_\nu). \quad (4.6)$$

The χ^2 values can be seen in Table 4.1 showing good agreement with the theoretical predictions described in ???. To test which hypothesis is favored, the Bayes factor is used:

$$\mathcal{B} = \frac{P(M|\Theta)}{P(Z|\Theta)} = \frac{P(\Theta|M)}{P(\Theta|Z)} \frac{P(M)}{P(Z)}, \quad (4.7)$$

where

$$P(M|\Theta) = e^{-\chi_{\text{Planck}}^2/2} \quad (4.8)$$

and

$$P(Z|\Theta) = e^{-\chi_{\text{zero}}^2/2}. \quad (4.9)$$

The assumed prior sets detection and non-detection of magnification to be equally probable: $P(M) = P(Z)$. Bayes factors are computed for each function individually as well as for each band using the full covariance.

The significance for each individual correlation function has a strong dependence on the considered magnitude limit of the sub-sample. At the bright cuts, shot-noise prevents the identification of a non-zero magnification signal. At the faint end, although the sub-samples are much more populated, the strength of the magnification signal is compatible with zero. This behaviour has been compared with the predictions (see ??). Predicted and measured values are plotted together

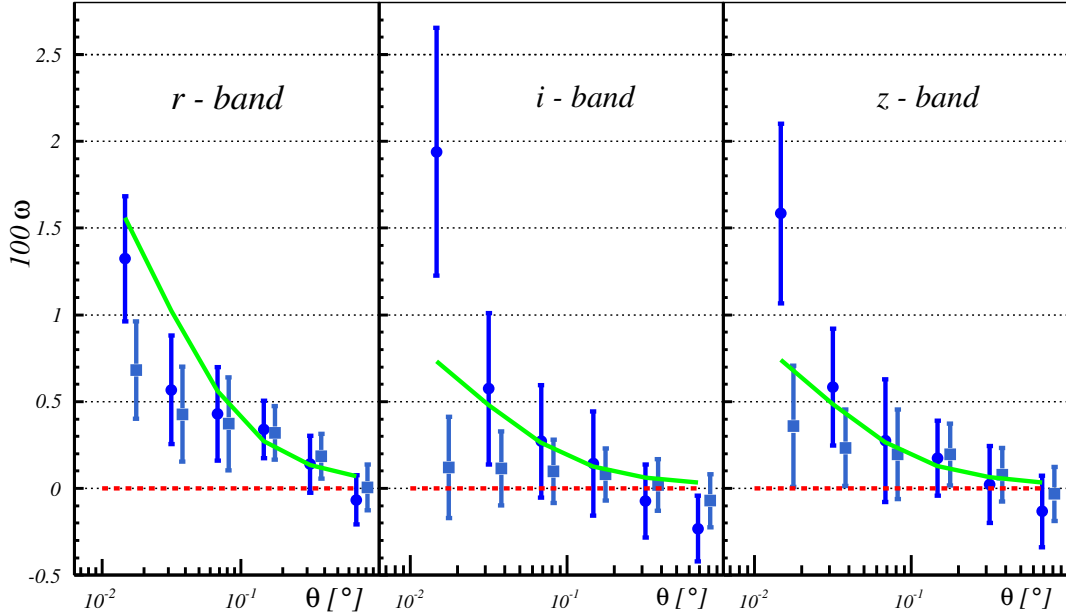


Figure 4.9: Measured two-point angular cross-correlation functions for the samples $r < 23.0$, $i < 22.5$ and $z < 22.0$ left to right respectively. Dots use the optimal weighting [107], where each galaxy is weighted by its corresponding $\alpha_S(m) - 1$ value, whereas squares are not weighted. Green line is the theoretical prediction. Red dashed line is an eye-guide for zero.

in Figure 4.8. It can be seen that the prediction of the location of the maximum signal-to-noise can only be used as a first approach.

To compute the significance of the detection for each band, the full covariance is used. One covariance matrix (see Figure 4.3 for the i -band matrix) per each band is computed taking into account the correlations between each magnitude cut. The logarithm of the Bayes factor can be found in Table 4.1, being all above 2, allowing to claim that magnification has been detected [**10.2307/2291091**].

A usual approach to enhance the signal-to-noise ratio, is to define a unique source sample and weight each source galaxy with its corresponding $\alpha_S(m) - 1$ value [129] and compute the two-point angular cross-correlation function. This weighting procedure is used at the samples $r < 23.0$, $i < 22.5$ and $z < 22.0$. These correlation functions can be seen in Figure 4.9 with a comparison with the theoretical prediction and the correlation functions of the same sample computed without weighting. Significances of these measurement can be found in Table 4.1 with a marginal difference respect to the one computed without weighting using the five subsamples.

Finally, in order to test that the signal is achromatic, the measured two-point

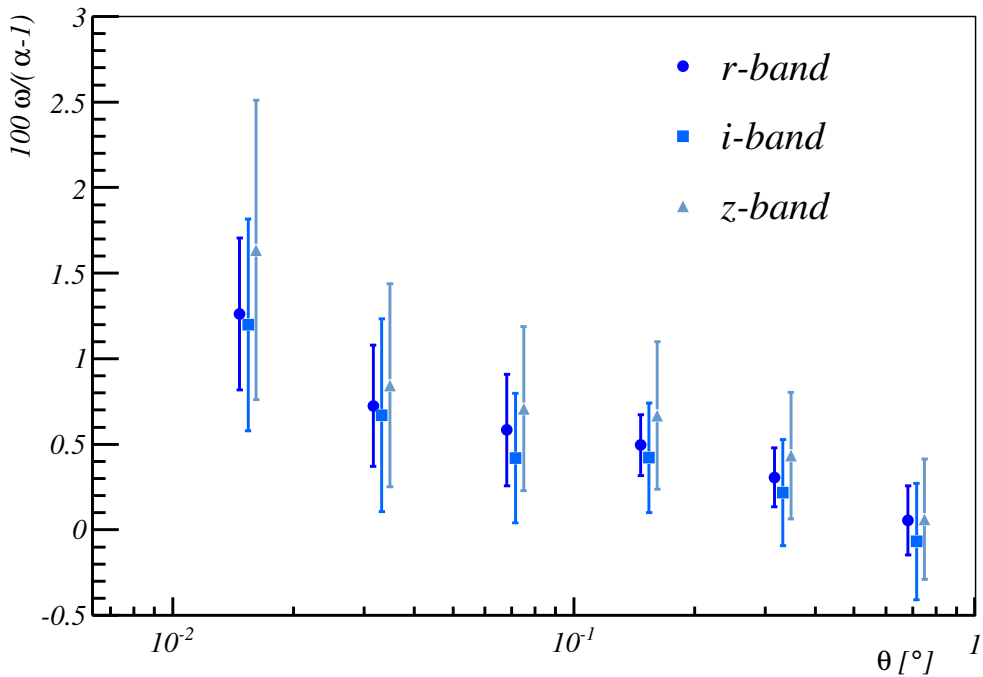


Figure 4.10: Example of the achromaticity of the measured signal. Here are shown the measured two-point angular cross-correlation functions for $r < 22.5$, $i < 22.0$ and $z < 21.5$ divided by their corresponding $\alpha - 1$.

angular cross-correlation functions for each band, normalized by its $\alpha_S(m) - 1$ are compared. All cross-correlation functions fluctuate within 1σ errors (see Figure 4.10 for an example) demonstrating that the measured convergence field does not depend on the considered band.

4.2.3 Systematic error analysis

Here, the impact of potential sources of systematic errors on the measured two-point angular cross-correlation function is investigated and how they are taken into account in the measurement is described.

Number count slope α

When comparing the measured two point angular cross-correlation functions with the theoretical prediction via ?? for a given set of cosmological parameters, $\alpha(m)$ is determined by fitting the cumulative number count distribution to Equation 4.3 and then using ???. To compute the possible impact of the uncertainty of this fit on the comparison with theory, a marginalisation over all the parameters of fit (A, m_*, β) is made.

Parameters are randomly sampled with a Gaussian distribution centred on the value given by the fit to the cumulative number count and with a standard deviation equal to the 1σ errors of the fit. The value of α is recalculated with these randomly sampled parameters. The impact of the dispersion of the α values obtained is negligible compared to the size of the jackknife errors, so they are not

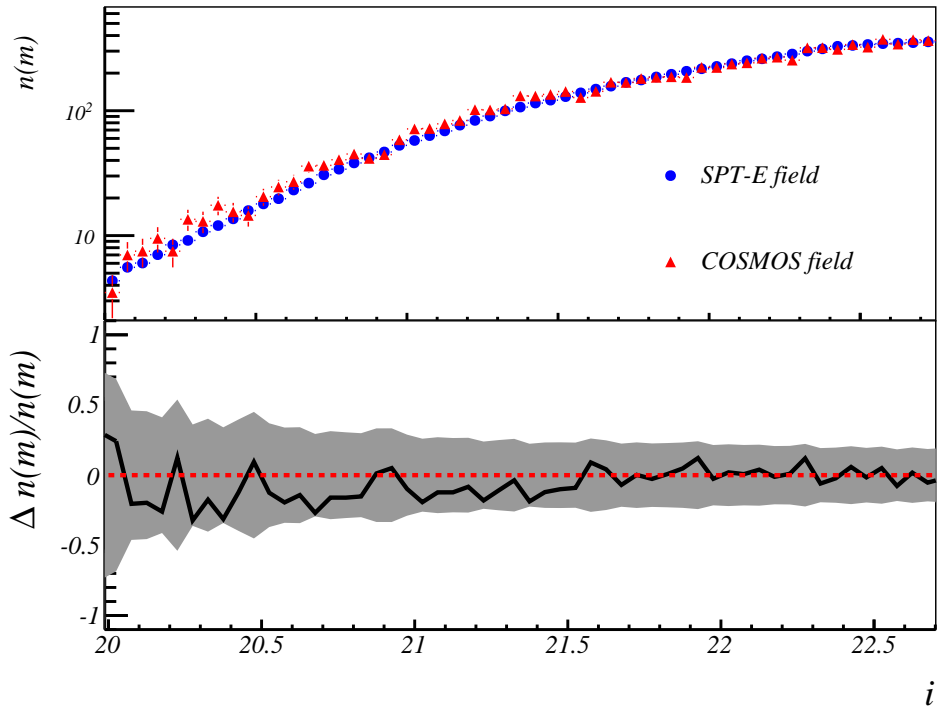


Figure 4.11: Upper panel: Comparison of the magnitude distribution for the SPT-E and the COSMOS fields. Both histograms are normalized by their respective area. Lower panel: Relative difference between the magnitude distribution of the COSMOS and the SPT-E fields. The shaded region shows the 1σ confidence interval computed from shot-noise.

taken into account.

In addition to the parameter determination, a possible non-completeness on the SPT-E field can modify the magnitude distribution altering the cumulative number count slope parameter [130]. To estimate the possible impact of non-completeness, the measured magnitude distributions of the SPT-E field are compared with those of deeper fields measured by DES, such as the COSMOS field. Both distributions are found to be equal at the range of magnitudes considered on this analysis (see Figure 4.11 for an example in the i -band).

Object obscuration

[113] studied whether moderately bright objects in crowded environments produce a decrease in the detection probability of nearby fainter objects at scales $\theta \lesssim 10$ arcsec. However, such scales are well below those considered in this analysis ($\theta > 36$ arcsec) and therefore this effect is ignored.

Stellar contamination

For a given choice of star-galaxy classifier, there will be a number of stars misclassified as galaxies, so the observed two-point angular cross-correlation function $\omega_O(\theta)$ must be corrected by the presence of any fake signal induced by stars (see ??):

$$\omega_{LS_j} = \frac{\omega_O(\theta) - \lambda_L \omega_{*S_j}(\theta) - \lambda_{S_j} \omega_{L*}(\theta)}{1 - \lambda_L - \lambda_{S_j}}, \quad (4.10)$$

where ω_{LS_j} is the corrected galaxy cross-correlation function, ω_{L*} is the cross-correlation function of the true galaxy lenses with the stars misclassified as galaxies in the source sample, ω_{*S_j} is the cross correlation of the stars misclassified as galaxies in the lenses with the true source galaxies and λ_L, λ_{S_j} are the fraction of stars in the lens and in the source samples respectively. Assuming that the misclassification of stars is spatially random and is a representative sample of the spatial distribution of the population classified as stars and that the fraction of misclassified stars is small, the functions $\omega_{L*}, \omega_{*S_j}$ are estimated from the cross-correlation of the galaxy population and the stellar population in the corresponding redshift bin.

Following a similar approach to [131], if the latter is true and the misclassified stars trace the global population of stars, for a given patch of the sky the number of objects classified as galaxies N_O must be the average number of true galaxies \bar{N}_g plus a quantity proportional to the number of stars on that given pixel,

$$N_O = \bar{N}_g + \gamma N_s. \quad (4.11)$$

Dividing by the average number of objects marked as galaxies \bar{N}_O ,

$$\frac{N_O}{\bar{N}_O} = p + \gamma N_s, \quad (4.12)$$

where $p = \bar{N}_g/\bar{N}_O$ is the purity of the sample, that is, $\lambda = 1 - p$.

In order to estimate the purity of the galaxy sample with this method, an $N_{\text{side}} = 512$ HEALPix pixelation is made and for each pixel N_O/\bar{N}_O and N_s is computed. Then, a fit to Equation 4.12 is made determining a purity of 94 per

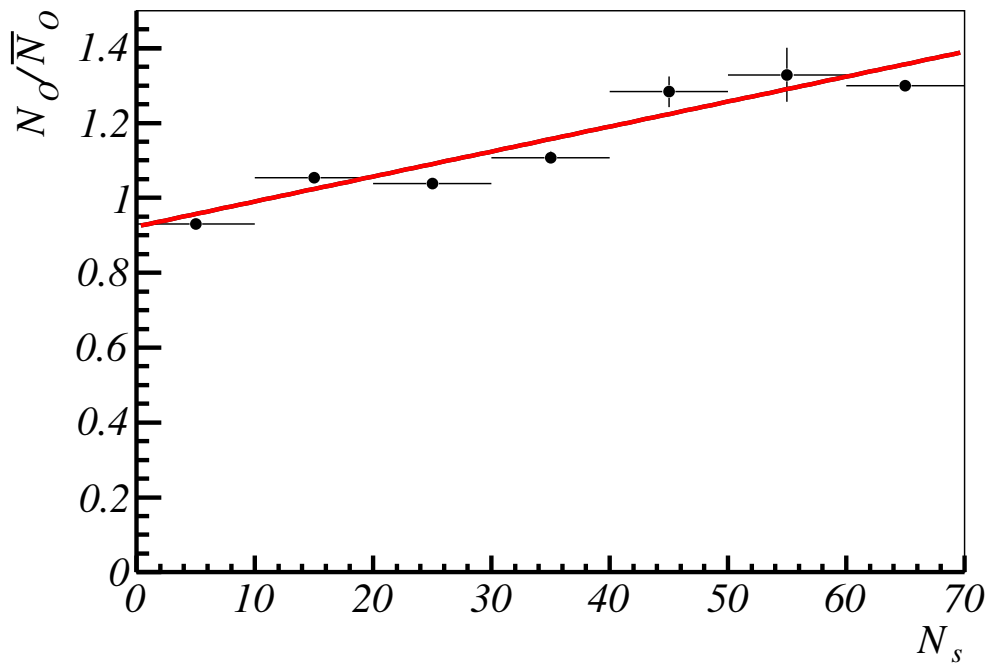


Figure 4.12: Determination of the purity of the lens sample. For each $N_{\text{nside}} = 512$ HEALPix-pixel, the number of objects classified as galaxies divided by the average number of galaxies per pixel is plotted as a function of the number of objects classified as stars. Black dots are the measured data. Red line is the linear fit to the data. The intercept of the line with the Y-axis is the estimated purity of the sample.

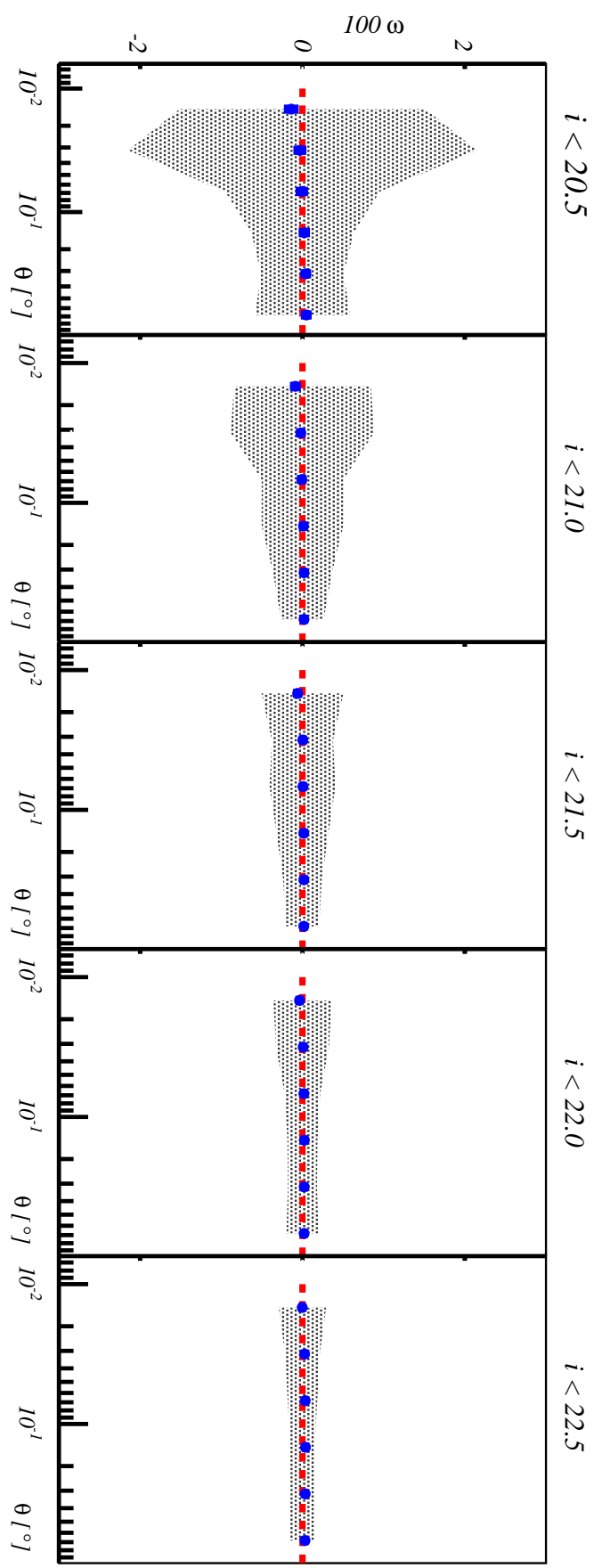


Figure 4.13: Correction by stellar contamination on the $i < 21.5$ sample. Blue dots are the correction and shaded area is the 1σ confidence interval of the measured cross-correlations of the magnification signal. Red dashed line is and eye-guide for zero.

cent for the lens sample and about 98 per cent for the source sample depending on the considered band (see Figure 4.12 for an example). With this purity, the correction due to stellar contamination given by Equation 4.10 is found to be one order of magnitude smaller than the statistical errors (see Figure 4.13 for the *i*-band correction), so stellar contamination is not taken into account in the analysis. Nevertheless, on future analysis with more galaxies and area this may be important. Note that the objects labeled as stars by our star-galaxy classifier would be a combination of stars and galaxies thus these calculations are an upper bound to stellar contamination.

Survey observing conditions

Observing conditions are not constant during the survey, leading to spatial dependencies across the DES-SV footprint [132] that may affect the observed cross-correlation function, such as seeing variations, air-mass, sky-brightness or exposure time [133]. To trace these spatial variations, the catalog produced by the Monte Carlo sampling code BALROG has been used as random sample [124]. It is important to remark that BALROG catalogs are produced with the same pipeline as DES-SV data, allowing one to trace subtle effects such as patchiness on the zero-points, deblending and possible magnitude errors due to a wrong sky subtraction close to bright objects.

The use of Monte Carlo sampling methods provides a new approach to mitigate systematic effects complementary to methods that cross-correlate the galaxy-positions with the maps of the survey observing conditions ([131]; [134]; [133]) or involve masking the regions of the sky with worst values of the observing conditions [112]. The amount of sky to be masked in order to mitigate the systematic effects on the correlation functions, is freely decided based on the impact on the correlation function, which may lead to a biassed measurement. On the other hand, the approach involving cross-correlations may lead to an overcorrection effect since the different maps of the observing conditions are, in general, correlated in a complicated manner [2016MNRAS.456.2095E]. This new Monte Carlo technique to sample the selection function of the survey given by BALROG, has the advantage that takes into account the correlation of the different observing conditions maps as well as provides an objective criteria to mitigate systematic errors on the correlation function for a given sample, avoiding biassed measurements. In addition, the use of BALROG has the potential to allow us in the future to exploit the full depth of the survey [124].

Dust extinction

The possible presence of dust in the lenses may modify the observed magnitude in addition to the magnitude shift due to magnification [109]. The change in magnitude (δm) on the *p*-band may be written as

$$\delta m_p = -2.5 \log \mu + \frac{2.5}{\ln 10} \tau_p, \quad (4.13)$$

where $\mu \simeq 1 + 2\kappa$ is the change in magnitude due to magnification and τ_k is the optical depth due to dust extinction. Whereas magnification is achromatic, dust extinction induces a band-dependent magnitude change. Taking this into account,

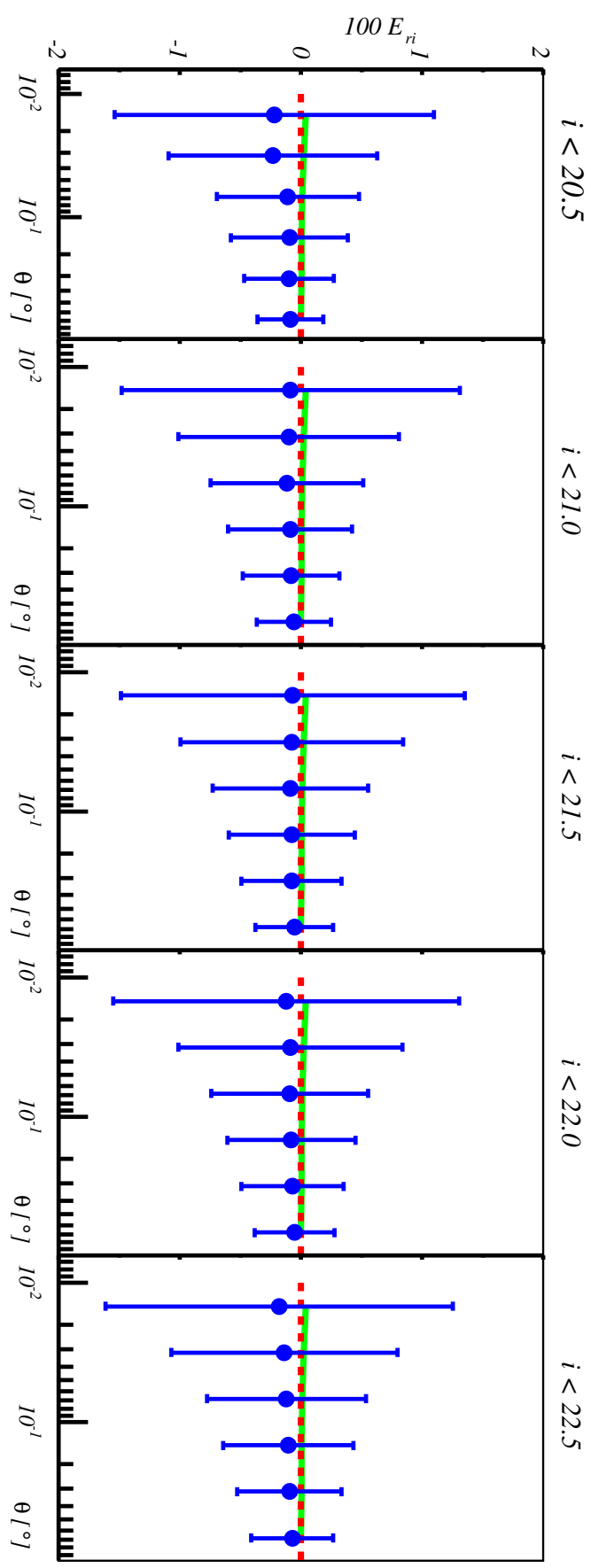


Figure 4.14: Blue dots: colour-density cross-correlation functions measured on SV data for the r and i bands (sample $i < 21.5$). Green solid line is the expected value from Equation 4.16. Red dashed line is an eye-guide for zero.

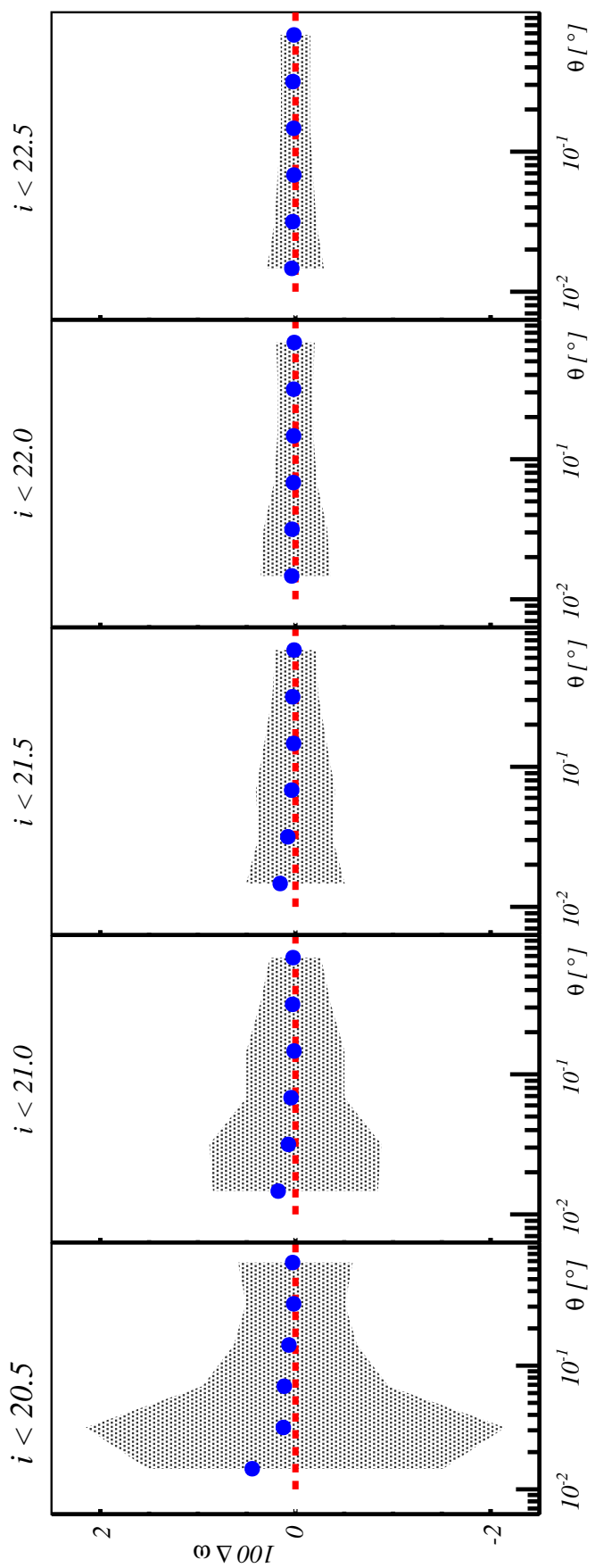


Figure 4.15: Impact of dust on the number count from MIKE (case $i < 21.5$). Shade is the 1σ confidence interval. Blue dots are the number count differences between the case with and the case without the simulated dust profile. Red dashed line is an eye-guide for zero.

Figure 4.16: Comparison of 1σ jackknife errors of the measured correlation function (grey shade) with the expected signal induced by the photo-z migration between the lens and the source sample (case $i < 22.5$) computed theoretically with the stacking of the pdfs for the i -band (blue line).

the colour-excess for bands p, q ⁷ is defined as

$$E_{pq} = \delta m_p - \delta m_q = 1.08[\tau_p - \tau_q]. \quad (4.14)$$

Define the colour-density cross-correlation as [109]

$$\langle \delta_g E_{pq} \rangle(\theta) = 1.09[\tau_p(\theta) - \tau_q(\theta)], \quad (4.15)$$

where δ_g is the density contrast of the lenses and E_{pq} is the colour-excess of the sources; from the measurements by [109] it can be parametrized as

$$\langle \delta_g E_{pq} \rangle(\theta) = 1.09\tau_V \left[\frac{\lambda_V}{\lambda_p} - \frac{\lambda_V}{\lambda_q} \right] \left(\frac{\theta}{1'} \right)^{-0.8}, \quad (4.16)$$

with $\tau_V = 2.3 \times 10^{-3}$ the optical depth at the V -band and $\lambda_V, \lambda_p, \lambda_q$ the average wavelengths of the V , p and q bands respectively. With this parametrization, the impact of dust extinction is negligible at the scales considered on this analysis. As it can be seen in Figure 4.14, colour-density cross-correlation functions are compatible with Equation 4.16 as well as with zero.

In addition, the impact of a dust profile has been simulated as described in Equation 4.16 with the MICE simulation (??). To do so, for each galaxy belonging to the source sample a magnitude shift is induced

$$m_d = m_\mu + 1.09\tau_V \frac{\lambda_V}{\lambda} \sum_l \left(\frac{\theta_l}{1'} \right)^{-0.8}. \quad (4.17)$$

Here θ_l is the angular separation of the source-galaxy and the l -th lens galaxy and the summation is over all the galaxies of the lens sample. In Figure 4.15 the difference between the two-point angular cross-correlation with and without the dust can be seen to be less than the statistical errors. It can be deduced that dust has no impact on the angular scales considered on this work.

Since the parametrization used here only applies to a sample similar to the one used at [109], statements about dust constrains are limited. Nevertheless this does not change the fact that no chromatic effects are detected.

Photometric redshifts

A general study of photo-z performance in DES-SV can be found in [121]. A comprehensive study of the photo-z performance and its implications for weak lensing for this data can be found in [135]. Both studies are followed in this analysis. Conservative photo-z cuts are made in order to minimize migration

⁷In this section p, q stand for a generic index label while V stands for the V band of the UBV system.

between lens and source samples. Nevertheless, catastrophic outliers in the photo-z determination can bias the measurement of κ [136]. Thus, the tails of the probability density functions (pdfs) of the photo-z code are a crucial systematic to test. As mentioned in ??, in addition to the magnification signal, galaxy migration due to a wrong photo-z assignment between lens and source samples may induce a non-zero cross-correlation signal due to the physical signal coming from the clustering of objects in the same redshift bin. As a first approach, estimation of the expected signal induced by photo-z migration (ω^{ph}) is computed with ??:

$$\omega_{LS_j}^{ph}(\theta) = \int_0^\infty dz \int_0^\infty dz' \phi_L(z) \phi_{S_j}(z') \xi(\theta; z, z'), \quad (4.18)$$

where $\xi(\theta; z, z')$ is the 3D correlation-function and ϕ_L, ϕ_{S_j} are the redshift distribution of the lens (L) sample and the source sample (S_j) estimated from the stacking of the pdfs given by TPZ. Figure 4.16 compares the measured two-point angular cross-correlation and the expected signal induced by photo-z can be seen for the I sample. The signal induced by photo-z is found to be smaller than the statistical errors. Note that this method relies on an assumed cosmology and bias model, and therefore should be considered only an approximation. A more accurate calculation can be made with the help of N-body simulations.

From the overlap of the redshift distribution of both lens and source samples, it is found that the total photo-z migration between lens and source sample is $o \sim 0.6\%$ depending on the magnitude cut of the source sample. The procedure to compute this overlap is to integrate the product of the pdfs of the lens and source sample:

$$o = \int_0^\infty dz \phi_L(z) \phi_S(z), \quad (4.19)$$

where ϕ_L, ϕ_S are the stacked pdfs of the lens and source sample respectively. Since TPZ provides an individual pdf for each galaxy, the stacked pdf of a given sample is computed by adding all the individual pdfs of the galaxies that belong to that sample (see [2016MNRAS.459.1293A] for a study of clustering with stacked pdfs).

To estimate the maximum photo-z migration allowed between the lens and the source sample, the MICE simulation (??) with the un-lensed coordinates and magnitudes is used. Galaxies are randomly sampled on the lens redshift bin and then placed on the source redshift bin. Conversely, galaxies on the source redshift bin are randomly sampled and placed on the lens redshift bin. For a given lens or source sample, the number of galaxies introduced from the other redshift bin is chosen to be 0.1, 0.3, 0.5, 0.7, 0.9 and 2 per cent of the galaxies. Then, the two-point angular cross-correlation is computed for each case. The difference of the correlation functions measured at the simulation with induced migration between lens and source sample and the original used in ?? is the signal induced by photo-z migration. The signal induced by photo-z for the cases with 0.9 and 2 per cent computed with this method can be seen at Figure 4.17. It is found that at 0.9 per cent of contamination, the induced signal due to photo-z migration is comparable to the error in the correlation functions. This upper limit is greater than the

estimated photo-z migration, demonstrating that the effect of photo-z migration is negligible. Photo-z migration has a larger impact on the brightest samples. Nevertheless, since the errors of the correlation functions of these samples are shot-noise dominated, the tightest constraints on photo-z migration are imposed by the faintest samples. With a larger data sample this statement will no longer be true.

Photo-z induced correlation functions that mimic magnification may affect the measured significance. Thus, Bayes factor is recomputed with two new hypothesis, the measured signal is a combination of magnification and photo-z ($M + Ph$) or the measured signal is only photo-z (Ph):

$$\mathcal{B} = \frac{P(M + Ph|\Theta)}{P(Ph|\Theta)} = \frac{P(\Theta|M + Ph)}{P(\Theta|Ph)}, \quad (4.20)$$

where

$$P(\Theta|M + Ph) = e^{-\chi^2_{\text{Planck+Ph}}/2} \quad (4.21)$$

and

$$P(\Theta|Ph) = e^{-\chi^2_{\text{Ph}}/2}. \quad (4.22)$$

To compute $\chi^2_{\text{Planck+Ph}}$ and χ^2_{Ph} it has been assumed that the expected theory is given by $\omega_{LS_j}(\theta) + \omega_{LS_j}^{\text{Ph}}(\theta)$ and $\omega_{LS_j}^{\text{Ph}}$ respectively, where $\omega_{LS_j}^{\text{Ph}}$ is the expected signal induced by photo-z computed using Equation 4.18. The significances recomputed using these two new hypothesis for the r , i and z bands are $\log_{10} \mathcal{B} = 2.5, 4.0, 3.5$ respectively. Thus, it can be concluded that photo-z migration has a limited impact on the measured significances.

All previous calculations were based on the assumption that the pdfs are a reliable description of the true redshift distribution. This statement can be partially validated comparing the pdfs with the spectroscopic redshift distribution for the same sample (see Figure 4.18 for an example). Redshift distributions predicted by TPZ are found to be representative of those given by the spectroscopic sample. Nevertheless, this statement has limitations –but is good enough for SV data– and a more accurate description of the real redshift distribution of the full sample will be measured with methodologies involving clustering-based estimators ([137]; [138]; [139]; [140]) when the size of the data sample grows. This type of estimators involve the use of two-point angular cross-correlations between different redshift bins, whose measurement may be biased by number count magnification itself. Nevertheless, as it has been stated in ??, depending on the value of the number count slope, the amplitude induced by magnification on the correlation-function may be zero. Thus, when employing this kind of estimators, samples should be carefully chosen so that $\alpha_S - 1 = 0$. This can be done by measuring the number count slope at the cumulative magnitude distribution with methods such that used in this work.

Finally, to demonstrate that the measured signal is independent of the photo-z technique employed to estimate the redshift, the two-point angular cross-correlation functions used on this analysis are re-computed with redshift estimated with other two different approaches that have shown to have similar performance as TPZ [121] a neural network, Skynet [141], and a template based approach, Bayesian

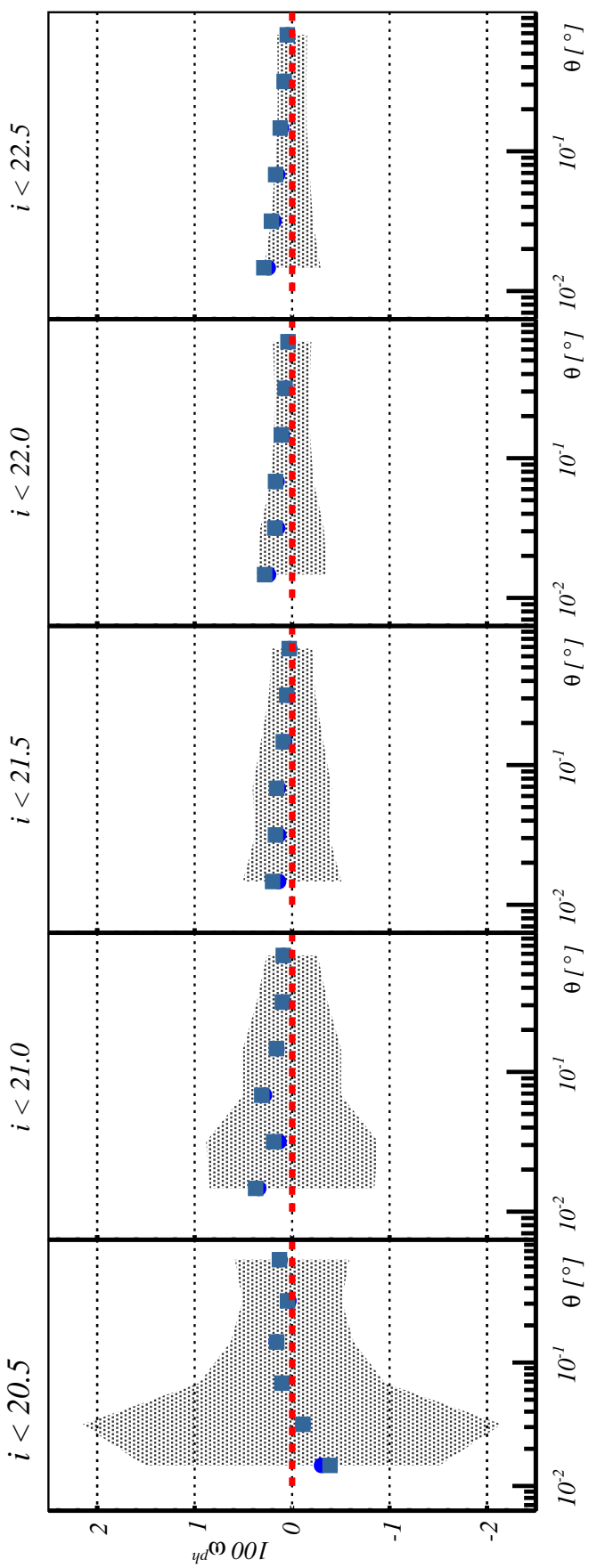


Figure 4.17: Estimation of the signal induced by migration of selected fractions of MICE unlensed galaxies between the lens and the source sample (case $i < 22.5$). Shaded area is the 1σ confidence interval for the measured number count cross-correlations. Dark blue dots correspond to a contamination fraction of 0.9 per cent. Violet squares correspond to a 2 per cent. Squares are displaced at the X axis for clarity. Red dashed line is an eye-guide for zero.

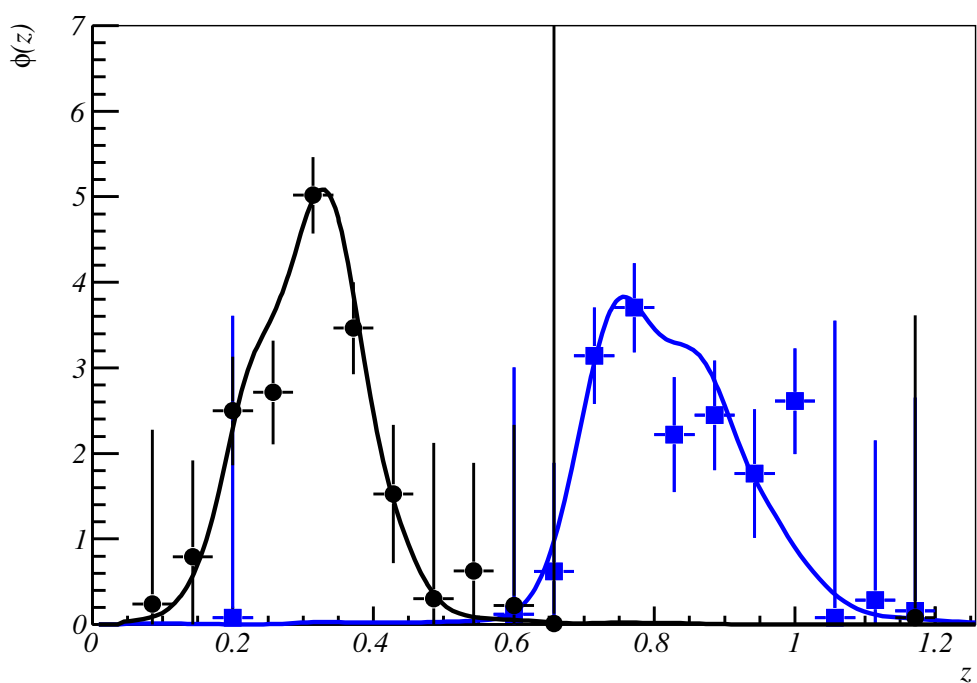


Figure 4.18: Comparison of the redshift distribution computed by the stacking of the pdfs given by TPZ (solid lines) with the ones computed with the spectroscopic sample of the lens (black dots) and the source sample $i < 22.5$ (blue squares).

Photo-Z (BPZ; [142]). Figure 4.19 compares the cross-correlations computed with the three codes for the *i*-band, showing them to be within 1σ errors.

4.3 Magnification in DES Year 1 data

4.3.1 Data sample

Lens sample

Lens sample

4.3.2 Determination of matter profile: voids & troughs

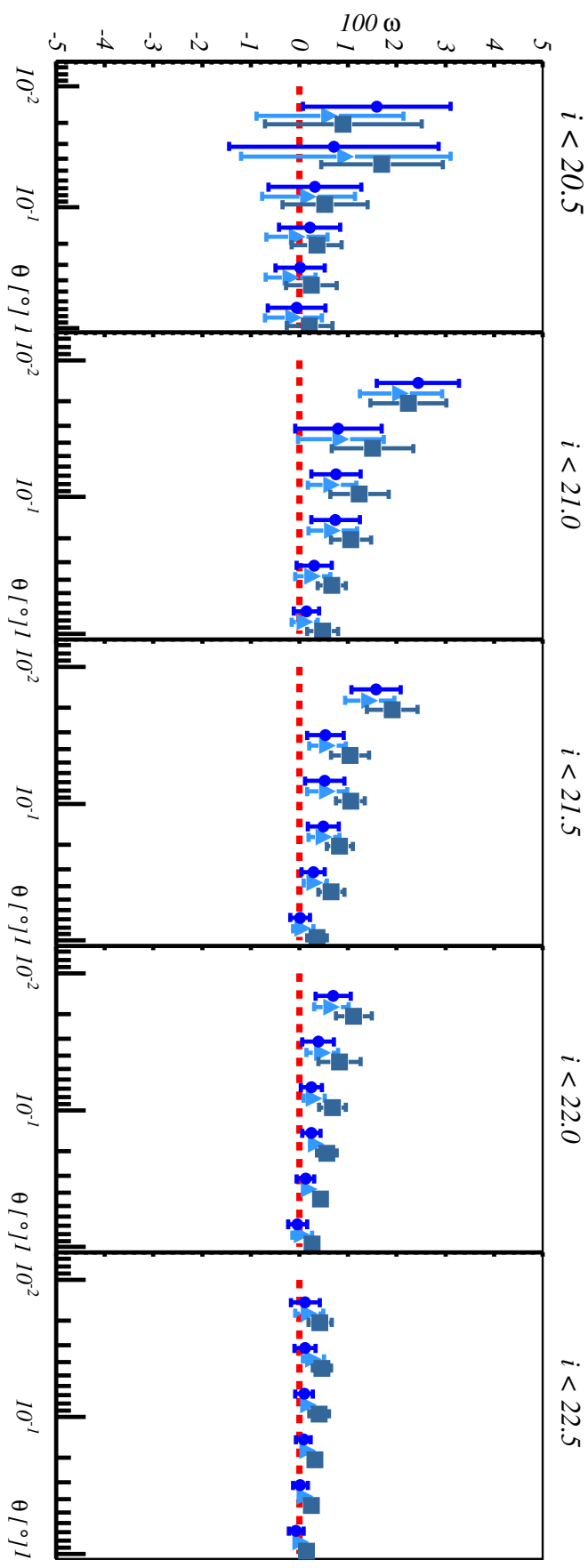


Figure 4.19: Comparison of the measured two-point angular cross-correlation functions corresponding to the sample $i < 21.5$ measured with the Landy-Szalay estimator using TPZ, Skynet and BPZ. Triangles and squares are displaced at the horizontal axis for clarity.



5. Conclusions

General Relativity has been the gravitational theory since Einstein conceived it a century ago. Since then, it passed successfully the most stringent tests. Nevertheless, the discovery of the accelerated expansion of the Universe –dark energy– along with the latest LHC results on High Energy Physics suggest that there must be something beyond General Relativity or the Standard Model of Particle Physics.

Tests of gravity on cosmological scales can provide an insight on the nature of dark energy. One of those scenarios, are the empties regions of the Universe: voids and troughs. Since they are mostly empty of matter, their evolution and structure is dominated by dark energy. Thus, they constitute a promising environment to test the nature of dark energy.

Measurements of voids and troughs properties can be made with weak gravitational lensing, namely: magnification and gg-lensing. The advantage of using these two methods is that they are complementary effects of the same physical phenomena but are sensitive to different systematic effects. Thus, the combination of these two weak-lensing methods to measure voids and trough profiles provide an accurate and reliable probe for the nature of dark energy.

Although wide-field surveys has provided the last years numerous weak-lensing results, magnification has been little studied due to its low signal-to-noise ratio compared with gg-lensing and to its sensitivity to systematic effects.

On this work, a technique to measure magnification with the number-count technique has been presented. In addition, a through and new way to take into account systematic errors has been presented, providing un-biased and reliable measurement.

Nevertheless, number-count magnification is not the measurement *per se*, but

a proxy to the convergence profile of the lenses, the final physical observable. This implies that other types of magnification measurements can be made as a proxy to the convergence: the magnitude and size shift.



A. My test appendix



References

- [1] F. Halzen and A.D. Martin. *Quarks and leptons: an introductory course in modern particle physics*. Wiley, 1984. URL: <https://books.google.es/books?id=zwDvAAAAMAAJ>.
- [2] M.E. Peskin and D.V. Schroeder. *An Introduction to Quantum Field Theory*. Advanced book classics. Avalon Publishing, 1995. ISBN: 9780201503975. URL: <https://books.google.es/books?id=i35LALNOGosC>.
- [3] S. Weinberg. *The Quantum Theory of Fields*. The Quantum Theory of Fields 3 Volume Hardback Set v. 1. Cambridge University Press, 1995. ISBN: 9780521550017. URL: <https://books.google.es/books?id=doeDB3%5CWLvwC>.
- [4] S. Weinberg. *The Quantum Theory of Fields: Volume 2, Modern Applications*. Cambridge University Press, 1996. ISBN: 9781139643252. URL: <https://books.google.es/books?id=J2EhAwAAQBAJ>.
- [5] S. F. Novaes. “Standard Model: An Introduction”. In: *ArXiv High Energy Physics - Phenomenology e-prints* (Jan. 2000). eprint: [hep-ph/0001283](https://arxiv.org/abs/hep-ph/0001283).
- [6] Steven Weinberg. “Photons and Gravitons in Perturbation Theory: Derivation of Maxwell’s and Einstein’s Equations”. In: *Phys. Rev.* 138 (4B May 1965), B988–B1002. DOI: [10.1103/PhysRev.138.B988](https://doi.org/10.1103/PhysRev.138.B988). URL: <https://link.aps.org/doi/10.1103/PhysRev.138.B988>.
- [7] R.P. Feynman et al. *Feynman Lectures on Gravitation*. Advanced book program. Addison-Wesley, 1995. ISBN: 9780201627343. URL: <https://books.google.es/books?id=P8XvAAAAMAAJ>.
- [8] P. G. O. Freund, A. Maheshwari, and E. Schonberg. “Finite-Range Gravitation”. In: *ApJ* 157 (Aug. 1969), p. 857. DOI: [10.1086/150118](https://doi.org/10.1086/150118).
- [9] Robert M. Wald. “Spin-two fields and general covariance”. In: *Phys. Rev. D* 33 (12 June 1986), pp. 3613–3625. DOI: [10.1103/PhysRevD.33.3613](https://doi.org/10.1103/PhysRevD.33.3613). URL: <https://link.aps.org/doi/10.1103/PhysRevD.33.3613>.

- [10] C Cutler and R M Wald. “A new type of gauge invariance for a collection of massless spin-2 fields. I. Existence and uniqueness”. In: *Classical and Quantum Gravity* 4.5 (1987), p. 1267. URL: <http://stacks.iop.org/0264-9381/4/i=5/a=024>.
- [11] R M Wald. “A new type of gauge invariance for a collection of massless spin-2 fields. II. Geometrical interpretation”. In: *Classical and Quantum Gravity* 4.5 (1987), p. 1279. URL: <http://stacks.iop.org/0264-9381/4/i=5/a=025>.
- [12] C. Patrignani et al. “Review of Particle Physics”. In: *Chin. Phys. C*40.10 (2016), p. 100001. DOI: [10.1088/1674-1137/40/10/100001](https://doi.org/10.1088/1674-1137/40/10/100001).
- [13] A. Einstein. “Die Grundlage der allgemeinen Relativitätstheorie”. In: *Annalen der Physik* 354.7 (1916), pp. 769–822. ISSN: 1521-3889. DOI: [10.1002/andp.19163540702](https://doi.org/10.1002/andp.19163540702). URL: <http://dx.doi.org/10.1002/andp.19163540702>.
- [14] A. Einstein. “Die Grundlage der allgemeinen Relativitätstheorie”. In: *Annalen der Physik* 354 (1916), pp. 769–822. DOI: [10.1002/andp.19163540702](https://doi.org/10.1002/andp.19163540702).
- [15] D. Alonso et al. “Measuring the transition to homogeneity with photometric redshift surveys”. In: *MNRAS* 440 (May 2014), pp. 10–23. DOI: [10.1093/mnras/stu255](https://doi.org/10.1093/mnras/stu255). arXiv: [1312.0861 \[astro-ph.CO\]](https://arxiv.org/abs/1312.0861).
- [16] D. Alonso et al. “Homogeneity and isotropy in the Two Micron All Sky Survey Photometric Redshift catalogue”. In: *MNRAS* 449 (May 2015), pp. 670–684. DOI: [10.1093/mnras/stv309](https://doi.org/10.1093/mnras/stv309). arXiv: [1412.5151](https://arxiv.org/abs/1412.5151).
- [17] G. Lemaître. “Un Univers homogène de masse constante et de rayon croissant rendant compte de la vitesse radiale des nébuleuses extra-galactiques”. In: *Annales de la Société Scientifique de Bruxelles* 47 (1927), pp. 49–59.
- [18] Planck Collaboration et al. “Planck 2015 results. XIII. Cosmological parameters”. In: *ArXiv e-prints* (Feb. 2015). arXiv: [1502.01589](https://arxiv.org/abs/1502.01589).
- [19] C. D. Leonard, P. Bull, and R. Allison. “Spatial curvature endgame: Reaching the limit of curvature determination”. In: *Phys. Rev. D* 94.2, 023502 (July 2016), p. 023502. DOI: [10.1103/PhysRevD.94.023502](https://doi.org/10.1103/PhysRevD.94.023502). arXiv: [1604.01410](https://arxiv.org/abs/1604.01410).
- [20] E. Hubble. “A Relation between Distance and Radial Velocity among Extra-Galactic Nebulae”. In: *Proceedings of the National Academy of Science* 15 (Mar. 1929), pp. 168–173. DOI: [10.1073/pnas.15.3.168](https://doi.org/10.1073/pnas.15.3.168).
- [21] J. A. Frieman, M. S. Turner, and D. Huterer. “Dark Energy and the Accelerating Universe”. In: *ARA&A* 46 (Sept. 2008), pp. 385–432. DOI: [10.1146/annurev.astro.46.060407.145243](https://doi.org/10.1146/annurev.astro.46.060407.145243). arXiv: [0803.0982](https://arxiv.org/abs/0803.0982).
- [22] J. E. Bautista et al. “Measurement of BAO correlations at $z = 2.3$ with SDSS DR12 \lya-Forests”. In: *ArXiv e-prints* (Feb. 2017). arXiv: [1702.00176](https://arxiv.org/abs/1702.00176).
- [23] J. T. Nielsen, A. Guffanti, and S. Sarkar. “Marginal evidence for cosmic acceleration from Type Ia supernovae”. In: *Scientific Reports* 6, 35596 (Oct. 2016), p. 35596. DOI: [10.1038/srep35596](https://doi.org/10.1038/srep35596). arXiv: [1506.01354](https://arxiv.org/abs/1506.01354).

- [24] A. Einstein. “Kosmologische Betrachtungen zur allgemeinen Relativitätstheorie”. In: *Sitzungsberichte der Königlich Preußischen Akademie der Wissenschaften (Berlin)*, Seite 142–152. (1917).
- [25] S. M. Carroll. “The Cosmological Constant”. In: *Living Reviews in Relativity* 4, 1 (Dec. 2001), p. 1. DOI: 10.12942/lrr-2001-1. eprint: astro-ph/0004075.
- [26] Steven Weinberg. “The cosmological constant problem”. In: *Rev. Mod. Phys.* 61 (1 Jan. 1989), pp. 1–23. DOI: 10.1103/RevModPhys.61.1. URL: <https://link.aps.org/doi/10.1103/RevModPhys.61.1>.
- [27] T. Padmanabhan. “Cosmological constant—the weight of the vacuum”. In: *Phys. Rep.* 380 (July 2003), pp. 235–320. DOI: 10.1016/S0370-1573(03)00120-0. eprint: hep-th/0212290.
- [28] P. Bechtle, T. Plehn, and C. Sander. “The Status of Supersymmetry after the LHC Run 1”. In: *ArXiv e-prints* (June 2015). arXiv: 1506.03091 [hep-ex].
- [29] P. H. Brax and J. Martin. “Quintessence and supergravity”. In: *Physics Letters B* 468 (Nov. 1999), pp. 40–45. DOI: 10.1016/S0370-2693(99)01209-5. eprint: astro-ph/9905040.
- [30] P. Brax and J. Martin. “Cosmological Implications of the Supergravity Tracking Potential”. In: *ArXiv Astrophysics e-prints* (Nov. 1999). eprint: astro-ph/9912005.
- [31] P. Brax and J. Martin. “Robustness of quintessence”. In: *Phys. Rev. D* 61.10, 103502 (May 2000), p. 103502. DOI: 10.1103/PhysRevD.61.103502. eprint: astro-ph/9912046.
- [32] P. Binétruy. “Models of dynamical supersymmetry breaking and quintessence”. In: *Phys. Rev. D* 60.6, 063502 (Sept. 1999), p. 063502. DOI: 10.1103/PhysRevD.60.063502. eprint: hep-ph/9810553.
- [33] Joshua A. Frieman et al. “Cosmology with Ultralight Pseudo Nambu-Goldstone Bosons”. In: *Phys. Rev. Lett.* 75 (11 Sept. 1995), pp. 2077–2080. DOI: 10.1103/PhysRevLett.75.2077. URL: <https://link.aps.org/doi/10.1103/PhysRevLett.75.2077>.
- [34] J. A. Frieman and A. H. Jaffe. “Cosmological constraints on pseudo Nambu-Goldstone bosons”. In: *Phys. Rev. D* 45 (Apr. 1992), pp. 2674–2684. DOI: 10.1103/PhysRevD.45.2674.
- [35] L. Amendola and S. Tsujikawa. *Dark Energy: Theory and Observations*. 2010.
- [36] D. Burstein et al. “The distribution of mass in SC galaxies”. In: *ApJ* 253 (Feb. 1982), pp. 70–85. DOI: 10.1086/159611.
- [37] V. C. Rubin. “The rotation of spiral galaxies”. In: *Science* 220 (June 1983), pp. 1339–1344. DOI: 10.1126/science.220.4604.1339.

- [38] V. C. Rubin et al. “Rotation velocities of 16 SA galaxies and a comparison of Sa, Sb, and SC rotation properties”. In: *ApJ* 289 (Feb. 1985), pp. 81–98. DOI: [10.1086/162866](https://doi.org/10.1086/162866).
- [39] D. Burstein and V. C. Rubin. “The distribution of mass in spiral galaxies”. In: *ApJ* 297 (Oct. 1985), pp. 423–435. DOI: [10.1086/163541](https://doi.org/10.1086/163541).
- [40] M. Milgrom. “A modification of the Newtonian dynamics as a possible alternative to the hidden mass hypothesis”. In: *ApJ* 270 (July 1983), pp. 365–370. DOI: [10.1086/161130](https://doi.org/10.1086/161130).
- [41] J. Bekenstein and M. Milgrom. “Does the missing mass problem signal the breakdown of Newtonian gravity?” In: *ApJ* 286 (Nov. 1984), pp. 7–14. DOI: [10.1086/162570](https://doi.org/10.1086/162570).
- [42] R. H. Sanders. “A Stratified Framework for Scalar-Tensor Theories of Modified Dynamics”. In: *ApJ* 480 (May 1997), pp. 492–502. DOI: [10.1086/303980](https://doi.org/10.1086/303980). eprint: [astro-ph/9612099](https://arxiv.org/abs/astro-ph/9612099).
- [43] J. D. Bekenstein and R. H. Sanders. “Gravitational lenses and unconventional gravity theories”. In: *ApJ* 429 (July 1994), pp. 480–490. DOI: [10.1086/174337](https://doi.org/10.1086/174337). eprint: [astro-ph/9311062](https://arxiv.org/abs/astro-ph/9311062).
- [44] S. S. McGaugh. “Novel Test of Modified Newtonian Dynamics with Gas Rich Galaxies”. In: *Physical Review Letters* 106.12, 121303 (Mar. 2011), p. 121303. DOI: [10.1103/PhysRevLett.106.121303](https://doi.org/10.1103/PhysRevLett.106.121303). arXiv: [1102.3913 \[astro-ph.CO\]](https://arxiv.org/abs/1102.3913).
- [45] M. Milgrom. “Testing the MOND Paradigm of Modified Dynamics with Galaxy-Galaxy Gravitational Lensing”. In: *Physical Review Letters* 111.4, 041105 (July 2013), p. 041105. DOI: [10.1103/PhysRevLett.111.041105](https://doi.org/10.1103/PhysRevLett.111.041105). arXiv: [1305.3516 \[astro-ph.CO\]](https://arxiv.org/abs/1305.3516).
- [46] D. Clowe et al. “A Direct Empirical Proof of the Existence of Dark Matter”. In: *ApJ* 648 (Sept. 2006), pp. L109–L113. DOI: [10.1086/508162](https://doi.org/10.1086/508162). eprint: [astro-ph/0608407](https://arxiv.org/abs/astro-ph/0608407).
- [47] M. Bradač et al. “Strong and Weak Lensing United. III. Measuring the Mass Distribution of the Merging Galaxy Cluster 1ES 0657-558”. In: *ApJ* 652 (Dec. 2006), pp. 937–947. DOI: [10.1086/508601](https://doi.org/10.1086/508601). eprint: [astro-ph/0608408](https://arxiv.org/abs/astro-ph/0608408).
- [48] J. R. Brownstein and J. W. Moffat. “The Bullet Cluster 1E0657-558 evidence shows modified gravity in the absence of dark matter”. In: *MNRAS* 382 (Nov. 2007), pp. 29–47. DOI: [10.1111/j.1365-2966.2007.12275.x](https://doi.org/10.1111/j.1365-2966.2007.12275.x). eprint: [astro-ph/0702146](https://arxiv.org/abs/astro-ph/0702146).
- [49] E. P. Verlinde. “Emergent Gravity and the Dark Universe”. In: *ArXiv e-prints* (Nov. 2016). arXiv: [1611.02269 \[hep-th\]](https://arxiv.org/abs/1611.02269).
- [50] F. Lelli, S. S. McGaugh, and J. M. Schombert. “Testing Verlinde’s emergent gravity with the radial acceleration relation”. In: *MNRAS* 468 (June 2017), pp. L68–L71. DOI: [10.1093/mnrasl/slx031](https://doi.org/10.1093/mnrasl/slx031). arXiv: [1702.04355](https://arxiv.org/abs/1702.04355).

-
- [51] D.-C. Dai, R. Matsuo, and G. Starkman. “Gravitational lenses in generalized Einstein-aether theory: The bullet cluster”. In: *Phys. Rev. D* 78.10, 104004 (Nov. 2008), p. 104004. DOI: 10.1103/PhysRevD.78.104004. arXiv: 0806.4319 [gr-qc].
 - [52] A. De Felice and S. Tsujikawa. “f(R) Theories”. In: *Living Reviews in Relativity* 13, 3 (Dec. 2010), p. 3. DOI: 10.12942/lrr-2010-3. arXiv: 1002.4928 [gr-qc].
 - [53] T. P. Sotiriou and V. Faraoni. “f(R) theories of gravity”. In: *Reviews of Modern Physics* 82 (Jan. 2010), pp. 451–497. DOI: 10.1103/RevModPhys.82.451. arXiv: 0805.1726 [gr-qc].
 - [54] Mohamed Abdelwahab, Rituparno Goswami, and Peter K. S. Dunsby. “Cosmological dynamics of fourth-order gravity: A compact view”. In: *Phys. Rev. D* 85 (8 Apr. 2012), p. 083511. DOI: 10.1103/PhysRevD.85.083511. URL: <https://link.aps.org/doi/10.1103/PhysRevD.85.083511>.
 - [55] A. Abebe, Á. de la Cruz-Dombriz, and P. K. S. Dunsby. “Large scale structure constraints for a class of f(R) theories of gravity”. In: *Phys. Rev. D* 88.4, 044050 (Aug. 2013), p. 044050. DOI: 10.1103/PhysRevD.88.044050. arXiv: 1304.3462.
 - [56] A. M. Nzioki et al. “Geometrical approach to strong gravitational lensing in f(R) gravity”. In: *Phys. Rev. D* 83.2, 024030 (Jan. 2011), p. 024030. DOI: 10.1103/PhysRevD.83.024030. arXiv: 1002.2056 [gr-qc].
 - [57] E. Berti et al. “Testing general relativity with present and future astrophysical observations”. In: *Classical and Quantum Gravity* 32.24, 243001 (Dec. 2015), p. 243001. DOI: 10.1088/0264-9381/32/24/243001. arXiv: 1501.07274 [gr-qc].
 - [58] C. D. Leonard, T. Baker, and P. G. Ferreira. “Exploring degeneracies in modified gravity with weak lensing”. In: *Phys. Rev. D* 91.8, 083504 (Apr. 2015), p. 083504. DOI: 10.1103/PhysRevD.91.083504. arXiv: 1501.03509.
 - [59] T. Baker, P. G. Ferreira, and C. Skordis. “The parameterized post-Friedmann framework for theories of modified gravity: Concepts, formalism, and examples”. In: *Phys. Rev. D* 87.2, 024015 (Jan. 2013), p. 024015. DOI: 10.1103/PhysRevD.87.024015. arXiv: 1209.2117 [astro-ph.CO].
 - [60] Planck Collaboration et al. “Planck 2015 results. XIV. Dark energy and modified gravity”. In: *A&A* 594, A14 (Sept. 2016), A14. DOI: 10.1051/0004-6361/201525814. arXiv: 1502.01590.
 - [61] A. G. Riess et al. “A 2.4% Determination of the Local Value of the Hubble Constant”. In: *ApJ* 826, 56 (July 2016), p. 56. DOI: 10.3847/0004-637X/826/1/56. arXiv: 1604.01424.
 - [62] Planck Collaboration et al. “Planck 2013 results. XVI. Cosmological parameters”. In: *A&A* 571, A16 (Nov. 2014), A16. DOI: 10.1051/0004-6361/201321591. arXiv: 1303.5076.

- [63] M. Kilbinger et al. “CFHTLenS: combined probe cosmological model comparison using 2D weak gravitational lensing”. In: *MNRAS* 430 (Apr. 2013), pp. 2200–2220. DOI: 10.1093/mnras/stt041. arXiv: 1212.3338.
- [64] J. Harnois-Déraps et al. “KiDS-450: Tomographic Cross-Correlation of Galaxy Shear with { \backslash it Planck} Lensing”. In: *ArXiv e-prints* (Mar. 2017). arXiv: 1703.03383.
- [65] S. Joudaki et al. “KiDS-450: Testing extensions to the standard cosmological model”. In: *ArXiv e-prints* (Oct. 2016). arXiv: 1610.04606.
- [66] J. N. Dossett et al. “Constraints and tensions in testing general relativity from Planck and CFHTLenS data including intrinsic alignment systematics”. In: *Phys. Rev. D* 92.2, 023003 (July 2015), p. 023003. DOI: 10.1103/PhysRevD.92.023003. arXiv: 1501.03119.
- [67] S. Joudaki et al. “CFHTLenS revisited: assessing concordance with Planck including astrophysical systematics”. In: *MNRAS* 465 (Feb. 2017), pp. 2033–2052. DOI: 10.1093/mnras/stw2665. arXiv: 1601.05786.
- [68] A. Leauthaud et al. “Lensing is low: cosmology, galaxy formation or new physics?” In: *MNRAS* 467 (May 2017), pp. 3024–3047. DOI: 10.1093/mnras/stx258. arXiv: 1611.08606.
- [69] P. Bull et al. “Beyond Λ CDM: Problems, solutions, and the road ahead”. In: *Physics of the Dark Universe* 12 (June 2016), pp. 56–99. DOI: 10.1016/j.dark.2016.02.001. arXiv: 1512.05356.
- [70] B. Li, G.-B. Zhao, and K. Koyama. “Haloes and voids in f(R) gravity”. In: *MNRAS* 421 (Apr. 2012), pp. 3481–3487. DOI: 10.1111/j.1365-2966.2012.20573.x. arXiv: 1111.2602 [astro-ph.CO].
- [71] F. von Braun-Bates et al. “The f(Λ) halo mass function in the cosmic web”. In: *J. Cosmology Astropart. Phys.* 3, 012 (Mar. 2017), p. 012. DOI: 10.1088/1475-7516/2017/03/012. arXiv: 1702.06817.
- [72] G. Lavaux and B. D. Wandelt. “Precision cosmology with voids: definition, methods, dynamics”. In: *MNRAS* 403 (Apr. 2010), pp. 1392–1408. DOI: 10.1111/j.1365-2966.2010.16197.x. arXiv: 0906.4101.
- [73] Guilhem Lavaux and Benjamin D. Wandelt. “Precision Cosmography with Stacked Voids”. In: *The Astrophysical Journal* 754.2 (2012), p. 109. URL: <http://stacks.iop.org/0004-637X/754/i=2/a=109>.
- [74] Daeseong Park and Jounghun Lee. “Void Ellipticity Distribution as a Probe of Cosmology”. In: *Phys. Rev. Lett.* 98 (8 Feb. 2007), p. 081301. DOI: 10.1103/PhysRevLett.98.081301. URL: <https://link.aps.org/doi/10.1103/PhysRevLett.98.081301>.
- [75] D. Spolyar, M. Sahlén, and J. Silk. “Topology and Dark Energy: Testing Gravity in Voids”. In: *Physical Review Letters* 111.24, 241103 (Dec. 2013), p. 241103. DOI: 10.1103/PhysRevLett.111.241103. arXiv: 1304.5239 [astro-ph.CO].

- [76] E. V. Arbuzova, A. D. Dolgov, and L. Reverberi. “Spherically symmetric solutions in F (R) gravity and gravitational repulsion”. In: *Astroparticle Physics* 54 (Feb. 2014), pp. 44–47. DOI: 10.1016/j.astropartphys.2013.11.008. arXiv: 1306.5694 [gr-qc].
- [77] Y.-C. Cai, N. Padilla, and B. Li. “Testing Gravity using Void Profiles”. In: *ArXiv e-prints* (Oct. 2014). arXiv: 1410.8355.
- [78] P. Zivick et al. “Using cosmic voids to distinguish f(R) gravity in future galaxy surveys”. In: *MNRAS* 451 (Aug. 2015), pp. 4215–4222. DOI: 10.1093/mnras/stv1209. arXiv: 1411.5694.
- [79] A. Barreira et al. “Weak lensing by voids in modified lensing potentials”. In: *J. Cosmology Astropart. Phys.* 8, 028 (Aug. 2015), p. 028. DOI: 10.1088/1475-7516/2015/08/028. arXiv: 1505.05809.
- [80] I. Achitouv et al. “Imprint of f (R) gravity on nonlinear structure formation”. In: *Phys. Rev. D* 93.10, 103522 (May 2016), p. 103522. DOI: 10.1103/PhysRevD.93.103522. arXiv: 1511.01494.
- [81] I. Achitouv. “Testing the imprint of nonstandard cosmologies on void profiles using Monte Carlo random walks”. In: *Phys. Rev. D* 94.10, 103524 (Nov. 2016), p. 103524. DOI: 10.1103/PhysRevD.94.103524. arXiv: 1609.01284.
- [82] Steven Weinberg. *Gravitation and Cosmology: Principles and Applications of the General Theory of Relativity*. New York, NY: Wiley, 1972. URL: <https://cds.cern.ch/record/100595>.
- [83] M. Bartelmann and P. Schneider. “Weak gravitational lensing”. In: *Phys. Rep.* 340 (Jan. 2001), pp. 291–472. DOI: 10.1016/S0370-1573(00)00082-X. eprint: astro-ph/9912508.
- [84] G. Meylan et al., eds. *Gravitational Lensing: Strong, Weak and Micro*. 2006. eprint: astro-ph/0407232.
- [85] H. Hoekstra and B. Jain. “Weak Gravitational Lensing and Its Cosmological Applications”. In: *Annual Review of Nuclear and Particle Science* 58 (Nov. 2008), pp. 99–123. DOI: 10.1146/annurev.nucl.58.110707.171151. arXiv: 0805.0139.
- [86] L. van Waerbeke et al. “Magnification as a Probe of Dark Matter Halos at High Redshifts”. In: *The Astrophysical Journal Letters* 723.1 (2010), p. L13. URL: <http://stacks.iop.org/2041-8205/723/i=1/a=L13>.
- [87] David H. Weinberg et al. “Observational probes of cosmic acceleration”. In: *Physics Reports* 530.2 (2013). Observational Probes of Cosmic Acceleration, pp. 87–255. ISSN: 0370-1573. DOI: <http://dx.doi.org/10.1016/j.physrep.2013.05.001>. URL: <http://www.sciencedirect.com/science/article/pii/S0370157313001592>.
- [88] M. Kilbinger. “Cosmology with cosmic shear observations: a review”. In: *Reports on Progress in Physics* 78.8, 086901 (July 2015), p. 086901. DOI: 10.1088/0034-4885/78/8/086901. arXiv: 1411.0115.

- [89] R. D. Blandford et al. “Gravitational lens optics”. In: *Science* 245 (Aug. 1989), pp. 824–830. DOI: [10.1126/science.245.4920.824](https://doi.org/10.1126/science.245.4920.824).
- [90] M. Bartelmann. “Gravitational Lensing by Large-Scale Structures.” In: *Reviews in Modern Astronomy*. Ed. by G. Klare. Vol. 5. Reviews in Modern Astronomy. 1992, pp. 259–270.
- [91] M. Bartelmann. “Gravitational Lensing by Large-Scale Structures”. In: *Gravitational Lenses*. Ed. by R. Kayser, T. Schramm, and L. Nieser. Vol. 406. Lecture Notes in Physics, Berlin Springer Verlag. 1992, p. 345. DOI: [10.1007/3-540-55797-0_122](https://doi.org/10.1007/3-540-55797-0_122).
- [92] M. Bartelmann. “Cluster mass estimates from weak lensing.” In: *A&A* 303 (Nov. 1995), p. 643. eprint: [astro-ph/9412051](https://arxiv.org/abs/astro-ph/9412051).
- [93] M. Bartelmann and R. Narayan. “Gravitational lensing and the mass distribution of clusters”. In: *Dark Matter*. Ed. by S. S. Holt and C. L. Bennett. Vol. 336. American Institute of Physics Conference Series. July 1995, pp. 307–319. DOI: [10.1063/1.48350](https://doi.org/10.1063/1.48350). eprint: [astro-ph/9411033](https://arxiv.org/abs/astro-ph/9411033).
- [94] The Dark Energy Survey Collaboration. “The Dark Energy Survey”. In: *ArXiv Astrophysics e-prints* (Oct. 2005). eprint: [astro-ph/0510346](https://arxiv.org/abs/astro-ph/0510346).
- [95] A. Albrecht et al. “Report of the Dark Energy Task Force”. In: *ArXiv Astrophysics e-prints* (Sept. 2006). eprint: [astro-ph/0609591](https://arxiv.org/abs/astro-ph/0609591).
- [96] T. Broadhurst. “Mass distributions of clusters from gravitational magnification”. In: *Dark Matter*. Ed. by S. S. Holt and C. L. Bennett. Vol. 336. American Institute of Physics Conference Series. July 1995, pp. 320–329. DOI: [10.1063/1.48351](https://doi.org/10.1063/1.48351). eprint: [astro-ph/9505010](https://arxiv.org/abs/astro-ph/9505010).
- [97] A. H. Bauer et al. “Magnification of photometric LRGs by foreground LRGs and clusters in the Sloan Digital Sky Survey”. In: *MNRAS* 440 (June 2014), pp. 3701–3713. DOI: [10.1093/mnras/stu530](https://doi.org/10.1093/mnras/stu530). arXiv: [1312.2458](https://arxiv.org/abs/1312.2458).
- [98] J. Ford et al. “Cluster magnification and the mass-richness relation in CFHTLenS”. In: *MNRAS* 439 (Apr. 2014), pp. 3755–3764. DOI: [10.1093/mnras/stu225](https://doi.org/10.1093/mnras/stu225). arXiv: [1310.2295 \[astro-ph.CO\]](https://arxiv.org/abs/1310.2295).
- [99] I. Chiu et al. “Detection of enhancement in number densities of background galaxies due to magnification by massive galaxy clusters”. In: *MNRAS* 457 (Apr. 2016), pp. 3050–3065. DOI: [10.1093/mnras/stw190](https://doi.org/10.1093/mnras/stw190). arXiv: [1510.01745](https://arxiv.org/abs/1510.01745).
- [100] H. Hildebrandt, L. van Waerbeke, and T. Erben. “CARS: The CFHTLS-Archive-Research Survey. III. First detection of cosmic magnification in samples of normal high-z galaxies”. In: *A&A* 507 (Nov. 2009), pp. 683–691. DOI: [10.1051/0004-6361/200912655](https://doi.org/10.1051/0004-6361/200912655). arXiv: [0906.1580](https://arxiv.org/abs/0906.1580).
- [101] C. B. Morrison et al. “Tomographic magnification of Lyman-break galaxies in the Deep Lens Survey”. In: *MNRAS* 426 (Nov. 2012), pp. 2489–2499. DOI: [10.1111/j.1365-2966.2012.21826.x](https://doi.org/10.1111/j.1365-2966.2012.21826.x). arXiv: [1204.2830](https://arxiv.org/abs/1204.2830).
- [102] M. Seldner and P. J. E. Peebles. “Statistical analysis of catalogs of extragalactic objects. XI - Evidence of correlation of QSOs and Lick galaxy counts”. In: *ApJ* 227 (Jan. 1979), pp. 30–36. DOI: [10.1086/156699](https://doi.org/10.1086/156699).

- [103] C. J. Hogan, R. Narayan, and S. D. M. White. “Quasar lensing by galaxies?” In: *Nature* 339 (May 1989), p. 106. doi: 10.1038/339106b0.
- [104] W. Fugmann. “Statistical gravitational lensing and the Lick catalogue of galaxies”. In: *A&A* 240 (Dec. 1990), pp. 11–21.
- [105] M. Bartelmann and P. Schneider. “Large-scale correlations between QSOs and galaxies - an effect caused by gravitational lensing?” In: *A&A* 268 (Feb. 1993), pp. 1–13.
- [106] B. Ménard and M. Bartelmann. “Cosmological information from quasar-galaxy correlations induced by weak lensing”. In: *A&A* 386 (May 2002), pp. 784–795. doi: 10.1051/0004-6361:20020274. eprint: astro-ph/0203163.
- [107] Ryan Scranton et al. “Detection of Cosmic Magnification with the Sloan Digital Sky Survey”. In: *The Astrophysical Journal* 633.2 (2005), p. 589. URL: <http://stacks.iop.org/0004-637X/633/i=2/a=589>.
- [108] L. Wang et al. “HerMES: detection of cosmic magnification of submillimetre galaxies using angular cross-correlation”. In: *MNRAS* 414 (June 2011), pp. 596–601. doi: 10.1111/j.1365-2966.2011.18417.x. arXiv: 1101.4796.
- [109] B. Ménard et al. “Measuring the galaxy-mass and galaxy-dust correlations through magnification and reddening”. In: *MNRAS* 405 (June 2010), pp. 1025–1039. doi: 10.1111/j.1365-2966.2010.16486.x. arXiv: 0902.4240.
- [110] B. Jain and M. Lima. “Magnification effects on source counts and fluxes”. In: *MNRAS* 411 (Mar. 2011), pp. 2113–2117. doi: 10.1111/j.1365-2966.2010.17505.x. arXiv: 1003.6127.
- [111] Eric M. Huff and Genevieve J. Graves. “Magnificent Magnification: Exploiting the Other Half of the Lensing Signal”. In: *The Astrophysical Journal Letters* 780.2 (2014), p. L16. URL: <http://stacks.iop.org/2041-8205/780/i=2/a=L16>.
- [112] M. Crocce et al. “Galaxy clustering, photometric redshifts and diagnosis of systematics in the DES Science Verification data”. In: *MNRAS* 455 (Feb. 2016), pp. 4301–4324. doi: 10.1093/mnras/stv2590. arXiv: 1507.05360.
- [113] C. Chang et al. “Modeling the Transfer Function for the Dark Energy Survey”. In: *The Astrophysical Journal* 801.2 (2015), p. 73. URL: <http://stacks.iop.org/0004-637X/801/i=2/a=73>.
- [114] E. Bertin and S. Arnouts. “SExtractor: Software for source extraction.” In: *A&AS* 117 (June 1996), pp. 393–404. doi: 10.1051/aas:1996164.
- [115] I. Sevilla et al. “The Dark Energy Survey Data Management System”. In: *ArXiv e-prints* (Sept. 2011). arXiv: 1109.6741 [astro-ph.IM].
- [116] S. Desai et al. “The Blanco Cosmology Survey: Data Acquisition, Processing, Calibration, Quality Diagnostics, and Data Release”. In: *ApJ* 757, 83 (Sept. 2012), p. 83. doi: 10.1088/0004-637X/757/1/83. arXiv: 1204.1210 [astro-ph.CO].

- [117] J. J. Mohr et al. “The Dark Energy Survey data processing and calibration system”. In: *Software and Cyberinfrastructure for Astronomy II*. Vol. 8451. Proc. SPIE. Sept. 2012, p. 84510D. DOI: 10.1117/12.926785. arXiv: 1207.3189 [astro-ph.IM].
- [118] M. E. C. Swanson et al. “Methods for rapidly processing angular masks of next-generation galaxy surveys”. In: *MNRAS* 387 (July 2008), pp. 1391–1402. DOI: 10.1111/j.1365-2966.2008.13296.x. arXiv: 0711.4352.
- [119] K. M. Górski et al. “HEALPix: A Framework for High-Resolution Discretization and Fast Analysis of Data Distributed on the Sphere”. In: *ApJ* 622 (Apr. 2005), pp. 759–771. DOI: 10.1086/427976. eprint: astro-ph/0409513.
- [120] M. Carrasco Kind and R. J. Brunner. “TPZ: photometric redshift PDFs and ancillary information by using prediction trees and random forests”. In: *MNRAS* 432 (June 2013), pp. 1483–1501. DOI: 10.1093/mnras/stt574. arXiv: 1303.7269.
- [121] C. Sánchez et al. “Photometric redshift analysis in the Dark Energy Survey Science Verification data”. In: *MNRAS* 445 (Dec. 2014), pp. 1482–1506. DOI: 10.1093/mnras/stu1836. arXiv: 1406.4407 [astro-ph.IM].
- [122] M. Jarvis, G. Bernstein, and B. Jain. “The skewness of the aperture mass statistic”. In: *MNRAS* 352 (July 2004), pp. 338–352. DOI: 10.1111/j.1365-2966.2004.07926.x. eprint: astro-ph/0307393.
- [123] S. D. Landy and A. S. Szalay. “Bias and variance of angular correlation functions”. In: *ApJ* 412 (July 1993), pp. 64–71. DOI: 10.1086/172900.
- [124] E. Suchyta et al. “No galaxy left behind: accurate measurements with the faintest objects in the Dark Energy Survey”. In: *MNRAS* 457 (Mar. 2016), pp. 786–808. DOI: 10.1093/mnras/stv2953. arXiv: 1507.08336.
- [125] James MacQueen et al. “Some methods for classification and analysis of multivariate observations”. In: *Proceedings of the fifth Berkeley symposium on mathematical statistics and probability*. Vol. 1. 14. Oakland, CA, USA. 1967, pp. 281–297.
- [126] F. Pedregosa et al. “Scikit-learn: Machine Learning in Python”. In: *Journal of Machine Learning Research* 12 (2011), pp. 2825–2830.
- [127] T. Giannantonio et al. “CMB lensing tomography with the DES Science Verification galaxies”. In: *MNRAS* 456 (Mar. 2016), pp. 3213–3244. DOI: 10.1093/mnras/stv2678. arXiv: 1507.05551.
- [128] P. Schechter. “An analytic expression for the luminosity function for galaxies.” In: *ApJ* 203 (Jan. 1976), pp. 297–306. DOI: 10.1086/154079.
- [129] B. Ménard et al. “Improving the accuracy of cosmic magnification statistics”. In: *A&A* 403 (June 2003), pp. 817–828. DOI: 10.1051/0004-6361:20030406. eprint: astro-ph/0210112.
- [130] H. Hildebrandt. “Observational biases in flux magnification measurements”. In: *MNRAS* 455 (Feb. 2016), pp. 3943–3951. DOI: 10.1093/mnras/stv2575. arXiv: 1511.01352.

- [131] A. J. Ross et al. “The clustering of galaxies in the SDSS-III Baryon Oscillation Spectroscopic Survey: analysis of potential systematics”. In: *MNRAS* 424 (July 2012), pp. 564–590. DOI: 10.1111/j.1365-2966.2012.21235.x. arXiv: 1203.6499.
- [132] B. Leistedt et al. “Mapping and simulating systematics due to spatially-varying observing conditions in DES Science Verification data”. In: *ArXiv e-prints* (July 2015). arXiv: 1507.05647.
- [133] C. B. Morrison and H. Hildebrandt. “Mitigating systematic errors in angular correlation function measurements from wide field surveys”. In: *MNRAS* 454 (Dec. 2015), pp. 3121–3133. DOI: 10.1093/mnras/stv2103. arXiv: 1509.04290.
- [134] S. Ho et al. “Clustering of Sloan Digital Sky Survey III Photometric Luminous Galaxies: The Measurement, Systematics, and Cosmological Implications”. In: *ApJ* 761, 14 (Dec. 2012), p. 14. DOI: 10.1088/0004-637X/761/1/14. arXiv: 1201.2137.
- [135] C. Bennett et al. “Redshift distributions of galaxies in the Dark Energy Survey Science Verification shear catalogue and implications for weak lensing”. In: *Phys. Rev. D* 94 (4 Aug. 2016), p. 042005. DOI: 10.1103/PhysRevD.94.042005. URL: <http://link.aps.org/doi/10.1103/PhysRevD.94.042005>.
- [136] G. Bernstein and D. Huterer. “Catastrophic photometric redshift errors: weak-lensing survey requirements”. In: *MNRAS* 401 (Jan. 2010), pp. 1399–1408. DOI: 10.1111/j.1365-2966.2009.15748.x. arXiv: 0902.2782 [astro-ph.CO].
- [137] J. A. Newman. “Calibrating Redshift Distributions beyond Spectroscopic Limits with Cross-Correlations”. In: *ApJ* 684, 88-101 (Sept. 2008), pp. 88–101. DOI: 10.1086/589982. arXiv: 0805.1409.
- [138] D. J. Matthews and J. A. Newman. “Reconstructing Redshift Distributions with Cross-correlations: Tests and an Optimized Recipe”. In: *ApJ* 721 (Sept. 2010), pp. 456–468. DOI: 10.1088/0004-637X/721/1/456. arXiv: 1003.0687 [astro-ph.CO].
- [139] B. Ménard et al. “Clustering-based redshift estimation: method and application to data”. In: *ArXiv e-prints* (Mar. 2013). arXiv: 1303.4722.
- [140] V. Scottez et al. “Clustering-based redshift estimation: application to VIPERS/CFHTLS”. In: *MNRAS* 462 (Oct. 2016), pp. 1683–1696. DOI: 10.1093/mnras/stw1500. arXiv: 1605.05501.
- [141] P. Graff et al. “SKYNET: an efficient and robust neural network training tool for machine learning in astronomy”. In: *MNRAS* 441 (June 2014), pp. 1741–1759. DOI: 10.1093/mnras/stu642. arXiv: 1309.0790 [astro-ph.IM].
- [142] N. Benítez. “Bayesian Photometric Redshift Estimation”. In: *ApJ* 536 (June 2000), pp. 571–583. DOI: 10.1086/308947. eprint: astro-ph/9811189.